Institut für Physikalische und Theoretische Chemie
der Technischen Universität München

Mechanisms of Charge Separation and Protein Relaxation Processes in Native and Modified Reaction Centers of Photosynthetic Bacteria *Rb. sphaeroides* R26 Studied by Picosecond Time Resolved Fluorescence.

Pancho Tzankov

Vollständiger Abdruck der von der Fakultät für Chemie der Technischen Universität München zur Erlangung des akademischen Grades eines

Doktors der Naturwissenschaften

genehmigten Dissertation.

Vorsitzender:	Univ.-Prof. Dr. H. J. Neusser
Prüfer der Dissertation:	
	1. Priv.-Doz. Dr. A. Ogrodnik
	2. Univ.-Prof. Dr. H. Scheer, Ludwig-Maximilians-Universität München

Die Dissertation wurde am 01.07.2003 bei der Technischen Universität München eingereicht und durch die Fakultät für Chemie am 11.09.2003 angenommen.

In memory of Nickolay Panchev Tzankov, my Father.

Table of Contents

1. Introduction

The photosynthetic reaction centre (RC) is a membrane bound pigment protein complex which accepts the energy from the light-harvesting antenna and performs the electron transfer reaction, thereby converting the electronic excitation energy into chemical energy. The RC from *Rb. sphaeroides* is one of the best characterized complexes. The three dimensional structure of this RC was determined by X-ray diffraction studies with 2.65 Å resolution (average coordinate error 0.3 Å)[1]. The main components of the RC are a closely interacting dimer P (the special-pair) of bacteriochlorophyll (BChl) molecules (D_A, D_B), two BChl monomers (B_A, B_B), two bacteriopheophytins (BPhes H_A, H_B) and two quinones (Q_A, Q_B), all arranged into two branches, labeled A and B.

Between the quinones is an iron atom which is believed to stabilize the complex. All these elements are bound together by transmembrane helices that also introduce some asymmetry into the structure. Fig. 1.1 shows the protein imbedded in the bacterial membrane (a) and the principal arrangement of the main elements without the protein frame (b-c). Experimentally it has been established that electron transfer proceeds from the special-pair via the A-branch. The special-pair dimer P acts as the primary electron donor, which after having received excitation energy from antenna, donates an electron to H_A in ~3.5 ps. Since the distance between the special-pair and the H_A is ~17 Å[1], one is tempted to assume that the electron transfer proceeds via the B_A monomer which is located between the special-pair and the H_A in order to explain the fast transfer rate. From H_A the electron is transferred to the primary quinone Q_A in ~200 ps and subsequently to the secondary quinone Q_B in ~200 µs (see Fig. 1.2).

The distance between the BChl molecules D_A and D_B of the special-pair dimer P is less than 4 Å[1], which implies that the adequate description should consider the dimer as a supermolecule. Thus its absorption is the most red shifted among all of the other pigments in the protein. The absorption spectrum of the reaction center is given in Fig. 1.3. It is easy to distinguish between the Q_x and the Q_y absorption bands of the pigments. The most blue shifted absorption is from the quinones. Than the Q_x band of H_A and H_B follow at 535 and 545 nm, respectively. All of the rest of the absorption bands are coinciding for the pigment in A-branch and in B-branch of the RC. The Q_x band of BChls (B_A and B_B) is around 600 nm while their Q_y band is at 800 nm where the Q_x band of the special-pair P is overlapping too. The Q_y bands of BPhes H_A and H_B are around 760 nm and the Q_y band of P is around 865 nm where we have presumably excited in the experiments reported in this thesis. If BChls are exchanged vs. Vinyl-BChls Vinyl-$B_{A,B}$ their Q_y absorption shifts to 777 nm while their Q_x band shifts to 577 nm.

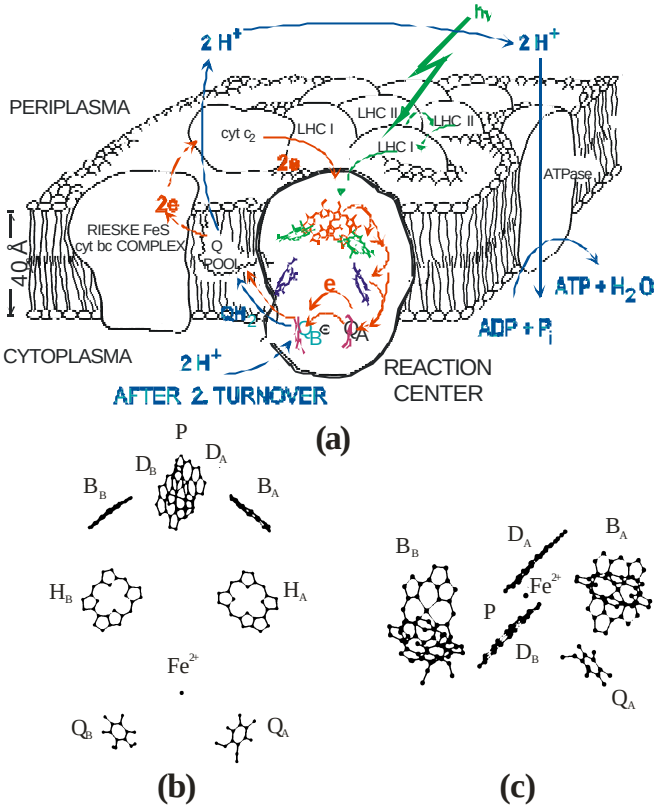

Fig. 1.1. The photosynthetic reaction center protein in the native bacterial membrane (a), side (b) and top (c) views. LHC – Light Harvesting Complex (Antenna), cyt – cytochrome.

Independently of which pigment is excited ultrafast energy transfer is done within 200 fs to the Q_y band of the special pair P.

The photosynthesis process is illustrated in Fig. 1.1. Upon excitation of P either by light or by energy transfer from LHC an electron transfer occurs through the membrane creating a photocontrolled gradient of protons from the both sides of the membrane. This gradient is used for the ATPase – process of creation of ATP which is the main energy carrier in the life organism.

This electron transfer is in the base of the photosynthetic processes in the bacteria. It is very extensively investigated in the past 30 years and could serve us for tracking the relaxation of the protein matrix where the pigments are situated. This protein relaxation is believed to be universal in Nature for many other proteins and will be investigated using the method of delayed fluorescence developed in Chapter 4. The electron process itself will be investigated in Vinyl-$B_{A,B}$ RCs in Chapter 5 analyzing its temperature dependence and in Chapter 6 using

time-resolved electric field induced fluorescence anisotropy method for the first time.

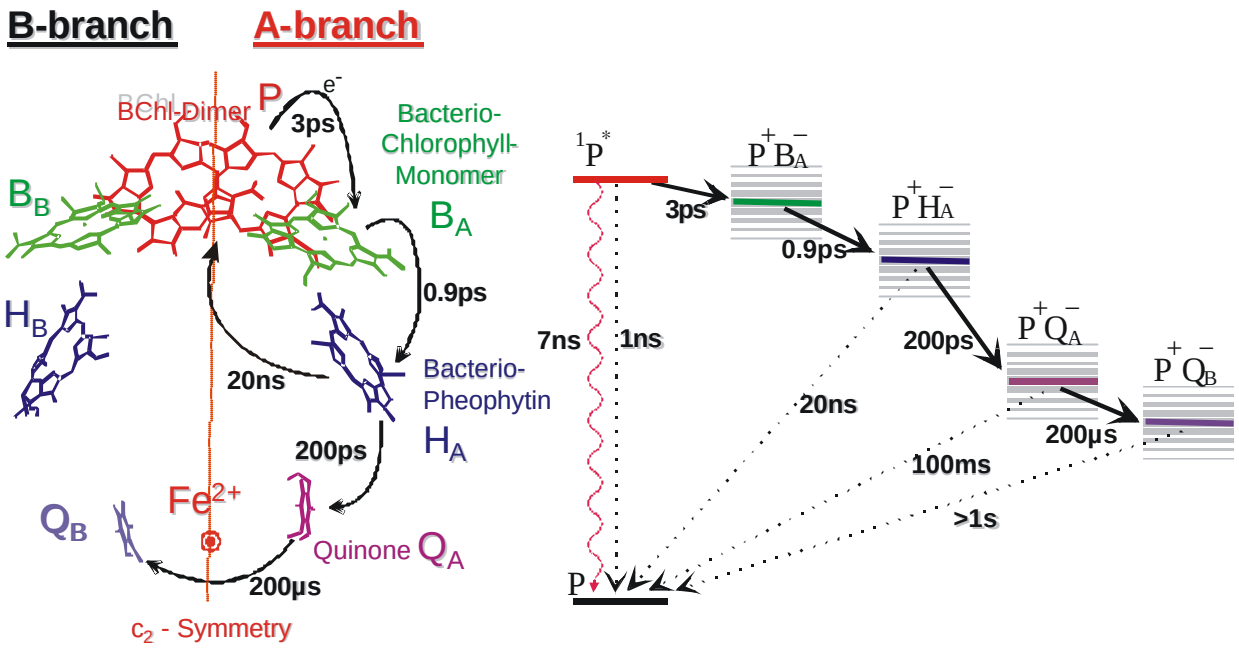

Fig. 1.2. Electron transfer kinetics of R26 RCs of *Rb. sphaeroides*

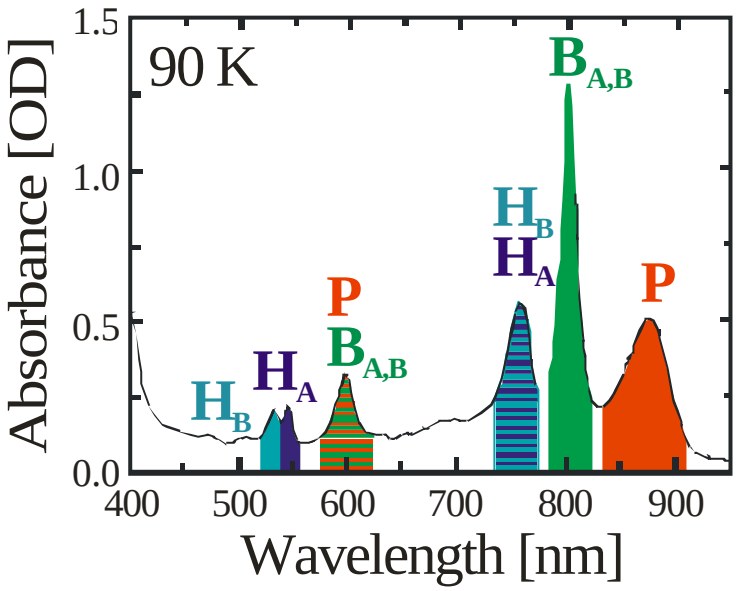

Fig. 1.3. Absorption spectrum of R26 RCs of *Rb. sphaeroides* at temperature of 90 K

As the electron moves through the different pigment in the multistep electron transfer through the membrane it creates enormous dipole moments. It is believed that the formed radical pairs have considerable heterogeneous broadening of their energy distributions due to the accompanying electrochromic shifts (see Fig. 1.2). We will identify the width of the $P^+H_A^-$ radical pair free energy distribution at 85 K using the combined results from the three different methods which will be considered in Chapters 4, 5 and 6.

2. Experimental methods

2.1. Picosecond time-resolved fluorescence measurements

Fluorescence kinetics were measured with the apparatus depicted in Fig. 2.1. and a similar one described in [2, 3]. Based on [4] and [5] the setup was extended to include a second excitation light source, a Ti:Sapphire regenerative amplifier (Coherent RegA 9000) seeded by Ti:Sapphire oscillator (Coherent Mira 900B) and both pumped by an Ar^+ laser (Coherent Innova 425). The RegA delivered more than 1 μJ pulses with 200 fs pulsewidth around 800 nm and 100 kHz repetition rate. The output of the RegA was focused into a 3 mm thick sapphire plate and a single filament white-light continuum was produced. It was collimated with a doublet achromatic lens introducing very small chromatic aberrations. A holographic notch filter with more than 4 OD rejection in the whole spectrum of the RegA output around 800 nm was placed behind the white-light generator. With this means of providing excitation pulses in broader spectral range (450 - 1600 nm) it became feasible to excite also the other absorption bands in the photosynthetic reaction center except the BChl Q_y band around 800 nm. The wavelength of the excitation pulses was chosen by interference bandpass filters with suppression of the remaining part of the white-light continuum with a minimal factor of 10^3.

For excitation in the Q_y absorption band of the special pair a laser diode at 864 nm Hamamatsu PLP-01: pulsewidth 40 ps, energy 2 pJ, repetition rate 10 MHz is used. Its output is further filtered by a bandpass filter with transmission of more than 70% for the same wavelength in order to reject the intrinsic for the laser diode stray light at parasitic wavelengths.

2.2. Time-correlated single photon counting

In principle time-correlated single photon counting (TCSPC) is measuring the time between the excitation of the sample and the consecutive emission of a single photon. The fluorescence signal is attenuated so that physically only one photon per around 100 excitation pulses is detected. Accumulation of a manifold of such measurements yields a histogram depicting the time dependence of the fluorescence of the sample.

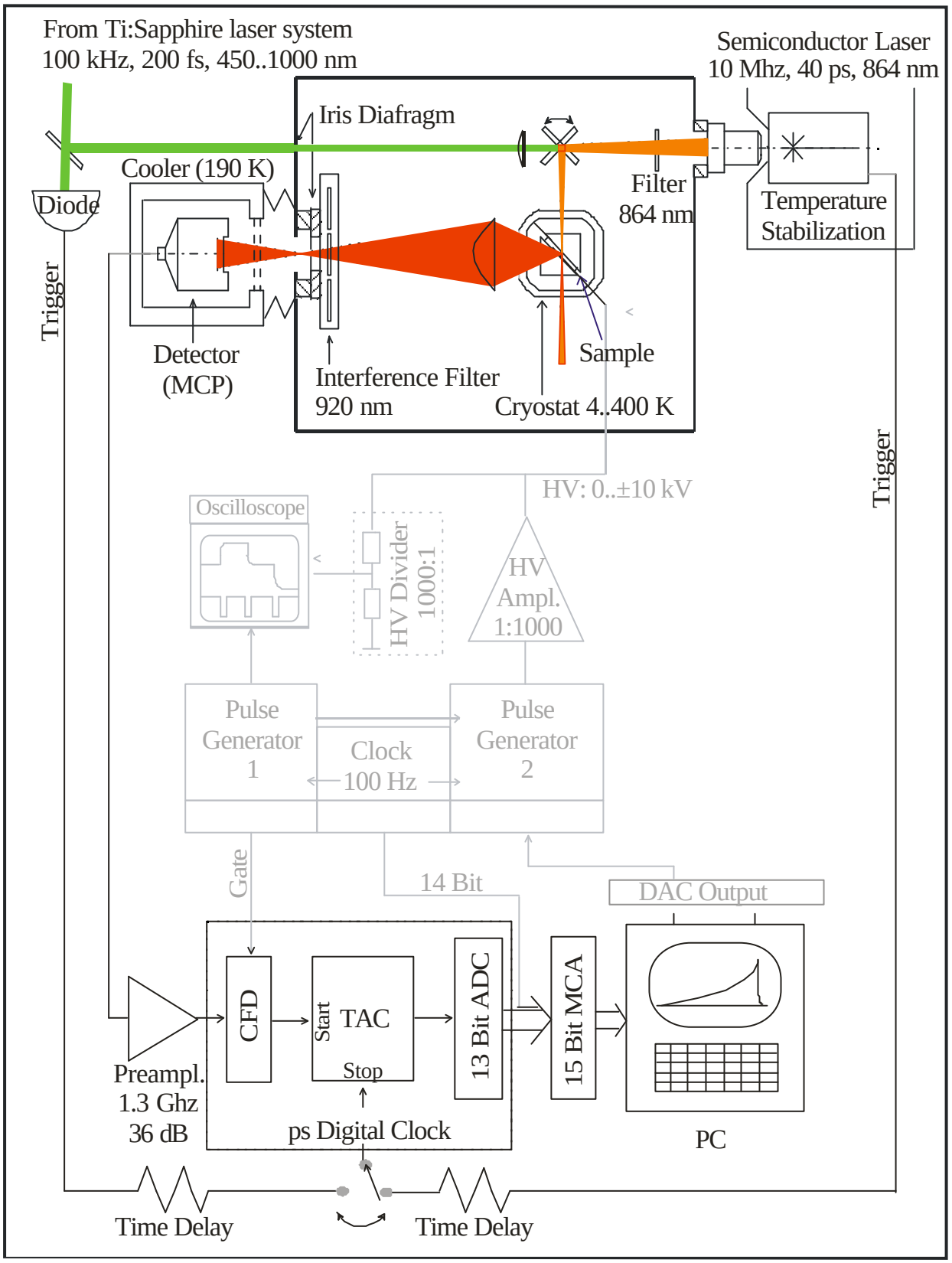

Fig. 2.1. Schematic setup of the picosecond time-resolved fluorescence apparatus. MCP – micro channel plate, CFD – constant fraction discriminator, TAC – time to amplitude converter, ADC – analog to digital converter, DAC – digital to analog converter, MCA – multi-channel analyzer, HV – high voltage.

The wavelength of the photons to be detected is selected by two bandpass filters Schott DAD 8-2 with peak transmission at 920 nm of more than 70% and a rejection for 865 nm stray light of 10^4. The signal of the detector, a high speed microchannel plate photomultiplier tube (Hamamatsu R2809-U with selected S1 cathode) cooled to 190 K to reduce noise, is fed to an ultrafast pre-amplifier (Hewlett-Packard) and then converted to a NIM pulse utilizing a constant fraction discriminator timing discriminator (Tennelec TC454) (see Fig.2.1). The resultant almost jitter-free signal starts a time-to-amplitude converter (Ortec 567). In parallel, a small fraction of the RegA output at 800 nm or a TTL pulse from the laser diode power supply are used to generate a constant sequence of stop pulses. This inverted mode (the subsequent excitation pulse serves as timing reference) drastically reduces the TAC's deadtime while it is possible to maintain the high repetition rates of the laser systems. The TAC's amplitude output is digitized with ADC 7070 (FAST ComTec) and is stored in a 13 bit buffer MCD/PC (CMTE). Finally a multichannel analyzer software (FAST ComTec MCDDOS 32) running on a PC displays the results.

In TCSPC the instrument response function (IRF) of the setup described above has a full width at half maximum between 38 and 42 ps using the white-light as an excitation source and between 55 and 63 using the laser diode. The time window is limited by the corresponding repetition rate (10 μs for the case of RegA and 100 ns for the case of laser diode as excitation sources). On a daily basis two distinct time windows were used: 33 ns (short time window) and 66 ns (long time window).

2.3. The numerical analysis of the measurements

The goal of the numerical analysis is to describe the fluorescence kinetics measured in TCSPC. By an analytical function which is independent of statistical and systematical perturbations. In the cases relevant here the profiles derived from the measurements are in principle a convolution of the intrinsic fluorescence kinetics of the sample and the IRF. They are further including statistical noise, remains of the background signal and long-lived components of the fluorescence excited by the previous laser pulse.

The IRF itself is a convolution of the actual excitation light pulse and the response of the apparatus to a δ-shaped excitation. In practice it is measured by replacing the sample with a "scatter solution" (e.g. diluted milk or LIDOX (Si nanoparticles) solution or even rice paper) simulating a fluorophore with a lifetime of 0 ps.

In this work the deconvolution of the measured profiles was carried out with the program GNUAP[6] based on the Marquardt algorithm of nonlinear least squares fits[7]. The criterion to be minimized is given by:

$$\chi^{(2)} = \sum_{i=1}^{N} \left(\frac{Y_i - F(t_i)}{\sigma_i} \right)$$

where N is the number of data points in the profile, Y_i and σ_i the i^{th} data point and its statistical error, respectively, and F(t) the test function[7].

F(t) can be written as the sum of two terms: (i) a constant background signal B, (ii) the convolution of the IRF I(t) and the model function f(t) used to describe the fluorescence kinetics of the sample:

$$F(t) = B + \int_{-\infty}^{+\infty} I(t') f(t - t') dt'$$

In general f(t) has to be derived from the applied physical model – in case of fluorescence species it is commonly written as a sum of exponential terms:

$$f(t) = \sum_i A_i \, exp\left(-\frac{t}{\tau_i} \right)$$

However, one should keep in mind that other sets of functions could exist that might fit the profiles equally well.

Two criteria are employed to evaluate the quality of the fit results: (i) the reduced $\chi_r^{(2)} = \chi^{(2)} / (N - n_p)$. Normalized by the difference between the number of data points N and the number of free parameters n_p, $\chi_r^{(2)}$ should be close to unity, i.e. the mean square deviation of the data points from the test function is close to the statistical error. (ii) The weighted residuals $R_i = [Y_i - F(t_i)]/\sigma_i$ should be distributed statistically around zero with amplitude of less than 4.

Finally the lifetimes have an uncertainty of less than 20 % unless they are within the IRF time width. Lifetimes not shorter than half of the IRF width could be resolved with ambiguity of 2.

3. Theoretical background of the photoinduced electron transfer

Upon photoexcitation the molecules experience various photochemical reaction pathways which are classified in Table 3.1.[8].

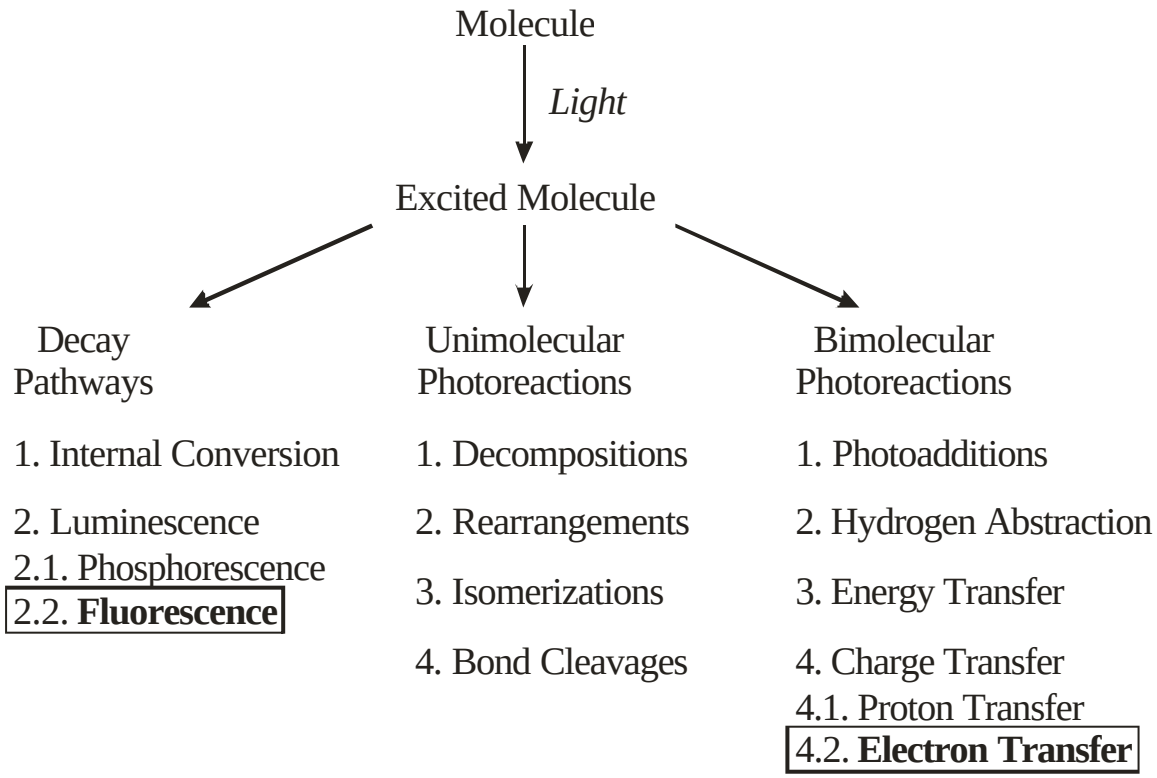

Table 3.1. Photoinduced reaction pathways in chemistry.

In this chapter, the theoretical basics and principles of the photoinduced electron transfer (ET) and fluorescence will be introduced. Some fluorescence methods for monitoring of ET and its influence on the surrounding required for an understanding of the experiments reported in the next chapters will be presented.

3.1 Introduction

Photoinduced electron transfer (ET) plays a central role in a broad array of processes in the physical, chemical and biological sciences[9-11] [8, 12, 13]. The seminal theoretical contributions of Marcus[14, 15] and the Russian school[16, 17] nearly half a century ago and the later contribution of Hush[18] and Jortner[19] established the modern view of the ET theory. Current theoretical

techniques permit detailed treatment of various complex ET systems at quantum mechanical or classical levels as dictated by the environmental conditions.

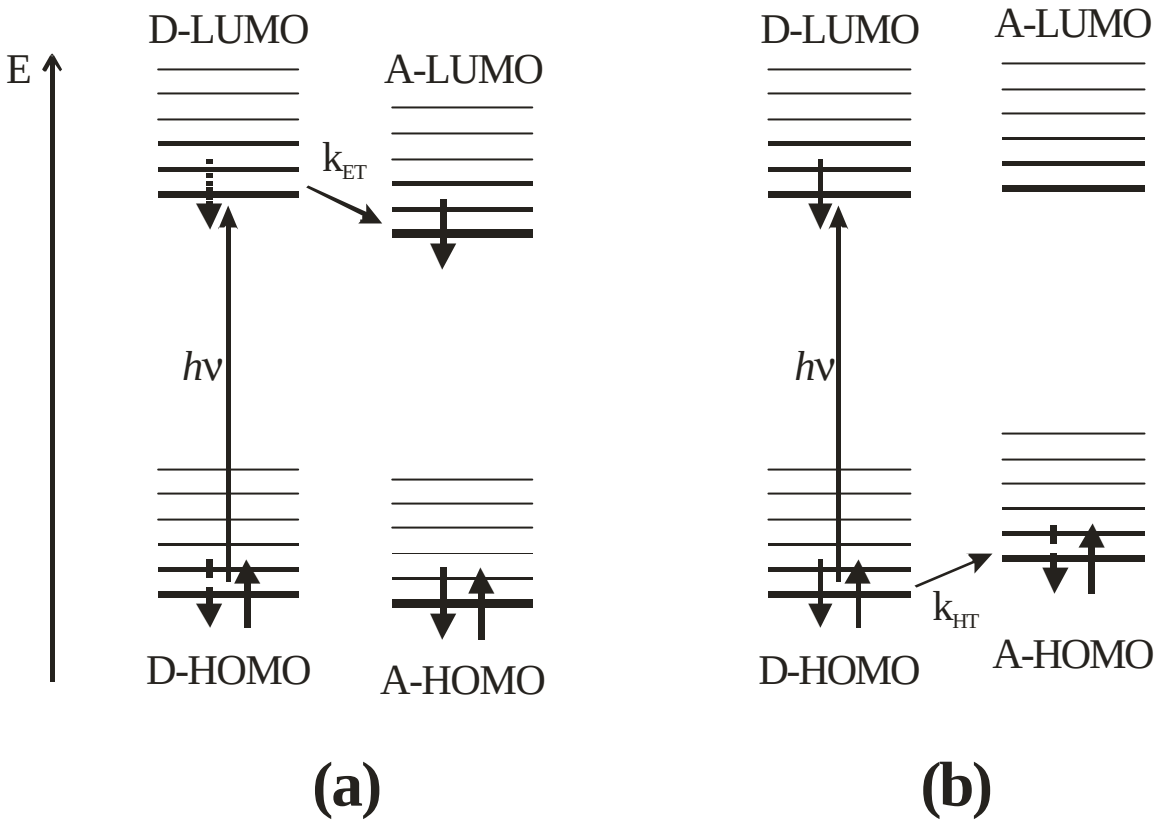

Fig. 3.1 Photoinduced charge transfer in a donor-acceptor complex. (a) Photoinduced electron transfer (ET), (b) photoinduced hole transfer (HT). There are shown the electron configurations of the reactant, photoexcited reactant and product states with dashed, dotted and solid lines, respectively. Thick lines and thin lines represent electronic and vibrational levels, respectively. The different lines in groups represent the vibronic structure of the electronic states. The thick lines in every group are the lowest vibrational states.

In its most simple description, electron transfer is the result of the transition of a single electron from a photoinduced reactant molecular state, i.e. the donor (D) state, to a product molecular acceptor (A) state[8, 9, 20]. In a photoinduced electron transfer reaction the photoexcited molecule can act either as oxidizing or reducing species. Concentrating only on the highest occupied molecular orbital (HOMO) and the lowest unoccupied molecular orbital (LUMO) of the donor-acceptor electronic manifold, Fig. 3.1. illustrates the possible pathways of ET. By optical excitation an electron of the donor is placed into the LUMO which is becoming the donor HOMO. The ET proceeds between the donor LUMOs and the acceptor LUMOs. Alternatively, an electron may move in the opposite direction from the acceptor HOMOs to the donor HOMOs. This process is usually called a hole transfer since the reaction can be alternatively understood as the motion of a missing electron (hole) from the donor to the acceptor.

From now on we will investigate only intramolecular ET, i.e. when the relative position between the donor and acceptor molecules is chemically fixed either in a large molecule as in photosynthetic reaction centers or DNA or by a molecular bridge in solvents.

3.2. Electron transfer rates

For a quantitative treatment of the rates of the ET let us consider the ET as a radiationless transition in the donor-acceptor system from an ensemble of photoexcited non-charge separated donor-acceptor molecular states D^*A associated with a wavefunction manifold $\{|rv>\}_v$ to an ensemble of charge separated product molecular states D^+A^- with a wavefunction manifold $\{|pw>\}_w$. Since the electrons are much faster than the nucleus because their mass is much smaller, we can consider them as moving approximately in a frozen potential formed by the motionless nuclei. In terms of such approximation, called the Born-Oppenheimer approximation, we could split the system Hamiltonian to an electronic and a nuclear part and consequently the wavefunctions of the quantum mechanical donor-acceptor system could be presented as:

$$\begin{aligned} |rv\rangle &= \varphi_r(x,Q)\chi_{rv}(Q) \\ |pw\rangle &= \varphi_p(x,Q)\chi_{pw}(Q) \end{aligned}, \tag{3.1}$$

where x and Q are the coordinates of the electrons and the nucleus, respectively. The φ_r and φ_p are the electronic wavefunctions, the χ_{rv} and χ_{pw} are the nuclear wavefunctions in the reactant (r) and in the product (p) states and v and w are describing the vibrational quantum numbers, respectively.

Lets us consider, for simplicity, that an electron to be transferred interacts with nucleus through a single nuclear reaction coordinate Q which passes through the relaxed nuclear configurations at the reactant state ($Q = 0$) and at the product state ($Q = \Delta$). Then the transfer integral between the initial and final states of the donor-acceptor system is defined as

$$V(Q)_{rv,pw} = \langle rv|\hat{V}|pw\rangle = \langle\varphi_r|\hat{V}|\varphi_p\rangle\langle\chi_{rv}|\chi_{pw}\rangle. \tag{3.2}$$

According to the Condon approximation the transfer integral for each two vibronic states of the reactant and the product is linearly proportional to the overlap between their wavefunctions with a constant V called coupling:

$$V(Q)_{rv,pw} = V\langle\varphi_r|\varphi_p\rangle\langle\chi_{rv}|\chi_{pw}\rangle \tag{3.3}$$

An idea for the functions $V(Q)_{rv,pw}$ one could obtain from Fig. 3.3. The function $V(Q)_{rv,pw}$ is significantly different than 0 only in the region around Q_c.

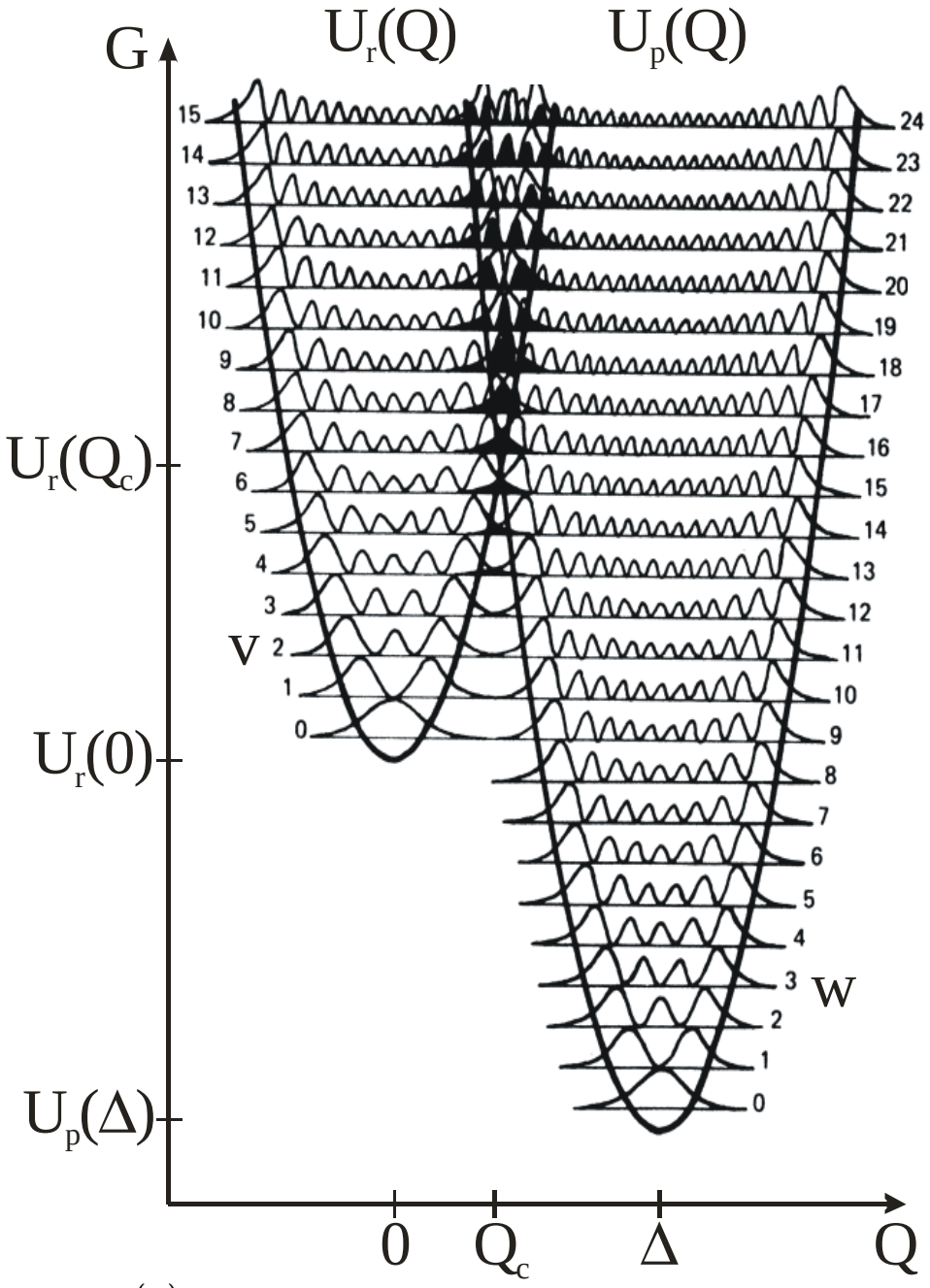

Fig. 3.2 Couplings $V(Q)_{rv,pw}$ for vibronic manifold of reactant and product states. The potentials are assumed harmonic, with the same curvature and cross at Q_c[21].

According to the Transition State Theory a transition between two different electronic states is possible only between approximately isoenergetical vibronic states. The product vibronic state experiences a concomitant relaxation to the lowest vibrational state. Such transition states are observed for the first time by Zewail[22]. On Fig. 3.2 are presented the $V(Q)_{rv,pw}$ functions only for isoenergetical states.

Depending on the magnitude of the coupling *V*, electron transfer theories can be divided into nonadiabatic or diabatic (small *V*) where ET rate is dependent on the square of the coupling and adiabatic (large *V*) where the ET rate is weakly dependent on coupling.

3.3 Nonadiabatic electron transfer

In the case of week coupling the ET probability is coupling determined and the electron could be found localized in the reactant or in the product state and thus could be treated by the perturbation theory of first order. This regime of ET is called nonadiabatic. Using the Fermi's golden rule for the ET rate from a single initial state $|iv>$to a manifold of final states $\{|fw>\}_w$ we have:

$$k_{rv\to\{pw\}} = \frac{2\pi}{\hbar}\sum_w \left|V_{rv,pw}\right|^2 \delta\left(E_{pw} - E_{rv}\right) \tag{3.4}$$

With the delta function is denoted that only an isoenergetical transitions are allowed according. If we consider an equilibrium population of the initial reactant state given from the Boltzmann distribution:

$$\rho_v = \frac{exp\left(-E_{av}/k_B T\right)}{\sum_v exp\left(-E_{av}/k_B T\right)} \tag{3.5}$$

for the average ET rate, i.e macroscopically observable ET rate from the reactant to the product state we have:

$$k = \sum_v \rho_v k_{rv\to\{pw\}} \tag{3.6}$$

and thus from eq. 3.4 and 3.5 we obtain the usual form for the nonadiabatic ET:

$$k = \frac{2\pi}{\hbar}\left|V\right|^2 FC \tag{3.7}$$

with thermally weighted Franc-Condon factor:

$$FC = \sum_v \sum_w \rho_v \left|\left\langle \chi_{iv} \middle| \chi_{fw} \right\rangle\right|^2 \delta\left(E_{fw} - E_{iv}\right) \tag{3.8}$$

The macroscopic ET in the nonadiabatic regime could be interpreted as a product between the square of the coupling and the Frank-Condon factor, which is a measure of the thermally weighted overlap between the nuclear wavefunctions (Fig. 3.3).

3.4. Adiabatic vs. nonadiabatic electron transfer

The distinction between nonadiabatic and adiabatic electron transfer is related to the magnitude of the electronic interaction between the reactant and the product potential energy surface (Fig. 3.4). In the nonadiabatic limit the splitting at the barrier top, given by the crossing point of the curves, is very small and is not considered. If we have a strong coupling between the donor and the acceptor states the ET proceeds on a single potential surface (Fig. 3.4(c)) while if the coupling is week the ET is a radiationless isoenergetic transition between the two adiabatic potentials of the reactant and product states (Fig. 3.4(b)). A quantitative criterion of the adiabaticity of the ET is given by the Landau-Zener parameter:

$$\gamma_{LZ} = V^2 \frac{2\pi}{\hbar\omega\sqrt{2\lambda k_B T}} \tag{3.9}$$

where $\hbar\omega$ is the characteristic vibrational energy of the medium, λ is the reorganization energy of the medium (see below) and $k_B T$ is the thermal energy.

In the case of $\gamma_{LZ} \leq 1$ the nonadiabatic approximation for the ET is applicable.

For $\gamma_{LZ} > 1$ when V is larger than the characteristic vibrational energy of the medium, the first order perturbation theory of the nonadiabatic ET could be not applied anymore. The rate determining process is the friction in the motion through the diabatic potential surface rather than the coupling.

3.5. Frank-Condon factor in single-mode approximation

The ET can be coupled to different vibrations of the nuclear configuration of the donor-acceptor molecular system. In the single mode approximation we can consider all the vibronic manifold of states as a single one with an average energy $\hbar\omega$ identical in the reactant and in the product state for the ET. Thus we restrict the donor-acceptor system to a single quantum-mechanical degree of freedom on the initially multidimensional potential surface. In this case the adiabatic potentials of the reactant and the product state will be (Fig. 3.4(a)):

$$U_r(Q) = \frac{\hbar\omega}{2} Q^2 \qquad (3.10a)$$

$$U_p(Q) = \frac{\hbar\omega}{2}(Q-\Delta)^2 + \Delta G \qquad (3.10b)$$

where $\Delta G = U_p(\Delta) - U_r(0)$ is the free energy of the ET reaction which is negative for exoenergetic reactions and Δ is the distance between the equilibrium reactant and product states in the nuclear reaction coordinate Q. We define the reorganization energy λ as the energy which the medium takes to bring the system from the reactant to the product state at $Q = 0$ without occurrence of ET. From Fig. 3.3(a) a physical meaning of the reorganization energy can be deduced: λ is the change in free energy required to move the reactant atoms to the product configuration and to move the solvent molecules as if they were solvating the products without actually transferring the electron (2λ corresponds to the optical stokes shift)

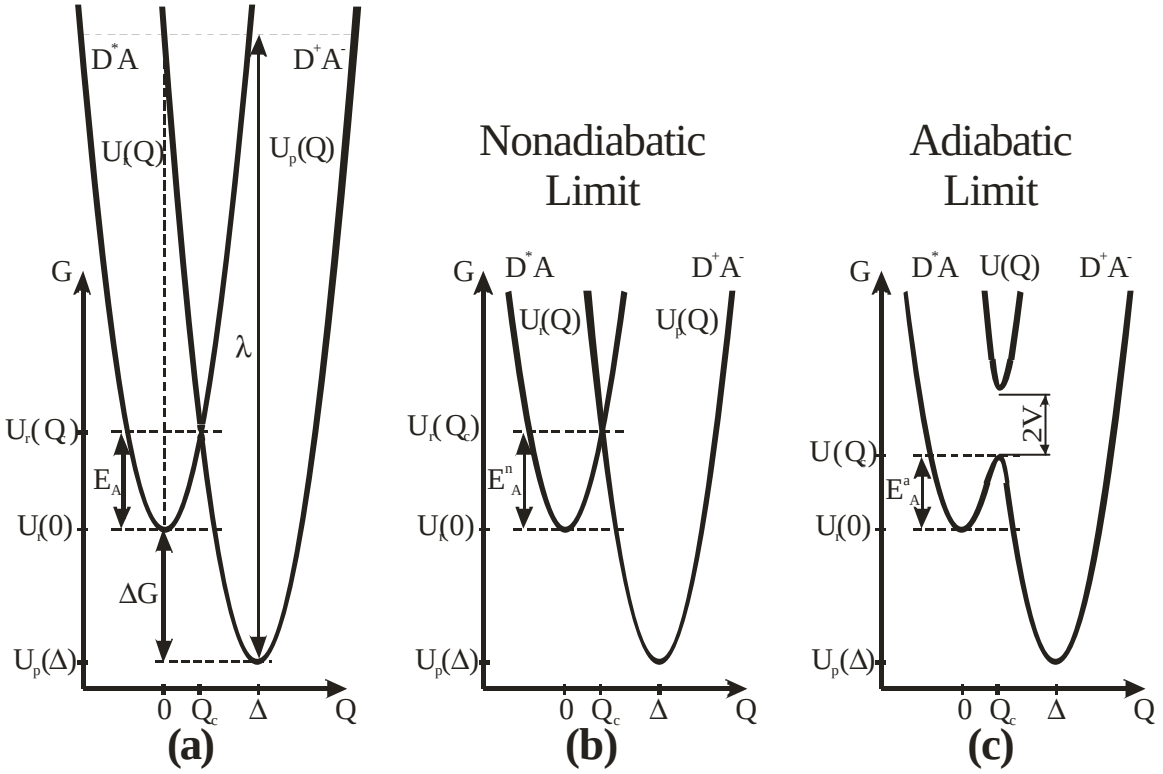

Fig. 3.3 Free energy curves for a donor acceptor complex in harmonic approximation. Q is the reaction coordinate. The definition of the driving force ΔG, the reorganization energy λ, and the free energy of activation Ea is indicated in (a). The diabatic or nonadiabatic limit and the adiabatic limit are shown in (b) and (c). The splitting of the potential in the adiabatic limit has a magnitude of 2V at the crossing point of the reactant and product diabatic potentials.

Then the ET could be interpreted as activated quantum mechanical process with an activation barrier of $E_A = U_r(Q_c) - U_r(0)$. If the system transition is nonadiabatic than the system passes

from a reactant adiabatic state to a product adiabatic state through the adiabatic point Q_c (Fig. 3.4a) with an activation energy:

$$E_A^n = \frac{(\Delta G - \lambda)}{4\lambda}, \tag{3.11}$$

while if the system is adiabatic that the ET occurs as a movement through a single potential $U(Q)$ (Fig. 3.4b). This potential is essentially determined by the reactant and the product diabatic potentials except close to the intersection point Q_c where it is strongly nonlinear and forms two surfaces separated by $2V$ and consequently the activation energy for the adiabatic ET will be:

$$E_A^a = \frac{(\Delta G - \lambda)}{4\lambda} - V . \tag{3.12}$$

In the single-mode approximation in the nonadiabatic limit the Franc-Condon factor employs the analytical form from the Marcus-Levich-Jortner equation:

$$FC = \frac{1}{\hbar\omega} e^{-S(2\nu+1)} I_p \left\{2S[\nu(\nu+1)]^{1/2}\right\} \left[\frac{\nu+1}{\nu}\right]^{p/2} \tag{3.13}$$

where I_p is the modified Bessel function of order $p = \Delta G/\hbar\omega$ where $\hbar$ is the Planck constant,

$$S = \frac{\Delta^2}{2} = \frac{\lambda}{\hbar\omega} \tag{3.14}$$

is the dimensionless vibrational coupling constant (Huang–Rhys factor) and

$$\nu = [exp(\hbar\omega/k_B T) - 1]^{-1} \tag{3.15}$$

is the temperature dependent Bose factor.

Practically important case appeared to be the case when $\Delta G = -\lambda$ (activationless case). Then the temperature dependence of the ET rate is[23]:

$$k = \frac{2\pi}{\hbar} \frac{|V|^2}{\hbar\omega\sqrt{2\pi S}} \sqrt{\frac{exp(\hbar\omega/k_B T) - 1}{exp(\hbar\omega/k_B T) + 1}} \tag{3.16}$$

Depending on the treatment of the nuclear degrees of freedom that contribute to the ET, electron transfer theories can be divided into quantum mechanical ($\hbar\omega >> k_B T$) and classical ($\hbar\omega << k_B T$) approaches.

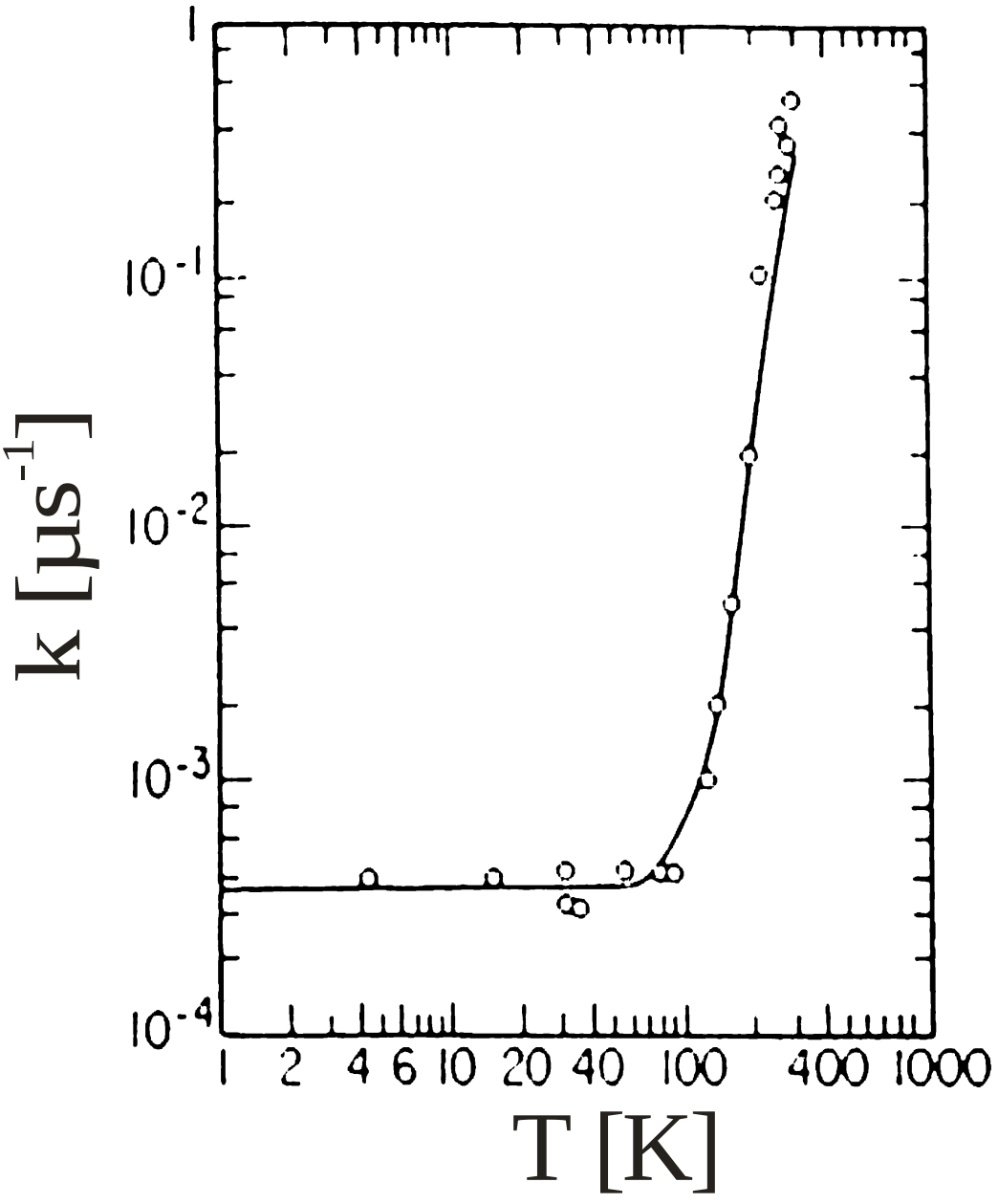

Fig. 3.4. Temperature dependence of the rate constant for electron transfer from cytochrome c to the oxidized special pair in the RC.

3.6. Quantum-mechanical nonadiabatic limit – nuclear tunneling

In the quantum mechanical nonadiabatic limit $k_B T << \hbar\omega$ the Frank-Condon factor is:

$$FC = \frac{1}{\hbar\omega} exp(-S)\frac{S^p}{p!} \tag{3.17}$$

and determine a temperature independent ET rate corresponding to a nuclear tunneling process from the initial reactant vibronic state to an isoenergetic product state. Such a process is observed in cytochrome c in photosynthetic bacterial reaction centers[19, 24] (see Fig. 3.4).

3.7. Classical nonadiabatic limit – Marcus theory

In the classical nonadiabatic limit $k_B T >> \hbar\omega$ this Frank-Condon factor is converging to the one derived first by Marcus.

$$FC = \frac{1}{\sqrt{4\pi\lambda k_B T}} e^{-E_A^n / k_B T} \tag{3.18}$$

and thus we obtained the Marcus

$$k = \frac{2\pi}{\hbar}\frac{V^2}{\sqrt{4\pi\lambda k_B T}} exp\left[-\frac{(\Delta G + \lambda)^2}{4\lambda k_B T}\right] \tag{3.19}$$

The transition temperature between the classical and the quantum mechanical limits is at

$$k_B T \approx \hbar\omega / 4 \tag{3.20}$$

For typical protein vibrational frequencies of $\hbar\omega \approx$ 100-300 cm^{-1} the transition temperature deviates between 35 and 100 K. Thus eq. (3.18) is valid for ET from a thermally equilibrated vibronic manifold of the donor acceptor potential surface, involving only the low frequency medium modes in the high-temperature (classical) limit[13]. It is most commonly used in describing the ET processes in the next chapters.

In eq. (3.2) k is expressed in terms of the reorganization energy λ and the free energy change of the reaction ΔG. Importantly, Eq. (3.18) predicts that the electron transfer rate decreases with increasing −ΔG for strongly exoenergetic reactions and advances a universal classification of ET reactions to normal (–ΔG < λ), activationless (–ΔG = λ), and inverted (–ΔG > λ) regions (Fig. 3.4)

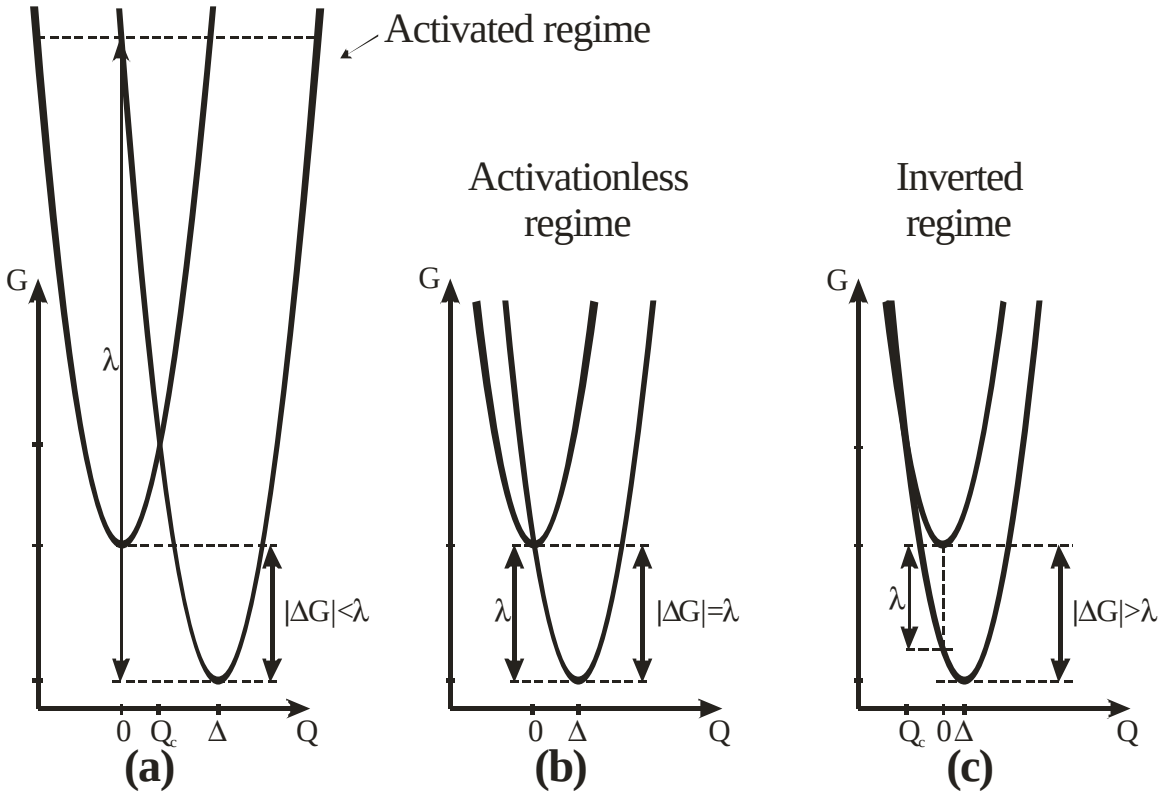

Fig. 3.5: (a) The normal region, (b) the activationless region, (c) and the inverted region of electron transfer in a donor-acceptor complex.

For photoinduced electron transfer reactions the free energy change ΔG can be calculated using the Rehm-Weller expression[25]:

$$\Delta G = E_{ox} - E_{red} - \Delta E_{00} + C \tag{3.21}$$

Here, E_{ox} is the oxidation potential of the ground-state donor, E_{red} is the reduction potential of the ground-state acceptor and ΔE_{00} is the zero−zero transition energy for optical excitation. To a first approximation, C is the Coulomb energy change resulting from ET between the donor and the acceptor.

3.8. Frank-Condon factor in multi-mode approximation

When the single mode approximation cannot represent the phonon spectrum sufficiently well as it is the case with complex molecules as proteins, we can represent the phonon spectrum by two modes. Low frequency mode $\hbar\omega_m < 300$ cm^{-1} covering the vibrational modes of the proteins and high frequency mode $\hbar\omega_a > 1000$ cm^{-1} representing the vibrations of small atomic groups as

C=C stretching mode. Such a representation of the phonon spectrum is called multi-mode approximation

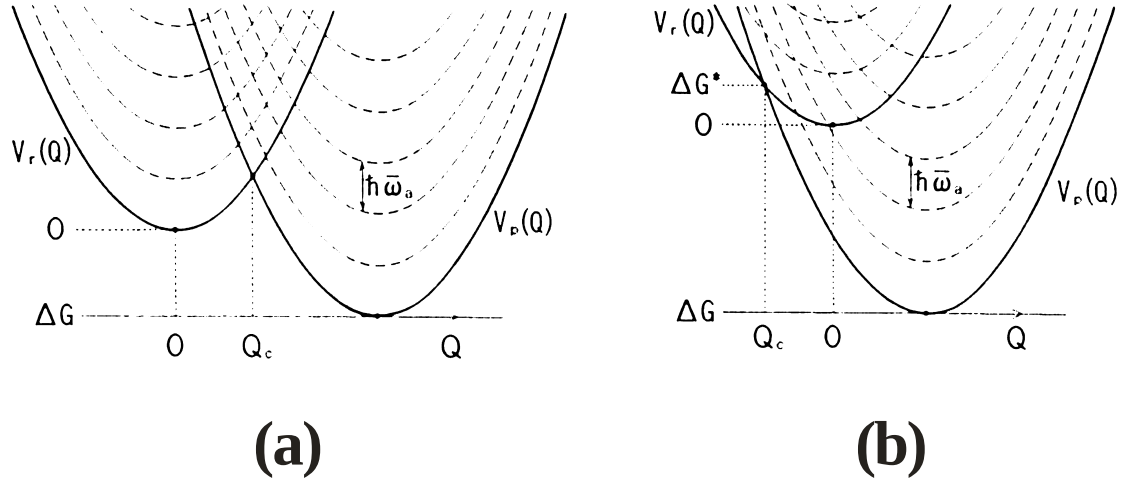

Fig. 3.6. The multiplication of the radical pair states in multimode approximation in (a) initially activated ET and (b) initially ET in the inverted region.

In the multi-mode approximation except the potential curve of the radical pair state D^+A^- we have a number of potential curves of the $(D^+A^-)_n$ states with energy higher than the initial radical pair state by $n\hbar\omega_a$ (see Fig. 3.6). Thus the ET rate in the multi-mode approximation obtains the form:

$$FC = \frac{1}{\hbar\omega_m} e^{-S_m(2\nu_m+1)-S_a(2\nu_a+1)} \cdot \sum_{n=-\infty}^{\infty} \left(\frac{\nu_m+1}{\nu_m}\right)^{p(n)/2} \cdot I_{|p(n)|}\left(2S_m\sqrt{\nu_m(\nu_m+1)}\right) \cdot \sum_{n=-\infty}^{\infty} \left(\frac{\nu_a+1}{\nu_a}\right)^{p(n)/2} \cdot I_{|p(n)|}\left(2S_a\sqrt{\nu_a(\nu_a+1)}\right) \tag{3.21}$$

where the phonon coupling constants S_m and S_a are defined as in eq. (3.14) and similarly the Bose factors ν_m and ν_a are defined as in eq. (3.15). The energy parameter here is $p = |-\Delta G - n\hbar\omega_a| / \hbar\omega_m$

In the low temperature limit eq. (3.21) obtains the form from eq. (3.17) and for high temperatures it converges to the Frank-Condon factor in the Marcus equation (eq. (3.18)). In the middle temperatures ($\hbar\omega_m/4 \langle\langle k_B T \langle\langle \hbar\omega_a/4$ equivalent to100 K < T < 500 K for RCs) the Frank-Condon factor in the multimode approximation obtains:

$$FC = \frac{1}{\sqrt{4\pi\lambda_m k_B T}} e^{-S_a} \cdot \sum_{n=-\infty}^{\infty} \frac{S_a{}^n}{n!} \cdot exp\left[-\frac{(\Delta G + n\hbar\omega_a + \lambda_m)}{4\lambda_m k_B T}\right] \tag{3.22}$$

In case two modes cannot represent the phonon distribution then the finite number of modes could be just added to the $k(-\Delta G)$ dependence shifted with $-\Delta G$[26] (see Fig. 3.7). Consequently for an infinite number of states as if the acceptor is an electrode (acceptor is attached to a macroscopic surface of a solid state material) will be present then the $k(-\Delta G)$ dependence would be flat in the inverted region. Such a theoretical prediction has been not yet confirmed experimentally.

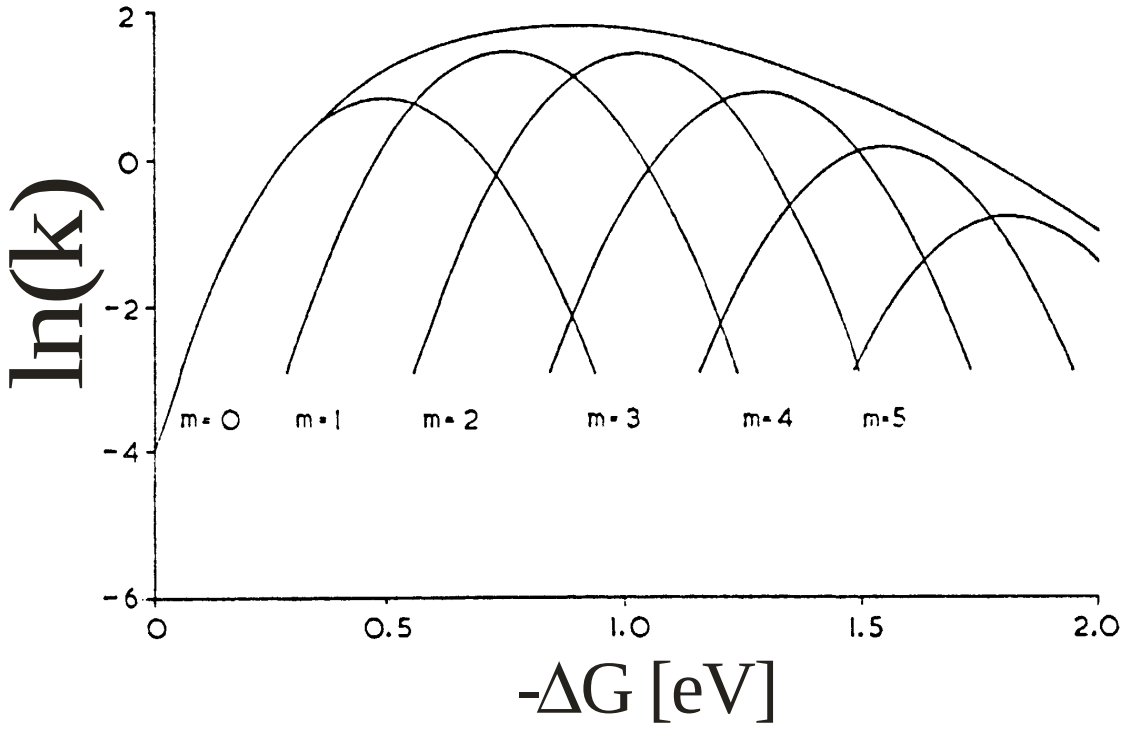

Fig. 3.7. ET to a finite number of modes as for each mode the rate is described by the Marcus equation. The overall rate is on top of the rates for each mode

In RCs the phonon spectrum is determined to have significant amplitudes between 80 and 160 cm^{-1}[27, 28] and therefore the single mode approximation or multimode approximation with small numbers of modes should be used for describing the ET kinetics.

It should be noted that around the activationless regime all of the different approximations, i.e. classical (Marcus equation), single-mode and multi-mode, will have similar behavior as it is evident from Fig. 3.8. Thus for simplicity we can use the Marcus formula for ET close to the activationless or slightly in the activated regime.

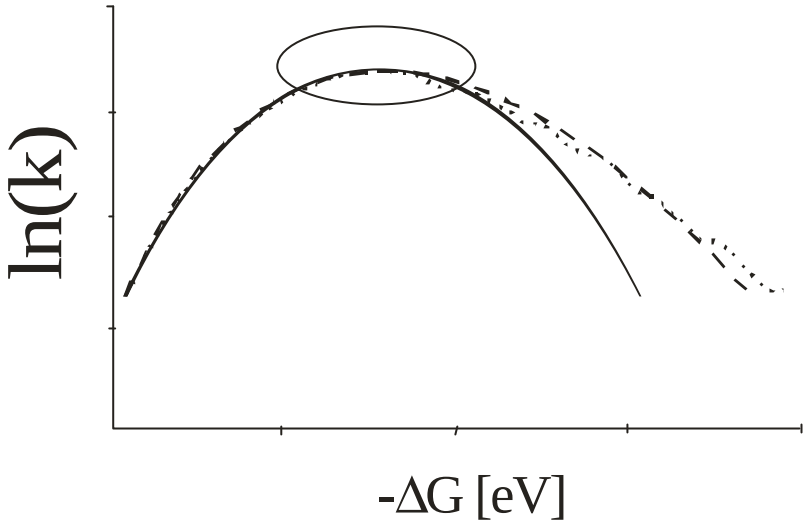

Fig. 3.8. (–Δ*G*) dependence of the natural logarithm of the observed rate constant at classical (solid line), single-mode (dashed line) and multi-mode approximation (dotted line).

3.9. Superexchange mediated electron transfer

In a variety of environments, e.g. in proteins, the rate of long-range (>5 Å) electron transfer has been shown to fall off exponentially with distance[21]:

$$V = V_0 \, exp\left[-\frac{\beta}{2}(R - R_0) \right] \tag{3.23}$$

If the separation exceeds the spatial extension of the wavefunctions of D and A, their direct interaction is negligible. Such long-range ET involves the mediation of the nonradiative process by the intervening molecular bridges (B), which control the process via electronic and/or vibronic coupling. For proteins and other insulating environments, there exists a large energy difference between the electronic origin of the DBA manifold and the energy of the oxidized state of the bridging medium (D^+B^-A). Consequently, coupling of the donor to the acceptor involves quantum mechanical tunneling of charge between a localized orbital on the donor and a localized orbital on the acceptor. The state D^+B^-A is virtual state that is not physically populated, i.e., the ET takes place in a single step[11].

For different classes of donor–acceptor systems β can vary substantially. The distance dependence of ET rates is especially well characterized in proteins. Reported β values typically fall in the range of 0.9–1.6 $Å^{-1}$[29, 30].

From the first perturbation theory in Quantum mechanics we can determine the coupling as[31]:

$$V = V_{DA} + \frac{V_{DB}.V_{BA}}{\delta E} \tag{3.24}$$

where the V_{DA} is the direct coupling between donor and acceptor and the remaining part of the total coupling is called superexchange coupling. The energy difference δE is the distance between the crossing point of the potentials of the donor and acceptor and the energy potential of the bridge state in the same reaction coordinate as depicted in Fig. 3.9.

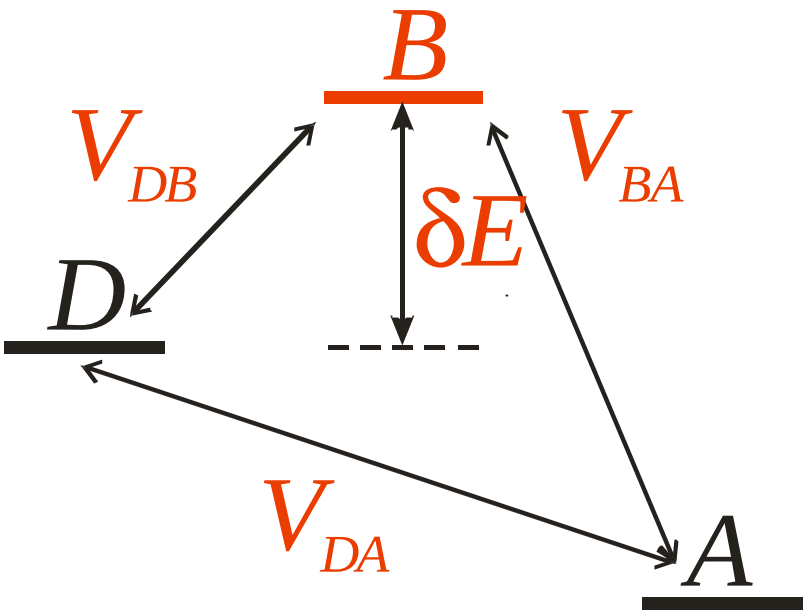

Fig. 3.9. Energetics of the donor bridge acceptor system with definition of δE.

The first perturbation theory is no longer valid as δE approaches 0. A limit of validity of eq. (3.24) is:

$$\delta E \geq \sqrt{3\lambda_{DS} k_B T} \tag{3.25}$$

4. Temperature dependence of the conformational relaxation of the state $P^+H_A^-$ in R26 reaction centers of *Rb. sphaeroides*

4.1. Introduction

Conformational flexibility is a distinctive feature of proteins and usually is of crucial importance for their function. At low temperature protein fluctuations are mainly restricted to harmonic motions with low amplitude around the conformations into which it is frozen. Above a typical dynamic transition temperature non-harmonic fluctuations involving barrier crossing between different conformations with significant structural changes dominate. This transition usually is intimately connected with functional activity of the protein. Nevertheless even at temperatures of ~4 K local rearrangement around pigment cofactors can occur on a very slow time scale as reflected in spectral diffusion experiments[32].

Various methods have been employed to investigate protein fluctuations and relaxations pertaining to different timescales or temperatures and reflecting different degrees of local or global properties. Fluctuations influence the area of the resonance lines in Mössbauer spectra, which depend on the mean square displacement of the iron atom as expressed by the Lamb Mössbauer factor. All motions faster than the nuclear lifetime (141 ns for ^{57}Fe) contribute. Various photophysical properties of intrinsic reporter molecules may report on the dynamic properties of their local environment via optical absorption (or emission) in the UV/VIS/IR. These properties are very specific to the individual molecules. Electron/phonon coupling to low frequency motions may show up as a Gaussian broadening of the absorption lines and e.g. in the case of the Soret band of heme proteins are related to vibrations of the iron perpendicular to the heme plane. Alternatively relaxation processes affecting the electrostatic interactions of the protein surrounding with the cofactor may directly be traced via the time dependent spectral shifts of optical transitions coupled to large changes of the dipole moment (e.g. charge transfer bands: CT-III band in myoglobin). Factors determining the time window accessible by optical methods are the lifetime of the excited state on one hand (usually in the order of nanoseconds, but considerably expandable if triplet states or long living photochemical products are involved) and inhomogeneous line broadening on the other hand. Limitations due to inhomogeneous line broadening may be overcome in low temperature hole burning experiments revealing slow scale spectral diffusion processes on timescales of minutes and longer.

In proteins with intramolecular charge transfer the interactions of the local surrounding with the dipole moment of a radical ion pair can be monitored on the delayed emission of the parent electron donor state revealing the change of free energy between them as a function of time[28,

[33-35]. It is evident that the solvent play significant role in the protein relaxation mechanisms. Different methods yield different behavior of the transition temperature on matrix conditions like sucrose/trehalose[36, 37], glycerol[28, 38], drying etc. Most of the methods demand a clear glass at low temperature for avoiding scattering problems. There are no clear interactions between the protein and the cryoprotectors or glass forming agents which are necessary for the low temperature investigations. Thus there is a great interest in investigation of the protein relaxation without such a protector. Freezing of the solvent matrix in absence of cryoprotector or glass forming agent is possible only when using the delayed fluorescence method[35] which will be described in this Chapter.

The photosynthetic reaction center RC with its well-resolved three-dimensional structure[39-43] and its plurality of electron transfer ET processes (see Fig. 1.2) is an ideal working model for investigating protein dynamics. The light-induced charge separation (CS) occurring within 3 ps induces sufficient perturbation of the charge distribution to trigger a detectable dynamic response of the protein. A series of subsequent CS and recombination processes between the various cofactors, which altogether cover a time window between 1 ps and several seconds[44-46] (see Fig. 1.2), serve as sensitive probes for detailed studies of this response. In particular, they can be utilized to explore the energetic relaxation of the CS states reflecting conformational changes in response to the charges moving between the cofactors. In spite of extensive investigations of the kinetics of essentially all ET reactions, dedicated investigations concerning details of protein action on the ET process and its response to charge separation are yet scarce and rather unclear. There is an increasing consensus, that after excitation of the primary donor P, a bacteriochlorophyll dimer, an electron is first transferred to the closest-lying cofactor, a bacteriochlorophyll monomer B_A in the protein A-branch[44-46] and then to a bacteriopheophytin H_A, before it proceeds to a quinone Q_A[47-50] and further to Q_B.

In the present chapter we will investigate the free energy relaxation of the bacteriopheophytin radical pair state $P^+H_A^-$ reflecting the conformational cooling of the R26 RC protein from *Rb. sphaeroides* using the method of delayed fluorescence described in the following section.

4.2. Method of discriminating between "prompt" emission of $^1P^*$ and "delayed" emission reflecting equilibrium with $P^+H_A^-$

The fluorescence of an excited state, which forms a long living intermediate like e.g. a charge separated state or a triplet state, will exhibit a main decay component with amplitude a_{prompt} reflecting equilibration between the two states, i.e. the decay of the excited state and the formation of the intermediate. Additionally to this fast or "prompt" emission component a slow

emission may be observed called "delayed", which reflects decay of the intermediate to the ground state. Its amplitude $a_{delayed}$ reflects the equilibrium which is established between the emitting parent state and the long living intermediate via the Boltzmann factor[51]:

$$\frac{a_{delayed}}{a_{prompt}} = exp\left(\frac{\Delta G}{k_B T}\right) \Big/ \left[1 + exp\left(\frac{\Delta G}{k_B T}\right)\right], \tag{4.1}$$

where k_B is the Boltzmann constant and T is the temperature of the system. Thus assuming single excited and intermediate states (for inhomogeneously broadened states see next section) we obtain access to the free energy difference ΔG between them:

$$\Delta G(t) = k_B \cdot T \cdot ln\left(\frac{a_{delayed}(t)}{a_{prompt} - a_{delayed}(t)}\right) \tag{4.2}$$

If ΔG changes with time due to a relaxation process, this should become evident from the time dependent amplitude. Since we are measuring at least five time constants in the reaction center discrimination between prompt and delayed emission is not straight forward and additional information is needed. Finger printing the contribution of delayed emission can be achieved in an elegant way, if it is possible to manipulate the lifetime of the intermediate state without affecting prompt fluorescence. In this case the delayed fluorescence should change its decay pattern, while the prompt fluorescence should remain unaffected. In the RC such a manipulation of the bacteriopheophytin radical pair state $P^+H_A^-$ can be achieved by extracting Q_A from the RC and reconstituting again. In the presence of Q_A the lifetime of $P^+H_A^-$ is 150-250 ps at 290 K and decreases to 80-100 ps at 85 K[52-55]. In the absence of Q_A the lifetime of $P^+H_A^-$ is 13-14 ns at 290 K and increases to 23-25 ns at 85 K[56-62].

The intensity of the delayed fluorescence is proportional to the product of the radiative rate k_F, and the equilibrium constant $^1P^* \leftrightarrow P^+H_A^-$ of the time dependent amplitude $a_{delayed}(t)$, and an exponential decay term accounting for the decay of $P^+H_A^-$ population, which is different in the two preparations. For the regime where *prompt* and *delayed emission* can be discriminated, i.e. when formation of $P^+H_A^-$ is fast compared to its decay and relaxation (this is valid for the vast majority of RCs) the total fluorescence can be written in very good approximation as:

$$\begin{aligned} F(t) &= F_{prompt}(t) + F_{delayed}(t) \\ &= F_{prompt}(t) + a_{delayed}(t) \cdot exp(-t/\tau_{P^+H_A^-}) \end{aligned} \tag{4.3}$$

with $F_{prompt}(t)$ being the decay of prompt emission, which may include any kind of not single exponential terms in order to account for dispersive charge separation[35]. We assume $F_{prompt}(t)$ to be identical in both preparations. We also assume that the energetic relaxation as reflected in $a_{delayed}(t)$ is the same in both preparations. Only $\tau_{P^+H_A^-}$, the lifetime of $P^+H_A^-$, is different in the Q_A-free (τ_{free}) and the Q_A-reconstituted (τ_{Q_A}) sample. Then we can eliminate F_{prompt} in (4.3) and obtain the time dependent amplitude:

$$a_{delay}(t) = \frac{F(t)_{free} - F(t)_{Q_A}}{exp(-t/\tau_{free}) - exp(-t/\tau_{Q_A})} \tag{4.4}$$

This amplitude reflects the free energy separation of $^1P^*$ and $P^+H_A^-$ and its relaxation behavior as a function of time. Now $F_{prompt}(t)$ and $F_{delayed}(t)$ can easily be obtained by inserting $a_{delayed}(t)$ into Equation (4.2).

4.3. Method for obtaining the free energy separation between $^1P^*$ and $P^+H_A^-$ in case of inhomogeneously broadened radical pair state

In RCs the excited special pair state $^1P^*$ is weakly broadened. Though its absorption and emission spectrum have bandwidths of about 1000 cm^{-1} (0.12 eV)[63], this broadening is mainly due to vibronic coupling. This explanation is corroborated by hole burning experiments, which reveal an inhomogeneous bandwidth of only 130 cm^{-1} (0.016 eV) [64]. Due to its large dipole moment the radical pair states $P^+B_A^-$ and $P^+H_A^-$ are expected to be broader[35] and to contribute significantly to inhomogeneity in the driving force for charge separation and to ΔG for $P^+H_A^-$. The variations in ΔG treated in the following reflect the difference between the free energies of $^1P^*$ and $P^+H_A^-$ and do not depend on the individual widths of these states.

When we have CS to an inhomogeneously broadened manifold of intermediate states it is not possible anymore to define a simple experimentally extractable free energy difference $\Delta G(t)$ between the donor and the intermediate state as in eq. (4.2). Adopting the formalism of eq. (4.2) for the inhomogeneous case we obtain an effective energy from the experimentally measured ration of $a_{delayed}/a_{prompt}$ which we call the apparent free energy difference $\Delta G_{app}(t)$. It does not correspond to a simple average of populations of the system. In the following we will derive ways of treating this experimentally accessible parameter in order to gain information about the true average value of ΔG and of the width of its distribution

In order to take into account the inhomogeneous broadening of the radical pair energy we calculate the experimentally obtained average amplitude of the delayed fluorescence as an

integral over the $^1P^*$ population expressed by the Boltzmann factor weighed with the distribution function of radical pair free energies $\rho(\Delta G)$. For positive ΔG the "delayed emission" is not defined and we only get fluorescence times faster than charge separation because the forward ET is becoming slower than the backward ET. Therefore we integrate only for negative free energy differences between the donor state and the acceptor manifold of states.

$$\frac{a_{delayed}}{a_{prompt}} = \int_{-\infty}^{0} \rho(\Delta G) \frac{e^{\frac{\Delta G}{k_B T}}}{1 + e^{\frac{\Delta G}{k_B T}}} d(\Delta G) \tag{4.5}$$

In absence of inhomogeneous broadening the radical pair free energy distribution is simply a delta function and eq. (4.5) is replaced by eq. (4.1). In lack of any further knowledge on the shape of the distribution function we assume a Gaussian distribution for $\rho(\Delta G)$. According to molecular dynamics simulations this seems to be a good approach[28, 65-67]:

$$\rho(\Delta G) = \rho_{Gauss}(\Delta G, \Delta G_0, \sigma) = \frac{1}{\sqrt{2\pi}\sigma} e^{-\frac{(\Delta G - \Delta G_0)^2}{2\sigma^2}}, \tag{4.6}$$

ΔG_0 is the mean value $\langle \Delta G \rangle$ or center of gravity of the distribution and σ is the half width.

Thus a relation between the experimentally extractable apparent free energy ΔG_{app} and the mean value ΔG_0 and the half width σ of the Gaussian distribution of intermediate state free energies can be obtained via importing eq. (4.4) in eq. (4.5):

$$\Delta G_{app}(\Delta G_0, \sigma, T) = k_B T \ln \left[\frac{\int_{-\infty}^{0} \frac{1}{\sqrt{2\pi}\sigma} e^{-\frac{(\Delta G - \Delta G_0)^2}{2\sigma^2}} \cdot \frac{e^{\frac{\Delta G}{k_B T}}}{1 + e^{\frac{\Delta G}{k_B T}}} d(\Delta G)}{1 - \int_{-\infty}^{0} \frac{1}{\sqrt{2\pi}\sigma} e^{-\frac{(\Delta G - \Delta G_0)^2}{2\sigma^2}} \cdot \frac{e^{\frac{\Delta G}{k_B T}}}{1 + e^{\frac{\Delta G}{k_B T}}} d(\Delta G)} \right] \tag{4.7}$$

Unfortunately this relation can be treated only numerically. An approximated formula for the inverse function $\Delta G_0[\Delta G_{app}, \sigma, T]$ was obtained in Appendix A via fitting of numerical simulations of eq. (4.7):

$$\Delta G_0(t) = \Delta G_{app}(t) - \frac{\sigma(t)^2}{2k_BT} + \left(\Delta G_0^{max}[\sigma(t)] - \Delta G_{app}^{max}[\sigma(t)] + \frac{\sigma(t)^2}{2k_BT} \right) \cdot \left\{ 1 - erf\left[\sqrt[3]{\frac{\left\{\Delta G_{app}(t) - \Delta G_{app}^{max}[\sigma(t)]\right\}^2}{27\sigma(t)k_BT}} \right]^2 \right\} \quad (4.8)$$

Note that such an approximate solution (or its asymptotic solution[35] eq. (B5) in the Appendix B) gives a straightforward dependence between the apparent free energy and the mean value and the half width of the distribution of free energies of the radical pair state at each moment t and at each temperature T. Thus by extracting the time and temperature dependent values of the apparent free energy from fluorescence data by the procedure described above, we can follow the relaxation of the free energy of the radical pair, with time and temperature in terms of both free energy mean value and width, as time and temperature dependent functions.

4.4. Obtaining the time dependence of the free energy separation between $^1P^*$ and $P^+H_A^-$

Fluorescence decay traces were collected with a time-correlated single-photon-counting apparatus described in Chapter 2. The samples were excited with a laser diode at 864 nm Hamamatsu PLP-01: pulse width 40 ps, energy 2 pJ, repetition rate 10 MHz of which 50% was focused to an area of 3 mm^2 resulting in an average turnover rate of 0.5 and a ground state bleaching of less than 5% due to accumulation of $P^+Q_A^-$. The dependence of the fluorescence decay on actinic intensity up to 0.1 W/cm^2 was investigated by exciting with a Ti:Sapphire laser Coherent, Mira 900B, 865 nm, pulse width 70 fs, energy 6 nJ, repetition rate 76 MHz pumped by an Ar-laser Coherent Innova 425. Amplified spontaneous emission in the excitation laser beams was suppressed with suitable spectral filters. The emission collected from the sample at 90° to the excitation beam was spectrally filtered at 920"5 nm Schott DAD 8-2 achieving a rejection for 864 nm stray light of 10^4. The fluorescence was detected with a MCP-photomultiplier equipped with a selected S1 cathode Hamamatsu, R2809-U cooled to 190 K. We found that beam polarization does not change the measured decay, in accordance with a rotational depolarization time of 90 ns for reaction centers in aqueous buffer [68]. The instrumental response function IRF was 40 ps full width at half maximum. The fluorescence was measured at seven different temperatures (85, 120, 160, 200, 220, 240 and 280 K) and two time windows (33 and 66 ns).

Time constants are extracted from the fluorescence decay pattern by fitting a convolution of the instrumental response function and 6 exponential decay functions to the data using the Levenberg–Marquardt method[7]. Deconvolution of Q_A - free and Q_A - containing RCs was done

simultaneously in a global analysis with *common* lifetimes and with *individual* amplitudes as free running parameters at each temperature and simultaneously for the two time windows.

The first two time constants and the ratios between the first and the second amplitudes were fixed in the fits because they were below the experimental time resolution. For 298 K and 82 K their values were taken from upconversion measurements with sufficient time resolution[69, 70]. Data at temperatures in between are available form Fleming et al.[71]. There only one single time constant was determined, which we associate to the average time $\tau_a = (\tau_1 A_1 + \tau_2 A_2)/(A_1 + A_2)$. These experimental data were well reproduced by a single mode approximation for the activationless case, which we use for interpolation of τ_a to the temperatures used in our experiment:

$$\tau_a(T) = \tau_a^0 \left[\frac{exp\left(\frac{\hbar\omega_a}{k_B T}\right) + 1}{exp\left(\frac{\hbar\omega_a}{k_B T}\right) - 1} \right]^{1/2} \tag{4.9}$$

Since the dominant first time constant τ_1 is expected to activationless we interpolate the 298 K and 82 K values by the same expression:

$$\tau_1(T) = \tau_1^0 \left[\frac{exp\left(\frac{\hbar\omega_1}{k_B T}\right) + 1}{exp\left(\frac{\hbar\omega_1}{k_B T}\right) - 1} \right]^{1/2} \tag{4.10}$$

where τ_1^0, τ_a^0, ω_1 and ω_a were determined from the available experimental data. For the second time constant resulting from the energetic inhomogeneity of the primary charge separation in RCs we checked two different approximation functions of the temperature dependence: (i) an Arrhenius type temperature activation

$$\tau_2(T) = A_{\tau 2}\, exp\left(\frac{E_{\tau 2}}{k_B T}\right) \tag{4.11}$$

(ii) a linear interpolation with $\frac{1}{T}$:

$$\tau_2(T) = \tau_2(85K) + \frac{\tau_2(85K) - \tau_2(298K)}{\frac{1}{85} - \frac{1}{298}}\left(\frac{1}{T} - \frac{1}{298}\right), \tag{4.12}$$

where τ_2 and $A_{\tau 2}$ were determined from the data at 298 K and 82 K. From these data finally temperature dependent ratio between the first and the second amplitude can be determined:

$$\frac{A_2(T)}{A_1} = \frac{\tau_a(T) - \tau_1(T)}{\tau_2(T) - \tau_a(T)}, \tag{4.13}$$

Differences in the method of interpolation for τ_2 and consequently A_2 using eq. (4.11 - 4.13), did not play a noticable role in the extraction of the apparent free energies.

The initial amplitude of the prompt fluorescence was taken to be:

$$a_{prompt}(T) = \sum_{i=1}^{6} A_i^{Q_A}(T) \tag{4.14}$$

The time dependent amplitude of the delayed fluorescence was taken as in eq. (4.4):

$$a_{delay}(t,T) = \frac{\sum_{i=1}^{6} \left(A_i^{free}(T) - A_i^{Q_A}(T)\right) exp(-t/\tau_i(T))}{exp(-t/\tau_{free}(T)) - exp(-t/\tau_{Q_A}(T))}, \tag{4.15}$$

The temperature dependences of the radical pair lifetimes have been taken from the literature. The temperature dependence of the radical pair lifetime of the Q_A-reconstituted RCs has been measured via transient absorption by Kirmaier et al.[54]. In this reference the Kakitani and Kakitani[72] model was used to fit the experimental values and the following interpolation formula is deduced according to the fit values presented therein:

$$\tau_{Q_A}(T) = 16.7 \cdot \frac{\Gamma[P(T)+1]}{0.6^{P(T)}}, \text{ where } P(T) = 1.11 + 1.55 \cdot \left(\frac{1}{2} + \frac{1}{exp(360/T)-1}\right), \tag{4.16}$$

$\Gamma[P(T)+1]$ is the gamma function, the lifetime τ_{QA} is in ps and the temperature T is in K.

The temperature dependence of the $P^+H_A^-$ radical pair lifetime of the Q_A-free RCs has been taken from the recombination data in Volk et al.[56]. These lifetimes do not directly correspond to rates, since they are governed by complex spin dependent recombination dynamics. Nevertheless the inverse lifetimes behave like an activated Marcus type rate, however exhibiting different activation barriers above and below 200 K. Therefore the data are best interpolated with a combination of two Marcus type rates in the two temperature ranges:

Table 4.1. Fits of $\Delta G_0(\Delta G_{app})$ relation using the function from eq. (4.8) for a set of temperatures where the lifetime τ_{free} is in ns and the temperature T is in K. For the temperatures of 200 K and 220 K the lower value from both formulas presented in eq. (4.17) was taken. A possible heterogeneity of the radical pair lifetimes will be discussed later.

σ [eV]	T [K]	85	120	160	200	220	240	280
0.015	$\chi^{(2)}$ [10^{-6}]	0.37	0.18	0.17	0.47	0.84	1.4	3.2
	k	11	8.6	6.1	4.8	4.5	4.0	3.6
	p_1	0.59	0.51	0.41	0.35	0.33	0.29	0.25
	p_2	0.75	0.86	1.1	1.37	1.42	1.73	2.1
0.020	$\chi^{(2)}$ [10^{-6}]	0.64	0.44	0.38	0.19	0.28	0.37	0.89
	k	11	9.3	7.2	5.8	5.2	4.8	4.1
	p_1	0.63	0.58	0.50	0.44	0.40	0.37	0.33
	p_2	0.71	0.76	0.90	1.0	1.2	1.3	1.5
0.025	$\chi^{(2)}$ [10^{-6}]	0.96	0.73	0.65	0.48	0.41	0.36	0.60
	k	9.3	9.1	7.8	6.5	5.9	5.4	4.7
	p_1	0.65	0.62	0.56	0.50	0.47	0.44	0.39
	p_2	0.69	0.72	0.80	0.90	0.96	1.0	1.2
0.030	$\chi^{(2)}$ [10^{-6}]	1.5	1.0	1.1	1.0	0.91	0.80	0.68
	k	8.1	8.3	7.8	6.8	6.3	5.9	5.1
	p_1	0.66	0.64	0.60	0.55	0.52	0.50	0.45
	p_2	0.68	0.70	0.73	0.81	0.85	0.90	1.0
0.035	$\chi^{(2)}$ [10^{-6}]	2.1	1.4	1.2	1.0	0.93	0.84	0.68
	k	7.1	7.5	7.4	6.9	6.5	6.2	5.5
	p_1	0.66	0.65	0.62	0.58	0.56	0.54	0.50
	p_2	0.68	0.69	0.72	0.76	0.79	0.82	0.90
0.040	$\chi^{(2)}$ [10^{-6}]	2.9	1.8	1.3	1.3	1.2	1.1	0.96
	k	6.3	6.8	7.0	6.7	6.5	6.2	5.6
	p_1	0.67	0.65	0.64	0.61	0.59	0.57	0.54
	p_2	0.67	0.69	0.70	0.73	0.75	0.77	0.83
0.045	$\chi^{(2)}$ [10^{-6}]	39	23	18	15	14	13	12
	k	5.6	6.1	6.4	6.3	6.3	6.1	5.7
	p_1	0.68	0.66	0.64	0.62	0.61	0.60	0.57
	p_2	0.66	0.68	0.70	0.72	0.73	0.74	0.78

$$\tau_{free}(T) = \begin{cases} \dfrac{\sqrt{T}}{0.988\,exp(-144/T) + 0.321\,exp(-43.2/T)}, & T \le 185\ K \\ \dfrac{\sqrt{T}}{8.23\,exp(-602/T) + 0.259\,exp(+14.4/T)}, & T \ge 230\ K \end{cases}, \qquad (4.17)$$

Using eq. (4.5) the time dependence of the ΔG_{app} was extracted from the delayed fluorescence amplitude $a_{delayed}(t)$. $G_0(t)$ was deduced from thus obtained $\Delta G_{app}(t)$ using eq. (4.8).
The half width σ of the Gaussian distribution of the radical pair free energy was assumed time and temperature independent. In case of time and/or temperature dependence of σ is introduced the approximated formula from eq. (4.8) should be used.

4.5. Time-resolved temperature dependent fluorescence data

The decay of the spontaneous fluorescence of the $^1P^*$ state of Q_A-containing RCs $F(t)_{Q_A}$ is shown in Fig. 4.1a, 4.1b, and that of Q_A-depleted $F(t)_{free}$ in Fig. 4.1c, 4.1d. As mentioned above in the presence of Q_A the lifetime of $P^+H_A^-$ is 150-250 ps at 280 K and decreases to 80-100 ps at 85 K [52-55] following the temperature dependence from eq. (4.16)[54]. In the absence of Q_A the lifetime of $P^+H_A^-$ is 13-14 ns at 290 K and increases to 23-25 ns at 85 K[56-62] following the temperature dependence from eq. (4.17)[56]. As expected, the fluorescence traces of Q_A shows additional emission in the 10 ns range originating from delayed emission of $P^+H_A^-$. In order to obtain this part of the emission in the fits correctly we have measured the fluorescence in relatively long time window (66 ns) thus spanning 5-6 times the longest component in the fluorescence traces. It was necessary to measure the fluorescence in a shorter time window as well (33 ns was the shortest possible with our system) in order to resolve the fast fluorescence components as good as it is possible with the instrumental response function of ~40 ps. Global fits of the both time windows retained the correct relation between the fast and the slow components.

Fits of individual decay traces do not converge to a unique set of time constants, which rather depend on the amount of components and the choice of starting parameters and convergence criteria. Apparently these time constants do not represent kinetically distinct states of the system, but should be regarded as a simple phenomenological description of a more complex decay of $^1P^*$[28]. In order to allow a direct quantitative comparison of the fluorescence decay traces of Q_A-free and Q_A-containing RCs (Table 4.2) we have employed a global fitting procedure, assuming an identical set of time constants (τ_i) for both samples but allowing for different amplitudes (A_i^{free} and $A_i^{Q_A}$) and σ:

Table 4.2. Results of the fit with six exponential functions of the time decay patterns of Q_A - free and Q_A - containing RCs in Fig. 4.1, which were done simultaneously in a global analysis with *common* lifetimes τ_i and with *individual* amplitudes A_i^{free} and $A_i^{Q_A}$, respectively, as free running parameters at each temperature and simultaneously for the short (33 ns) and long (66 ns) time windows. (i = 1..6)

T [K]→	85	120	160	200	220	240	280
$\chi^{(2)}$	1.26	1.24	1.04	1.09	1.07	1.03	1.17
τ_1 [ps]	1.44	1.59	1.76	1.93	2.01	2.08	2.24
τ_2 [ps]	10.5	8.88	8.02	7.55	7.39	7.25	7.04
τ_3 [ps]	158	152	146	144	119	89.8	83.6
τ_4 [ps]	527	605	687	772	669	514	659
τ_5 [ns]	2.55	3.01	3.18	3.75	3.03	2.59	3.32
τ_6 [ns]	16.2	15.0	15.5	15.8	14.2	11.5	11.3
A_1^{free} [a.u.]	100	100	100	100	100	100	100
A_2^{free} [a.u.]	10.5	12.8	15.3	17.9	19.3	20.7	23.7
A_3^{free} [a.u.]	9.19	8.14	4.87	4.56	7.01	6.93	1.41
A_4^{free} [a.u.]	2.57	1.99	1.38	1.60	2.09	1.53	0.177
A_5^{free} [a.u.]	0.137	0.202	0.233	0.276	0.439	0.259	0.0512
A_6^{free} [a.u.]	0.0193	0.0413	0.0526	0.0663	0.0819	0.0475	0.0147
$A_1^{Q_A}$ [a.u.]	100	100	100	100	100	100	100
$A_2^{Q_A}$ [a.u.]	10.5	12.8	15.3	17.9	19.3	20.7	23.7
$A_3^{Q_A}$ [a.u.]	4.70	4.09	3.35	2.73	1.97	4.70	1.56
$A_4^{Q_A}$ [a.u.]	0.828	0.740	0.679	0.396	0.225	0.313	0.0579
$A_5^{Q_A}$ [a.u.]	0.0272	0.0542	0.0706	0.0549	0.0335	0.0177	0.00109
$A_6^{Q_A}$ [a.u.]	0.000805	0.00363	0.00435	0.00507	0.00294	0.00131	0.0000714

The fastest two components of the fit and their amplitudes have been held fixed. So far this lifetimes are taken to be *independent* of the presence of Q_A, though a reliable comparative subpicosecond study of the $^1P^*$ lifetime in Q_A-free and Q_A-containing RCs is lacking. Since there are reliable high time resolution measurements of the $^1P^*$ decay at two temperatures only, i.e. at 298 K[69] and at 82 K[70] we have interpolated the fast decay parameters as described in the previous section. The amplitude of the fastest component was normalized to 100 in both preparations. The other amplitudes are given in relative units.

Some preliminary fluorescence upconversion measurements of Q_A-free RCs at 280 K[2] indicate an increase of the τ_1 value by ~30% as compared to the data for Q_A-containing RCs[73-82] However, the variation of the published values does not allow to safely conclude that the main

decay component of $^1P^*$ differs in Q_A-depleted and Q_A-containing RCs. Even in reduced RCs with an excess charge on Q_A, charge separation seems to slow down only subtly, much less than one might expect from the repulsion of charges on B_A^- and Q_A^- indicating that dielectric shielding has to be significant.

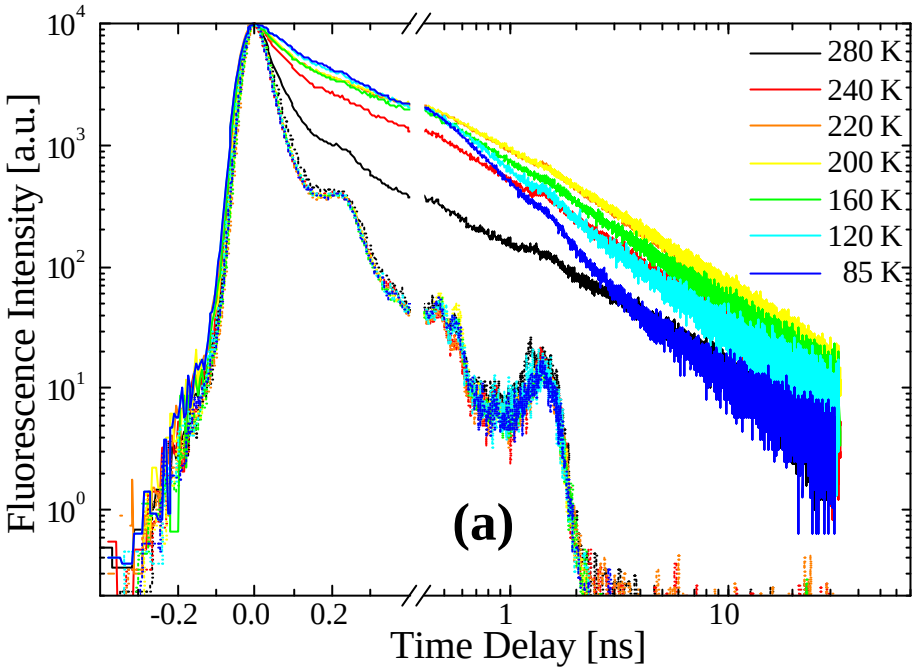

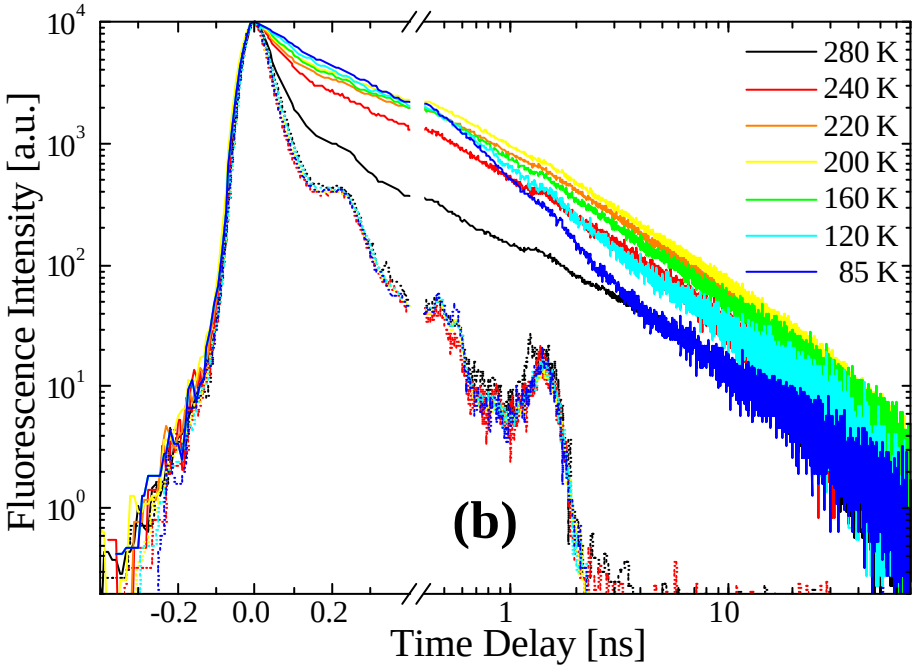

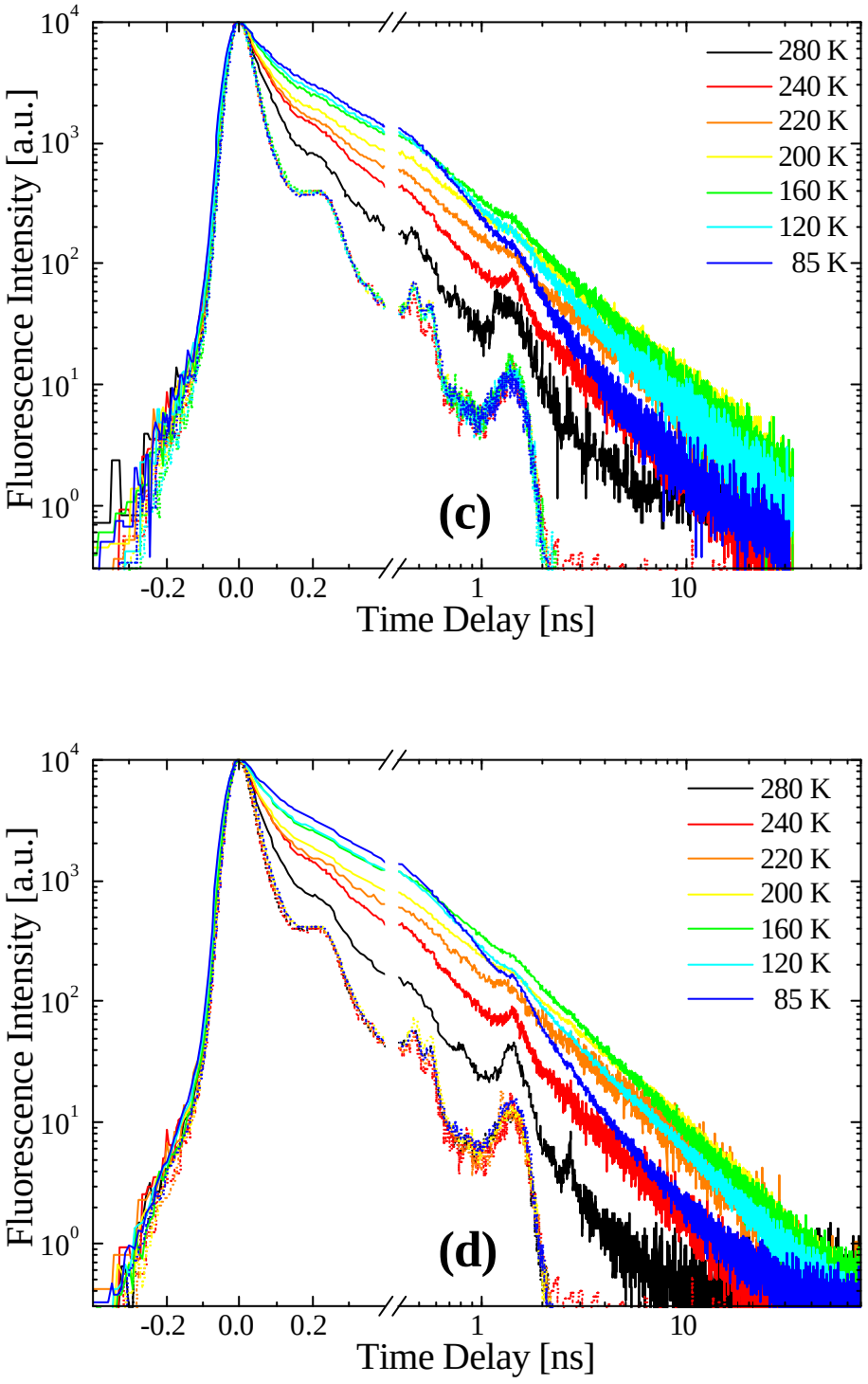

Fig. 4.1. Time resolved fluorescence of R26 *Rb. sphaeroides* RCs upon excitation at 864 nm and at different temperatures. In (a) and (b) are presented fluorescence decays of Q_A-free RCs at short (33 ns) and long (66 ns) time windows, respectively. In (c) and (d) are presented fluorescence decays of Q_A-reconstituted RCs at short and long time windows, respectively. The corresponding instrumental response functions are given with dotted lines in the same color as the fluorescence decays.

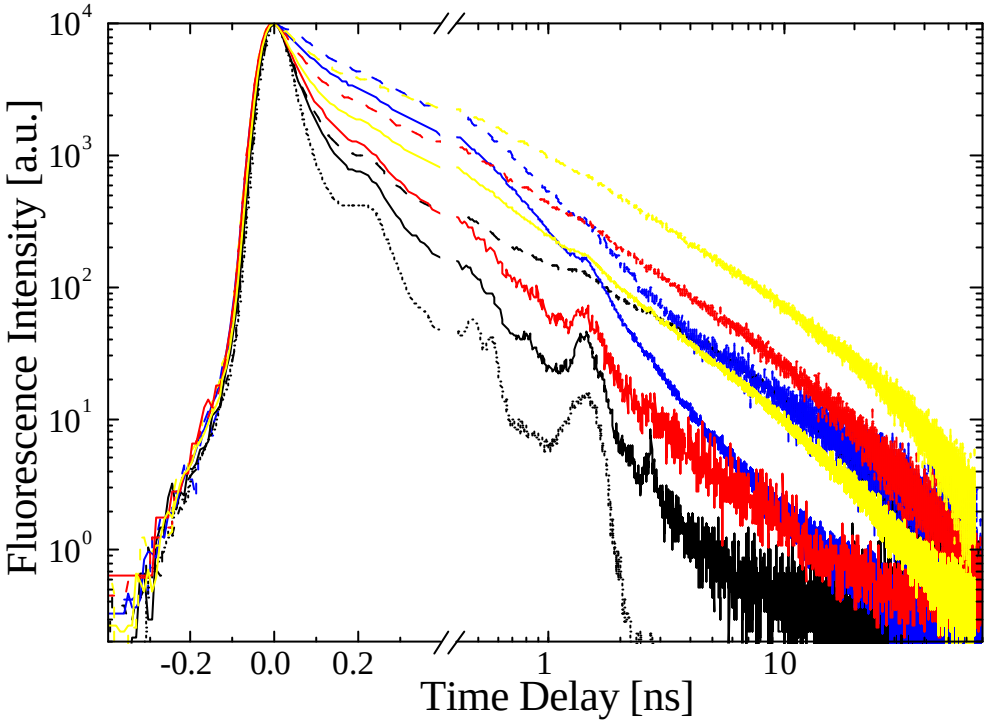

Fig. 4.2. Time resolved fluorescence of Q_A-free (dashed lines) and Q_A-reconstituted (solid lines) R26 *Rb. sphaeroides* RCs at 280 K (black), 240 K (red), 200 K (yellow) and 85 K (blue). A typical instrumental response function (IRF) is given with black dotted line.

The manipulation of the $P^+H_A^-$-lifetime by the presence or absence of Q_A leads to marked differences in the fluorescence decay pattern of $^1P^*$ (Fig. 4.1 and Fig. 4.2). At 280 K the normalized decay traces follow one another closely during the first 100 ps while at longer times the Q_A-containing sample decays more rapidly than the Q_A-free sample. At 280 K the global fit of the decay traces (Table 4.2) reveals that the amplitude of the third component with a time constant of 83.6 ps is essentially identical in both samples. The 659 ps component in the Q_A-containing sample - in which no $P^+H_A^-$ should remain present at this time - is smaller by a factor of ~3 than in the Q_A-depleted sample, in which $P^+H_A^-$ has not yet recombined. The presence of $P^+H_A^-$ has a more dramatic influence on the amplitudes of the 3.3 ns and 11 ns components, which are larger by factors of 50 and 200, respectively. The 11 ns component approximately follows the decay of $P^+H_A^-$[35]. The associated amplitude reflects the equilibrium constant, which bears information about the free energy difference between $^1P^*$ and $P^+H_A^-$ during the recombination of $P^+H_A^-$. This 11 ns component is essentially absent when Q_A is reconstituted with the exception of a remaining weak emission which corresponds to a residual Q_A-free fraction. The fraction of RCs resisting Q_A reconstitution could be determined independently by comparing nanosecond, microsecond and millisecond absorption transients as described in[83].

Fraction of <1% was measured for the sample on Fig. 4.3. A comparison between the fluorescence at 85 K for Q_A-free and Q_A-reconstituted RCs from different preparations and in different solutions is given in Fig. 4.3. The differences are minor and could be attributed to deviations in the preparations and in the RC source.

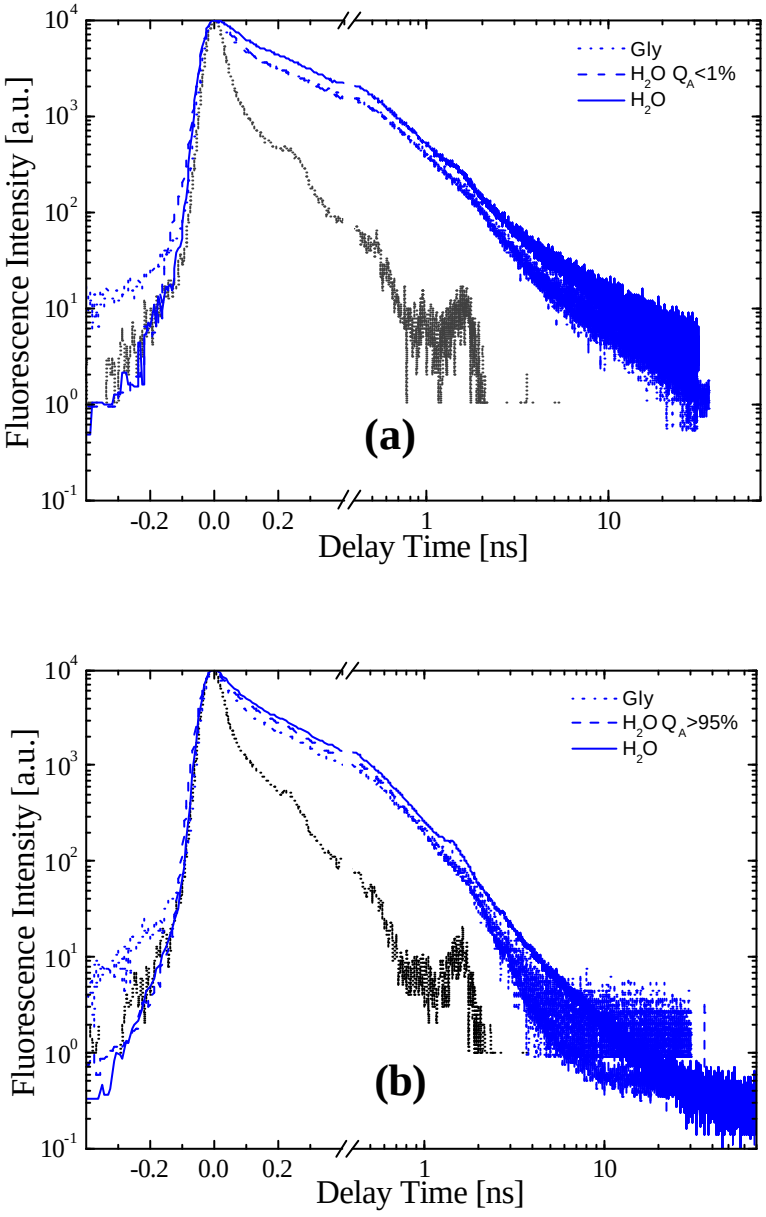

Fig. 4.3. Comparison between Q_A-free (a) and Q_A-reconstituted (b) samples at 85 K from different preparations. The fluorescence of the measured RCs dissolved in aqueous buffer in the present chapter is with solid lines. The Q_A-reconstituted sample is at 10 times higher concentration of LDAO in comparison with the Q_A-free one. With dashed lines are the fluorescence of the measured RCs dissolved in aqueous buffer and characterized as >95% Q_A content for the Q_A-reconstituted sample and <1% Q_A content for the Q_A-free sample[35]. With dotted lines are the fluorescence of RCs dissolved in 40 % aqueous buffer and 60% Glycerol mixture.

In Fig. 4.2 the fluorescence decay patterns of Q_A-depleted (solid lines) and Q_A-reconstituted (dashed lines) reaction centers are compared at 280 K (black lines), 240 K (red lines), 200 K (yellow lines) and 85 K (blue lines). Below the freezing point of the solvent at 260 K the decay traces of both samples follow one another closely at very early times. In the intermediate time window, i.e. from 80 ps to 700 ps, the decays of both samples are considerably slower than at 280 K and are becoming even slower with decreasing temperature. This is reflected in an increase of the amplitudes of the intermediate components given in Table 4.1, which grow in both preparations by a factor of 3-5 on lowering the temperature to 240 K. The third component slows down from τ_3=100 ps to 150 ps at 85 K while the amplitude for the Q_A-reconstituted RCs stays almost constant and the amplitude for the Q_A-free RCs increases slightly. The forth component with τ_4=600 ps shows a more complicated thermal behavior. Its amplitudes remain constant with temperature in both samples while its time constant exhibits a maximum around 200 K and then decreases reaching its value at 240 K again at 85 K. This behavior does not originate from the delayed fluorescence and seems to reflect the interplay between slow charge separation and internal conversion. In the nanosecond range the Q_A-containing sample decays more rapidly at all temperatures than the Q_A-free sample pointing to the dominant role of the delayed fluorescence in the latter sample. At 240 K the amplitude of the 3 ns component is larger by a factor of ~15. This factor decreases constantly with temperature to ~5 at 85 K. The amplitude of the 12 ns component is larger by a factor of ~35 in the absence of Q_A. It then slows down to ~ 15 ns and the ratio of the amplitudes of the both samples constantly decreases with temperature from ~30 at 220 K to ~25 at 85 K. It is important to note that the slowest ns delayed emission component of the Q_A-free sample has an unexpectedly weak temperature dependence before it freezes out below 70 K[33, 84].

It is evident from the fluorescence of the Q_A-reconstituted sample that the prompt emission has slow components beyond the internal conversion cutoff of less than 1 ns. As it is proposed from Ogrodnik et al.[35] this feature is due to a slow primary charge separation in a small minority of reaction centers. Indeed one would expect a slow tail of the electron transfer rates up to $k \rightarrow 0$ as a consequence of an inhomogeneous distribution of activation energies[85]. Of course we do not expect slower components than allowed by concurrent processes as excited state decay via internal conversion, superexchange enhanced ET to bacteriopheophytin as primary donor (investigated in the next two chapters) and fluorescence. Thus we attribute any slower components to a minority of RCs which refrained Q_A reconstitution.

4.6. Temperature and time dependent $P^+H_A^-$ free energy relaxation data

As shown in Fig. 4.2 the solid lines corresponding to the fluorescence of Q_A-containing RCs remain below the dashed lines corresponding to Q_A-free RCs after ~80 ps. This difference is attributed to the delayed fluorescence and consequently its contribution to the overall emission grows after ~80 ps. Nevertheless, in absolute terms, the delayed amplitude $a_{delayed}(t)$ decreases with time as can be estimated from Table 4.2. In Table 4.3 the temperature dependent differences between the different amplitudes of the fluorescence decays fits of Q_A-containing RCs and those of Q_A-free RCs are given. They are related to the amplitude of the first component in Table 4.2 and are presented in %. Thus the time dependent delayed fluorescence could be expressed in series of four exponents with time constants taken from Table 4.2 and divided by the difference of the time dependent exponents with time constants of the $P^+H_A^-$ radical pair lifetimes in the both samples according to eq. (4.15).

As mentioned in Chapter 4.5 the extraction of the prompt emission $F_{prompt}(t)$ and the delayed emission amplitude $a_{delayed}(t)$ from the experimental data is based on the working hypothesis that these quantities are identical in both samples. According to Fig. 4.1 $F(t)_{free}$ and $F(t)_{QA}$ are very similar to one another at early times. Obviously this reflects the similarity of the dispersive CS kinetics in both samples. Apparently there are no pronounced differences, which could have been induced by structural distortions of the protein due to the non-occupancy of the Q_A binding site. Thus we are encouraged to assume that the kinetic similarity also extends to longer times. Looking at details, however, we find that at 280 K the 83.6 ps component is larger by 10% in the $F(t)_{QA}$ than in $F(t)_{free}$ (Table 4.2), though according to our assumptions $F(t)_{free}$ should always be smaller than $F(t)_{QA}$. One of the following reasons could be responsible for this finding:

Table 4.3. The difference of the amplitude of Q_A-containing RCs from that of Q_A-free RCs relative to the first amplitude A_1 in the fits presented in Table 4.2. For reference the time constants corresponding to the amplitudes are given too.

T [K]→	85	120	160	200	220	240	280
τ_3 [ps]	158	152	146	144	119	89.8	83.6
τ_4 [ps]	527	605	687	772	669	514	659
τ_5 [ns]	2.55	3.01	3.18	3.75	3.03	2.59	3.32
τ_6 [ns]	16.2	15.0	15.5	15.8	14.2	11.5	11.3
$\left(A_3^{free} - A_3^{Q_A}\right)/A_1$	4.49 %	4.05 %	1.52 %	1.83 %	5.04 %	2.23 %	-0.15 %
$\left(A_4^{free} - A_4^{Q_A}\right)/A_1$	1.74 %	1.25 %	0.70 %	1.20 %	1.87 %	1.21 %	0.119 %
$\left(A_5^{free} - A_5^{Q_A}\right)/A_1$	0.110 %	0.148 %	0.162 %	0.221 %	0.406 %	0.241 %	0.0501 %
$\left(A_6^{free} - A_6^{Q_A}\right)/A_1$	0.0185 %	0.0377 %	0.0483 %	0.0612 %	0.0790 %	0.0462 %	0.0146 %

(i) The unresolved first time component of $F(t)_{free}$ may be slower than in $F(t)_{QA}$ so that the amplitudes of all the other components have to be scaled up relative to the first one in the Q_A-free sample. As pointed out from the preliminary experimental results in Ref. [2], this component indeed may be slower by ~30%. Such a difference could be induced by different prompt fluorescence amplitude a_{prompt} in the case of presence or absence of Q_A in contradiction with the working hypothesis. Another reason could be a presence of a significant delayed fluorescence amplitude $a_{delayed}(t)$ at early times from a minority of RC with faster than the average primary and secondary charge separations. Such an observation[2] although could be induced by a preferential excitation of a Q_A-free sample minority resisting Q_A reconstitution, which is almost unavoidable for fluorescence upconversion experiments since the recombination times differ with ~5 orders of magnitude for the both RCs preparations;

(ii) $F_{prompt}(t)$ may have larger amplitude in the Q_A-containing sample at 83.6 ps, indicating a somewhat larger minority with the corresponding CS kinetics in this sample. This is unlikely because one would rather expect slower kinetics from the Q_A-free protein which is disturbed in comparison with the native Q_A-containing protein;

(iii) At 280 K $a_{delayed}(t)$ may be significantly larger in the Q_A-containing sample than in the Q_A-free one, showing itself as a 83.6 ps component, because of the corresponding decay of $P^+H_A^-$. This would imply that in this time range $P^+H_A^-$ of the Q_A-containing sample is significantly higher in energy, i.e. it does not relax as fast as in the Q_A-depleted sample. Such a difference in the fast protein relaxation of $P^+H_A^-$ at the both samples could originate from a higher degree of structural flexibility in the environment of $P^+H_A^-$ and $P^+B_A^-$ due to the empty Q_A site. This however should also have a pronounced effect on the electronic coupling and finally on the CS kinetics, which has not been observed however. For further elucidation of this issue comparative measurements of $F(t)_{free}$ and $F(t)_{QA}$ at very low temperatures (10 K), would be valuable, since there we expect delayed emission to be frozen out completely[33, 84];

Nevertheless some small structural differences could be possible only above the freezing temperature of the solvent in contradiction with the working hypothesis.

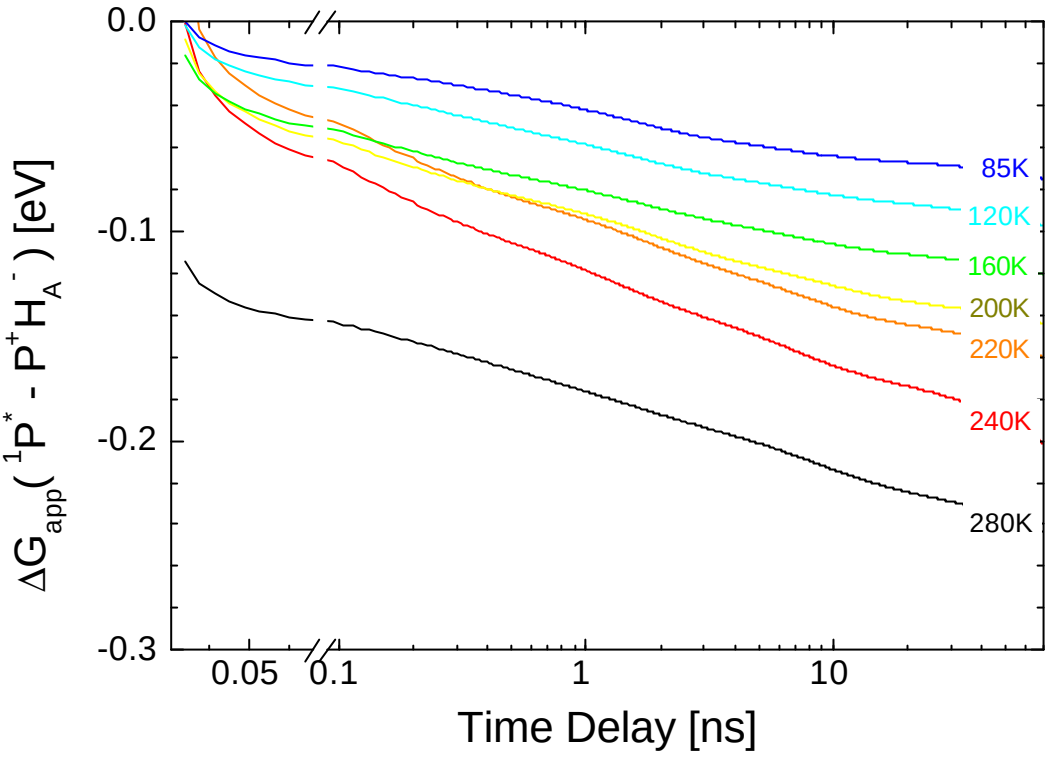

Fig. 4.4. Time and temperature dependence of the apparent free energy difference between $^1P^*$ and $P^+H_A^-$ in R26 *Rb. sphaeroides* RCs obtained from the time-resolved fluorescence data from Fig. 4.2 and Table 4.2 according to eq. (4.2) and (4.14-15).

We have obtained $a_{delayed}(t)$ from eq. (4.15) by inserting the deconvoluted multi-exponential decay data for $F(t)_{free}$ and $F(t)_{QA}$ given in Table 4.2 in order to be free of the distortions of the experimental raw data due to the instrumental response. Apparent free energy $\Delta G_{app}(t)$ then is derived according to eq. (4.2). Because of the limited systematic accuracy of the comparative measurement and since the denominator in eq. (4.15) becomes too small at earlier times $a_{delayed}(t)$ and thus the $\Delta G_{app}(t)$ can be quantified only after a delay of about 100-200 ps depending on the temperature. $\Delta G_{app}(t)$ in Fig. 4.4 should therefore not be taken literally at times shorter than 100-200 ps.

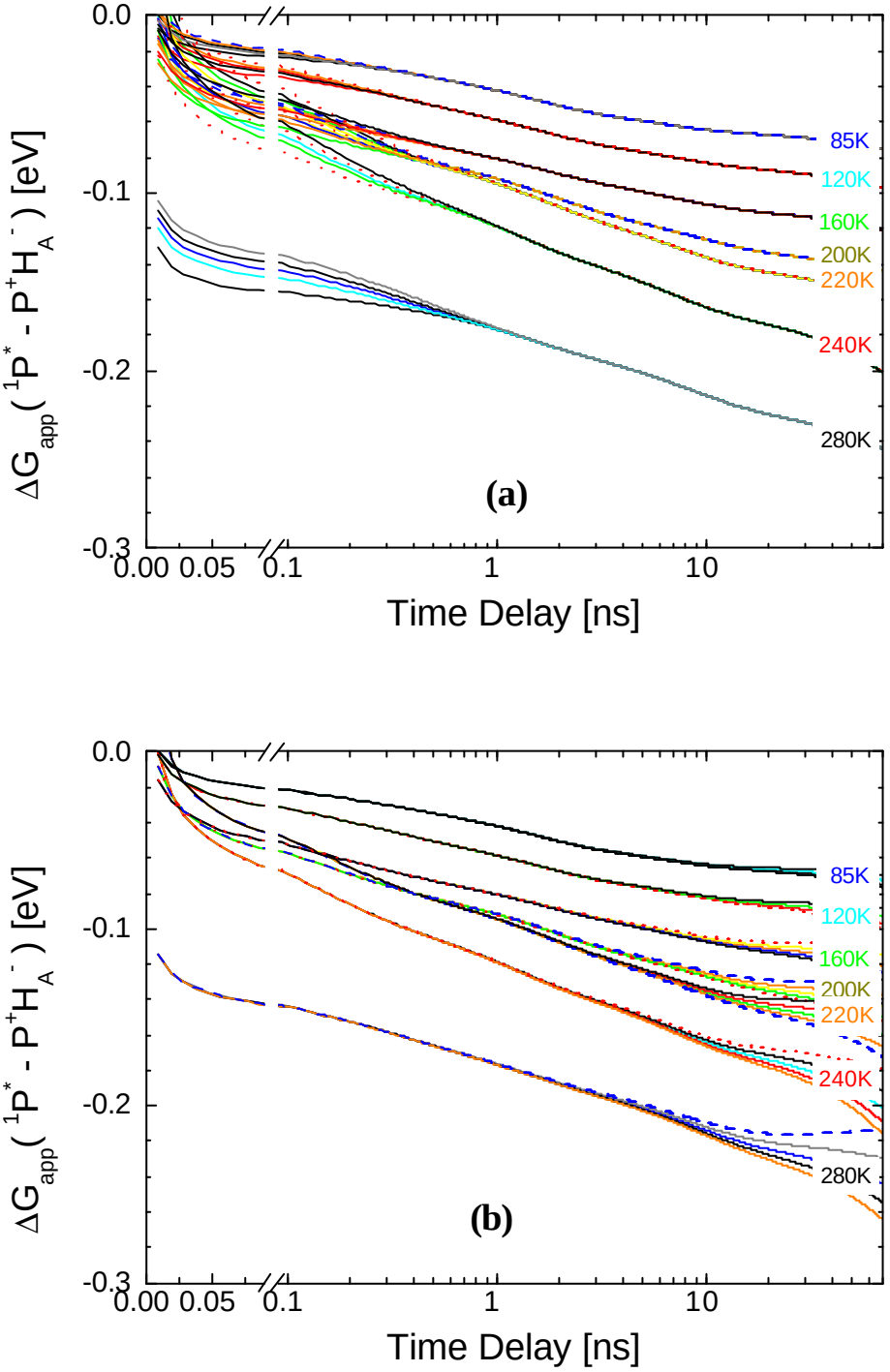

Fig. 4.5. Variation of $\Delta G_{app}(t)$ with τ_{Q_A} and τ_{free}. Solid lines are the literature values while dotted and dashed lines are when varying τ_{Q_A} with +20% and -20%, respectively (a) and τ_{free} with +10% and -10%, respectively (b). Short dotted and short dashed lines are when varying τ_{Q_A} with +50% and -50%, respectively (a) and τ_{free} with +20% and -20%, respectively (b).

τ_{Q_A} has been reported to depend on the wavelength of detection when monitoring the electrochromic shift of the 800 nm band. The $P^+H_A^-$ decay has thus been considered dispersive[54], though for a given wavelength no deviation from monoexponentiality has become evident in this

experiment nor has been reported elsewhere. The signal to noise ratio in this reference was not high enough to distinguish dispersive kinetics. Since this reaction is activationless it should not be particularly sensitive to energetic inhomogeneity. On the other hand we expect the electrochromic shift to be sensitive to the protein surrounding and its response to the ET act. In lack of further information, we describe the decay τ_{QA} of $P^+H_A^-$ in presence of Q_A by a single exponential time constant as in eq. (4.15). The dispersive kinetics of the $P^+H_A^-$ lifetime in Q_A-free RCs was investigated in [86] and τ_{free} was estimated to be essentially monoexponential. The width of its distribution was estimated to be wide less than ±13% of its mean value. Thus the description by a single exponent τ_{free} in eq. (4.15) is justified. In order to judge the sensitivity of $\Delta G_{app}(t)$ to uncertainties of the $P^+H_A^-$ lifetimes we have changed τ_{QA} by ±20% and ±50% and τ_{free} by ±10% and ±20% without obtaining significant deviations of $\Delta G(t)$ in the time window of 200 ps to 15 ns as it is evident from Fig. 4.5. At 200 ps a change of τ_{QA} by ±50% induces deviation of ΔG_{app}(200 ps) of about ±3% at 280 K. The same deviation of ΔG_{app}(15 ns) is observed when varying τ_{free} by ±20%. 280 K is the most sensitive temperature to uncertainties in τ_{QA} and τ_{free}. It is possible to extend the experimentally safe time window for the other temperatures, but for simplicity we will consider it temperature independent in the following investigations.

As already mentioned, delayed emission cannot be quantified at times earlier than 80-100 ps. However, it does not seem likely that it should take up a significant fraction of the total emission at very early times, because the overall emission rises very steeply at early times. Indeed, it has been shown that the decay of the photon echo signal covers the time range of both fast and slow components up to 4 ps[87]. Because optical coherence is destroyed after charge separation, only prompt emission can contribute to the photon echo signal. This finding demonstrates that prompt emission dominates at least in the 10 ps fluorescence component.

In Fig. 4.4 one can observe a relaxation with time of the apparent free energy difference between the excited special pair $^1P^*$ and the bacteriopheophytin radical pair $P^+H_A^-$. This is not the real energy relaxation of $P^+H_A^-$ radical pair but by definition from eq. (4.7) it is the effective one assuming $P^+H_A^-$ as a single state, i.e. the apparent free energy. If we account for the inhomogeneous broadening of radical pair state we have to correct this apparent energy as discussed in section 4.3. The correction we have developed there is valid under the following assumptions:

i) The distribution of $P^+H_A^-$ radical pair free energy is Gaussian

ii) The half width σ of this distribution is time independent. Two different approaches will be used – fixing σ as a temperature independent constant or assuming temperature dependence of σ according to molecular dynamics simulations.

In Appendix A an approximated formula is developed which allows treating the correction without the second assumption (see eq. (4.8)).

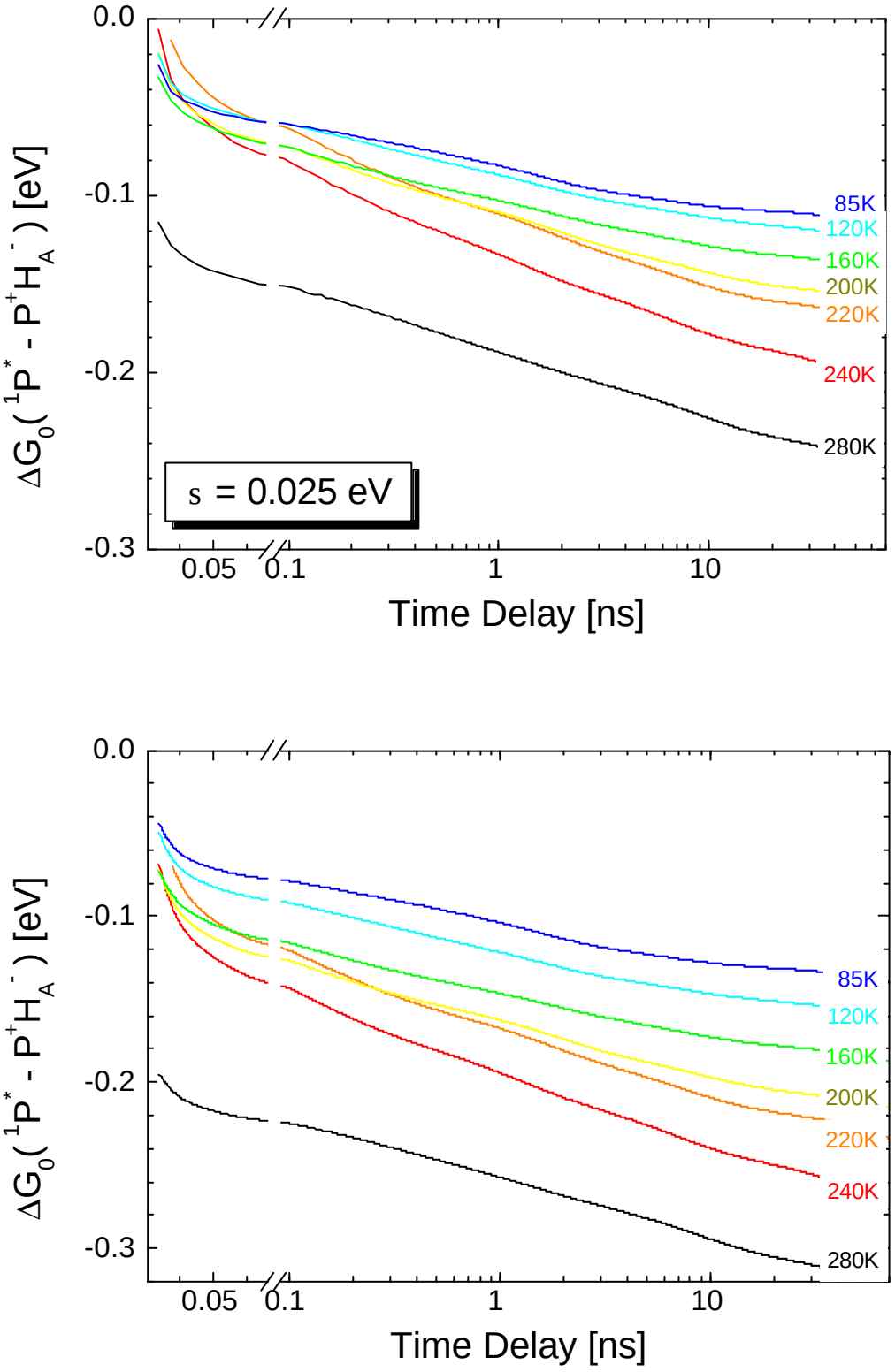

Fig. 4.6. (a) Time dependence of the relaxation of the center of $P^+H_A^-$ Gaussian distribution $\Delta G_0(t)$ with half width σ = 0.025 eV at temperatures of 85, 120, 160, 200, 220, 240 and 280 K determined according to eq. (4.8). The absolute values of $\Delta G_0(t)$ for 0.5 < t < 10 ns should be taken only literally; (b) Time dependence of $\Delta G_0(t)$ with σ according to eq. (4.18) when r = 0.4.

The Gaussian distribution is commonly used for describing inhomogeneous broadening due to protein conformations as for example in myoglobin CO recombination. The adequacy of the Gaussian distribution to describe protein inhomogeneity speaks for its random character since the Chebishev theorem states that if a process is controlled by more than 4 random factors, its measurable characteristics are always Gaussian distributed.

Investigating the time evolution of the half width of the RP energy distribution σ requires additional experimental information to our delayed emission data. Thus as a first approximation in our investigation we propose a time-independent σ.

The relaxation of the center of the radical pair energy distribution $\Delta G_0(t)$ was obtained according to 4.8 for several σ ranging from 0.010 eV to 0.050 eV with step of 0.005 eV. We have chosen the maximum σ where the $\Delta G_0(t)$ are still ordered hierarchically with temperature, i.e. the absolute values of the $\Delta G_0(t,T)$ are monotonically decreasing with decrease of temperature at each time in the experimentally safe time window (between 200 ps and 15 ns). This σ was found to be 0.025 ± 0.005 eV and the corresponding $\Delta G_0(t)$ is presented in Fig. 4.6a at different temperatures. This choice of σ could overemphasize the temperature dependence of the initial relaxation before 200 ps but on the other hand the values of ΔG_0 after 1 ns are far above the values determined by other methods[62, 66, 67]. One reason for this is that the assumption that σ is not temperature dependent. The temperature dependence of σ could be obtained in general from the width of the distribution of the primary charge separation rates[28, 88]. Unfortunately in the case of strongly dispersive multistep kinetics where two different unknown energy distributions are involved as in our case this is not a straightforward approach. There are no experimental results and only very few theoretical contributions through the literature that are treating this problem[65, 66]. The reason for this is that it is difficult experimentally to access such information for the $P^+H_A^-$ radical pair.

It is interesting to show how the overall results for the $P^+H_A^-$ relaxation from Fig. 4.6a could be modified at temperature dependent σ. For this purpose we have taken the temperature dependence deduced from molecular dynamics simulations in Nonella et al.[65] normalized by a variable temperature independent dimensionless factor r such that the mean value ΔG_0 to be around 0.25 eV at 1 ns and 280 K as experimentally determined in Volk et al.[62]:

$$\sigma(T) = r\,\frac{0.101 + 0.0009525.T}{2\sqrt{ln(4)}} \qquad (4.18)$$

where $\sigma(T)$ is in eV. We have found that this condition is fulfilled for r = 0.4. The obtained time dependences of ΔG_0 at the 7 investigated temperatures using eq. (4.18) are shown in Fig. 4.6b.

It is evident that there is a large change in the ultrafast dielectric response above and below the freezing temperature of the solvent. The ultrafast dielectric response below the freezing temperature of the solvent is no longer temperature independent. But this behavior strongly depends on the explicit function of σ from T. Nevertheless a shift of 0.10 eV for 240 K to 0.15 eV for 85 K in comparison to the initial relaxation at 280 K is observed.

As already mentioned the time course of $\Delta G_0(t)$ for $t < 200$ ps should not be taken literally. In fact we expect the initial relaxation to be of dielectric nature and well below our time resolution. However, the amplitude of this initial relaxation can be derived from our experiment and it reveals very interesting results. It is evident from Fig. 4.6 that this initial relaxation changes its amplitude upon freezing from around -0.13 eV to about -0.05 eV. This observation shows that the dielectric response in the close environment around the P and H_A chromophores is strongly influenced by the freezing of the solvent, which is certainly too far away to directly interact with the $P^+H_A^-$ radical pair. Apparently fast protein modes are frozen together with the phase transition of the solvent at 260 K. In other proteins like myoglobin a transition temperature associated with freezing of relaxational degrees of freedom occur at about 200 K and seem to be independent from the solvent. In fact at such high temperature no such distinct change has been observed at all. However these investigations pertain to slower time scales (ns to ms) and to solvents including glass forming agents like glycerol and sugars (trehalose). Due to the insensitivity of our experiment to light scattering we were able to measure in absence of a cryoprotector in the solvent. On one hand, glycerol e.g. is known to dehydrate and destabilize protein structure. In reaction centers at concentrations higher than 60% a blue shift of the P_{860}-band is observed and charge separation is impaired[89]. On the other hand the lack of a glass forming agent leads to a polycrystalline structure of the solvent, which might form a less “soft” cage around the protein imposing stronger restrictions to internal protein motions than in the glass. There is no evidence for large scale deformation of the protein in the frozen state even in absence of a cryoprotector, since no apparent change of the fast charge separation component was observed[2] nor does the prompt fluorescence of the slow minority shows any evidence according to this work (compare Fig. 4.3).

In the following we will discuss three distinct temperature regions with different relaxation kinetics in Fig. 4.6. At temperatures below 160 K we have slow relaxation with an almost temperature independent time constant (low temperature range). At temperatures between 200 K and freezing point of the solvent (260 K) the relaxation speeds up with increase of temperature (middle temperature range). In the high temperature range above the freezing point of the solvent the relaxation is slightly slower than in the middle temperature region. This may be due to the fact that after the large initial relaxation only few relaxation barriers in the conformational landscape are left to be overcome. Thus we have observed two transition temperatures in the protein

relaxation in RC in aqueous solution in 200 ps – 15 ns time range. The freezing temperature of the solvent contributes to the freezing part of the ultrafast relaxation and we will call the dielectric transition point. The second transition temperature observed between 200 and 160 K coincides with that observed in other proteins and is a well accepted intrinsic property of proteins which was shown by variety of methods pertaining to slower timescales from ns to minutes[28, 38, 90-93]. Using aqueous solvent and high time resolution we have separated the classical protein transition at 200 K from the solvent induced dielectric transition. So far this transition has been obscured because: (i) in presence of a glass forming agent both transition temperatures fortuitously coincide and (ii) experiments pertaining to the mobility of the CO ligand or the heme-iron in myoglobin may not be sensitive to the ultrafast fluctuations associated with the dielectric response. In the next section we will analyze our data in terms of the existing theories and empirical approaches of protein relaxation.

4.7. Discussion of the $P^+H_A^-$ relaxation in terms of the existing theories and empirical approaches

A common feature of proteins is the large number of conformational substates, which often are important for their biological function[94]. Such states can be described as a point in a multidimensional rough potential (see Fig. 4.7) called conformational landscape. Due to the complex nature and high dimensionality of such a landscape thermally induced transitions between the different substates have a highly statistical character and usually are described by a diffusive motion[95]. This motion in phase space of course is closely related to changes in protein structure. At thermal equilibrium, i.e. in absence of a driving force, such motions within the thermally accessible neighborhood of the potential minimum are called **fluctuations**. In many cases these fluctuations can gate the accessibility of reaction sites inside the molecule[38, 90, 92-94, 96-98] and will therefore be of crucial importance for biological function. If the system is quickly transferred into a starting state which is not in thermal equilibrium by a triggering process like temperature jump, pressure jump or field jump, it will move downward in the complex energy landscape along one of a large multitude of trajectories heading to a potential minimum. Since ΔG is dissipated this process is irreversible and thus called relaxation. Relaxation can be monitored on various observables $O(t)$ as a function of time. These observables will directly or indirectly depend on the free energy ΔG and will therefore reflect the energetic relaxation with time. Such observables may be spectral lines shifting during the relaxation process, transport phenomena and enzymatic kinetics or even electron transfer kinetics changing during relaxation. In contrast to these observables here we are directly monitoring the free energy.

The transitions between the conformational substates of biological macromolecules occurring during relaxation are determined by the local surrounding in the conformational landscape, which form statistically varying barriers (see Fig. 4.7). Thus they may proceed with rates differing by many orders of magnitude[94] and leads to a complex, inhomogeneous dynamics of the relevant observables.

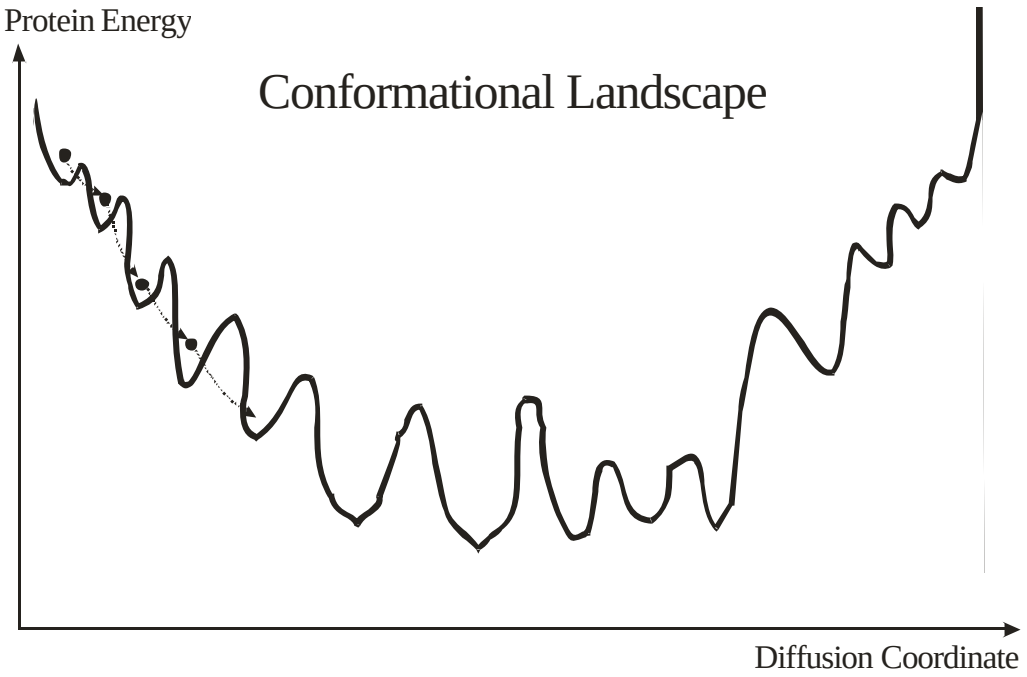

Fig. 4.7. Diffusion through a rough potential

The conformational response of the protein to a triggering perturbation observed on one of the different observables $O(t)$ is commonly characterized by the normalized relaxation function[90, 97]:

$$\Phi(t) = \frac{O(t) - O(\infty)}{O(0) - O(\infty)} \tag{4.19}$$

where $O(0)$ is the initial value of the observable if only conformational response is assumed. Often other responses are accumulated in the observable in early times depending on the type of initial disturbances. In pressure (P)-jump experiments elastic response takes place while in ET initiated protein relaxation as in our case an ultrafast dielectric response might contribute together with the conformational response to the observable $\Delta G_0(t)$ before 50 ps (see previous section). These two types of relaxation might have completely different origin although they are reflected by one observable function.

Our observable is the mean value $\Delta G_0(t)$ of the Gaussian distribution of the $P^+H_A^-$ radical pair energies. The relaxation function in our case is thus given by:

$$\Phi(t) = \frac{\Delta G_0(t) - \Delta G_0(\infty)}{\Delta G_0(0) - \Delta G_0(\infty)} \tag{4.20}$$

The Kohlrausch-Williams-Watt (KWW) law: Due to the statistical distribution of energetic barriers E_a along the relaxation pathways in a protein the relaxation function is not exponential with time[90]. According to the equivalence of ensemble and time averaging it can be described by a distribution of exponentials with time constants corresponding to the barrier distribution $\rho(E_a)$:

$$\Phi(t) = \int r(E_a) \exp\left[-\left(\frac{t}{t(E_a)}\right)\right] dE_a \tag{4.21}$$

Usually $\rho(E_a)$ is assumed to be a Gaussian distribution of barriers. $\tau(E_a)$ is most often assumed to behave according to a simple Arrhenius law:

$$\tau = \tau_0 . exp\left(\frac{E_a}{k_B T}\right) \tag{4.22}$$

In a double log/log plot such a relaxation function is characterized over quite a large range by a straight line with some bending as shown in Fig. 4.8.
$\tau(E_a)$ could also use other dependence as will be discussed later.

Relaxation functions have often been parameterized by the empirical Kohlrausch - Williams - Watt (KWW) law[99, 100], usually dubbed stretched exponential function[90, 101]:

$$\Phi(t) = exp\left[-\left(\frac{t}{\tau(T)}\right)^{\beta(T)}\right] \tag{4.23}$$

where $0<\beta<1$. This function is characterized by a long tail extending over many orders of magnitude in time, which becomes more pronounced the smaller the stretching parameter β is. In the double log/log plot it gives a straight line and can well represent the function 4.23 over a large time range. Unfortunately there exists no simple relation between the τ and β parameter of 4.23 and the location and width of the Gaussian barrier distribution and the preexponential factor τ_0. Since our data cover only about 2 orders of magnitude in time it is difficult to reliably extract τ and β values of eq. (4.23). The relaxation time $\tau(T)$ is the characteristic diffusion time and depends on the characteristic size of the energy barriers E_a along the relaxation path in the conformational landscape[102] and thus should exhibit a thermally activated behavior. The stretching parameter β characterizes the distribution of relaxation times[103] and is a good measure of how dispersive the relaxation is[101, 104]. As it approaches 1 the relaxation becomes exponential,

representing a non dispersive Debye type relaxation[105]. In a recent interpretation of the KWW-law the stretching factor β represents the dimensionality of the fractional Fick's second law equation known as diffusion equation[106, 107]. This equation was found to describe diffusion processes in complex systems where continuous-time random walks do **not have finite mean values of the waiting time** for transitions between the different substates[108, 109]. In these cases β is determining the character of the diffusion process as superdiffusive (β>1) and subdiffusive (0< β<1)[110].

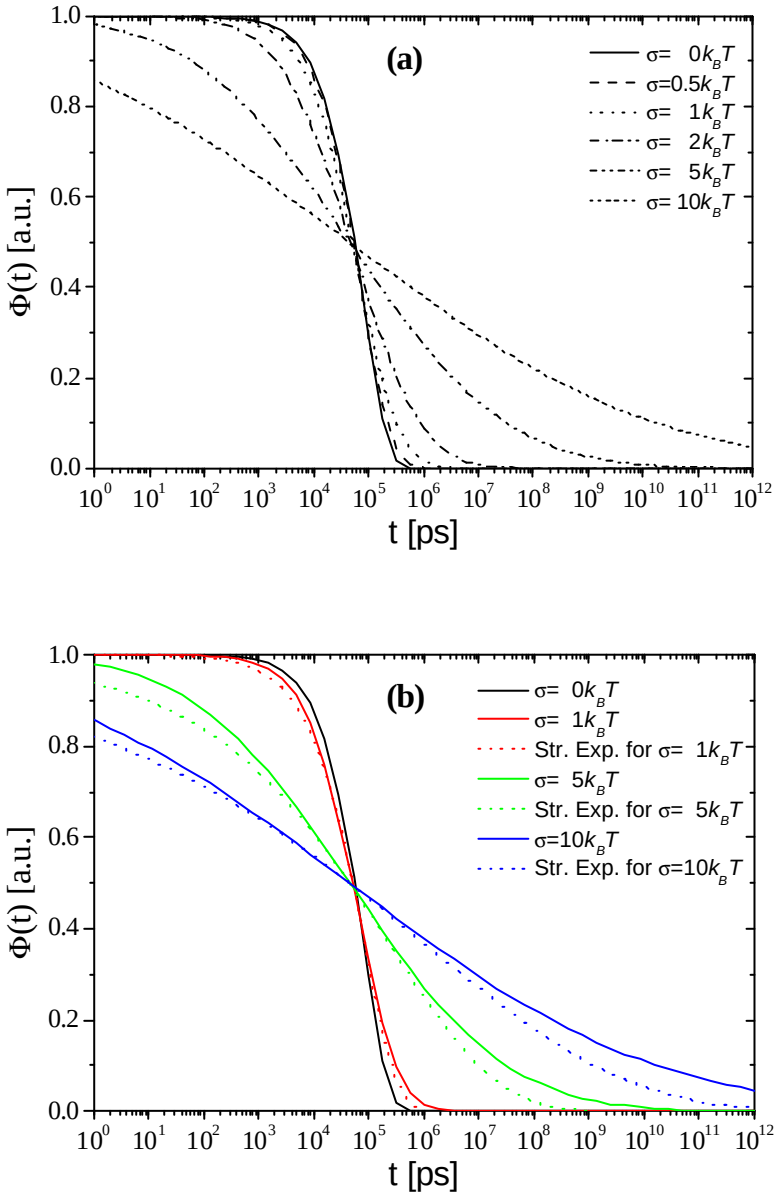

Fig. 4.8. (a) Simple Arrhenius relaxation as in eq. (4.22) (solid line) and dispersive relaxation assuming Gaussian distribution of the Arrhenius activation energy as in eq. (4.21) with σ = 0.5, 1, 2, 5 and 10 times k_BT (nonsolid lines). (b) Comparison between some of the dispersive relaxations from (a) (soled lines) with their stretched exponential fits (dotted lines).

Similarities in formal description of the protein relaxation with other relaxation processes are pointed out elsewhere[97]. The observables and the physical meaning of β and τ are different in these cases. For example the dielectric relaxation in glasses[111] and in supercooled liquids[112] as well as the conductivity in organic polymers[113] obey similar relaxation behaviors as in proteins.

Temperature laws: Numerous *empirical* approaches developed in other areas of science were applied to the description of such processes and therefore were applied also to protein relaxation, in particular the temperature dependence of τ.

(i) **The classical Arrhenius type of temperature dependence** characterizing elementary reactions across a well defined homogeneous barrier is expected in proteins only if bottleneck pathways with a specific high lying doorway state are rate determining. In general it gives an acceptable description of the temperature dependence of τ only within small temperature intervals[28, 90, 102].

The Arrhenius dependence is typical for low-viscosity materials as liquids and rubber-like materials, where diffusion is characterized by a single barrier.

(ii) **The Ferry type of temperature dependence**[114] is typically used to describe the conductivity of organic polymers[113], or the characteristic rearrangement times of disordered high-viscosity materials as glasses and polymers, where the barriers for transitions become higher and the ability of rearrangement is greatly reduced.

$$\tau = \tau_0 . exp\left[\left(\frac{E_a}{k_B T}\right)^2\right] \qquad (4.24)$$

It is successfully used to describe protein relaxation over large temperature intervals[28, 38, 90, 97, 98, 115, 116]. Since it is defined only by two independent parameters τ_0 and E_a it is more convenient than the stepwise definition of Arrhenius barriers in many different temperature intervals. Often it reliably determines the temperature dependence of the relaxation function within limited timescales. A Ferry type temperature dependence is predicted in the irreversible random transition theory (IRT) where the effective diffusion coefficient becomes temperature dependent below a critical temperature T_{cr}[102]. In this theory a hierarchy of irreversible conformational transitions are assumed and a proportionality between τ and β parameters is deduced:

$$\tau \sim exp\left[\frac{4}{\beta}\left(\frac{1}{\beta} - 1\right)\right] \qquad (4.25)$$

(iii) **The Vogel-Tammann-Fulcher (VTF) type of temperature dependence**[90, 112] uses an additional parameter, the characteristic temperature T_0, which describes the typical width of the

barrier height distribution. It can be derived as the mean lifetime time of an inhomogeneous ensemble with a Gaussian distribution of barriers[85]:

$$\tau = \tau_0 . exp\left[\frac{E_a}{k_B(T - T_0)}\right] \qquad (4.26)$$

Eqs. (4.22, 4.24) were successfully used to determine the dielectric relaxation in glasses over times of more than 10 orders of magnitude[111, 117].

(iv) At very **low** temperatures, typically <10 K, a **power law** is commonly used to describe $\tau(T)$ derived from the line width of hole burning experiments[32, 37]:

$$\tau = A_\tau T^{-p} \qquad (4.27)$$

The temperature dependence of $P^+H_A^-$ relaxation: We have tested all these temperature laws of the characteristic relaxation time τ according to eqs. (4.22, 4.24, 4.26, 4.27) by fitting a stretched exponential function according to eqs. (4.20) and (4.21) to the time dependence of $\Delta G_0(t)$ in Fig. 4.6. If the complete temperature range 85-240 K was fitted simultaneously with a single set of parameters it was not possible to obtain physically meaningful results for any of the proposed types of temperature dependences. Good fits could be obtained, however, when different parameter sets were allowed for in two distinct temperature ranges. The results are presented in Table 4.4.

The difference in the case of temperature dependent σ is that the absolute values of $\Delta G_0(0)$ and $\Delta G_0(\infty)$ from eq. (4.20) are decreased roughly with $[\sigma(T)^2\text{-}0.025^2]/2k_BT$ for $\sigma(T) > 0.030$ eV i.e. for all of the temperatures considered in our investigation. Such a result is expected considering that for $\Delta G_0 >> \sigma$ eq. (B5) from Appendix B could be applied for the correction of the apparent free energy ΔG_{app}. Consequently the values of β and τ are within the fit uncertainty of the fits presented in Table 4.4.

For 280 K it was not possible to perform a global fit and a simple stretched exponential fit gave $\beta = 0.18$ and $\tau = 0.99$ ns. As for the lower temperatures, the $\Delta G_0(0)$ and $\Delta G_0(\infty)$ values differ for the case of temperature independent σ (0.025 eV) and dependent σ (0.052 eV). In the first case $\Delta G_0(0) = -0.12$ eV and $\Delta G_0(\infty) = -0.36$ eV. In the latter case $\Delta G_0(0) = -0.14$ eV and $\Delta G_0(\infty) = -0.38$ eV. There is a clear downshift of $[0.052^2\text{-}0.025^2]/2k_B280 \sim 0.02$ eV as expected. This result confirms once again the difficulty of extracting the exact values of the initial fast dielectric relaxation amplitude by our method. Nevertheless the big jump of this amplitude upon solvent freezing is evident independently of the assumption for σ.

Table 4.4. Results from fitting of the data in Fig. 4.6 with stretched exponential relaxation function according to eqs. (4.20-4.21) with different temperature dependences of the characteristic relaxation time τ according to eqs. (4.22, 4.24, 4.26, 4.27).

	Low Temperatures			Middle Temperatures		
T [K]	85	120	160	200	220	240
$\tau(T)$ type	Arrhenius (eq. (4.22))					
$\chi^{(2)}$	1.3×10^{-7}			9.1×10^{-8}		
τ_0 [ns]	0.32			1.4		
E_a [eV]	4.4×10^{-3}			2.0×10^{-5}		
β [a.u.]	0.38	0.30	0.23	0.34	0.28	0.24
$\Delta G_0(0)$ [eV]	-0.018	-0.006	0	-0.037	-0.005	-0.004
$\Delta G_0(\infty)$ [eV]	-0.11	-0.12	-0.15	-0.16	-0.18	-0.22
$\tau(T)$ type	Ferry (eq. (4.24))					
$\chi^{(2)}$	3.7×10^{-8}			1.1×10^{-7}		
τ_0 [ns]	0.29			1.1		
E_a [eV]	8.0×10^{-3}			4.4×10^{-3}		
β [a.u.]	0.45	0.30	0.24	0.33	0.27	0.25
$\Delta G_0(0)$ [eV]	-0.038	-0.09	0	-0.033	0	0
$\Delta G_0(\infty)$ [eV]	-0.11	-0.12	-0.15	-0.16	-0.18	-0.22
$\tau(T)$ type	VTF (eq. (4.26))					
$\chi^{(2)}$	4.2×10^{-8}			No convergence		
τ_0 [ns]	0.21					
E_a [eV]	8.0×10^{-3}					
T_0 [K]	25.2					
β [a.u.]	0.45	0.31	0.24			
$\Delta G_0(0)$ [eV]	-0.038	-0.011	0			
$\Delta G_0(\infty)$ [eV]	-0.11	-0.12	-0.15			
$\tau(T)$ type	Power Law (eq. (4.27))					
$\chi^{(2)}$	4.53×10^{-8}			No convergence		
A_τ [ns/K]	620					
p [a.u.]	2.76					
β [a.u.]	0.46	0.27	0.19			
$\Delta G_0(0)$ [eV]	-0.039	0	0			
$\Delta G_0(\infty)$ [eV]	-0.11	-0.12	-0.15			

In the small temperature interval between 200 K and 240 K there is essentially no temperature dependence. The Arrhenius law gives an activation barrier of only 2.0×10^{-5} eV. In the temperature range from 160 K down to 85 K the Ferry and VFT-law give the best fits with $\chi^{(2)}$ of 3.7×10^{-8} and 4.2×10^{-8}, respectively.

We tried to simultaneously fit τ and β according to the ITR- theory (eq. (4.25)). However, we were not able to find any pair of different temperatures at which we could fit the data with such a constraint.

The temperature dependences of the stretched exponential parameter β from Table 4.4 are presented in Fig. 4.10. A common feature of all the fits is the increase of β with decreasing temperature. Thus we find relaxation to become less dispersive with decreasing temperature. Just the opposite temperature dependence of β is predicted for dispersive kinetics originating from a distribution of activation barriers (e.g. IRT theory). Such opposite temperature dependence is observed in numerous contributions dealing with protein relaxation in various systems and investigated by various methods in slower time scales[28, 38, 90-93, 95, 98, 102, 113].

It should be emphasized, that a reliable derivation of the stretching parameter β requires large time windows, which are necessary for experimentally capturing the initial and final amplitudes of the observable ($\Delta G(0)$ and $\Delta G(\infty)$). These cornerstone values are essential for correctly defining the relaxation function (4.21) and extracting β. We consider the preceding ultrafast dielectric relaxation of $P^+H_A^-$ as an independent process: Therefore it is dangerous to describe the relaxation function of this process by the same parameter set. Because according to Fig. 4.6 this fast dielectric relaxation apparently has strongly temperature dependent amplitudes (at least around the melting point of the solvent) the slower relaxation processes related to protein motion investigated here will succeed at different starting points $\Delta G(0)$. Due to the intrinsically limited time window of this method we have no good way of extrapolating $\Delta G(0)$.

The extrapolation of $\Delta G(\infty)$) is likewise problematic. We have no evidence that the relaxation process tapers off at the end of our time window. In fact, usually protein relaxation data refer to time windows which begin where our window ends. Such data show considerable relaxation on the µs and ms timescale. In particular, it has been shown, that relaxation affects the recombination of $P^+Q_A^-$ on the 30 ms timescale[28]. At low temperatures $P^+Q_A^-$ recombination happens to occur in the activationless limit. Above 200 K relaxation is faster and brings the $P^+Q_A^-$ state further down to an energetically less favorable state in the activated regime before recombination can take place at a lower rate. At low temperatures relaxation is incomplete on this time scale and may be extended to timescales way beyond experimental accessibility.

In thermal release experiments the relaxation after formation of $P^+Q_A^-$ can be directly monitored with µs time resolution[118]. At room temperature the main part of the relaxation corresponding to an energy release of 0.5 eV occurs faster than this time scale. Additional 0.1 eV are released with

a time constant of 3 ms (see Fig. 4.9). We expect that relaxation dynamics in the states $P^+H_A^-$ and $P^+Q_A^-$ do not differ substantially. Accordingly at room temperature relaxation is not complete on the ns-timescales of our experiment. This indeed seems to be reflected in the high temperature curves in Fig. 4.6. At low temperature part of the relaxation may in principle be arrested, i.e. to become much slower than the repetition rate of the experiment. According to Fig. 4.6 $\Delta G(t)$ seems to be leveling off at around 10 ns and become constant with time. It is not clear whether this observation is really significant.

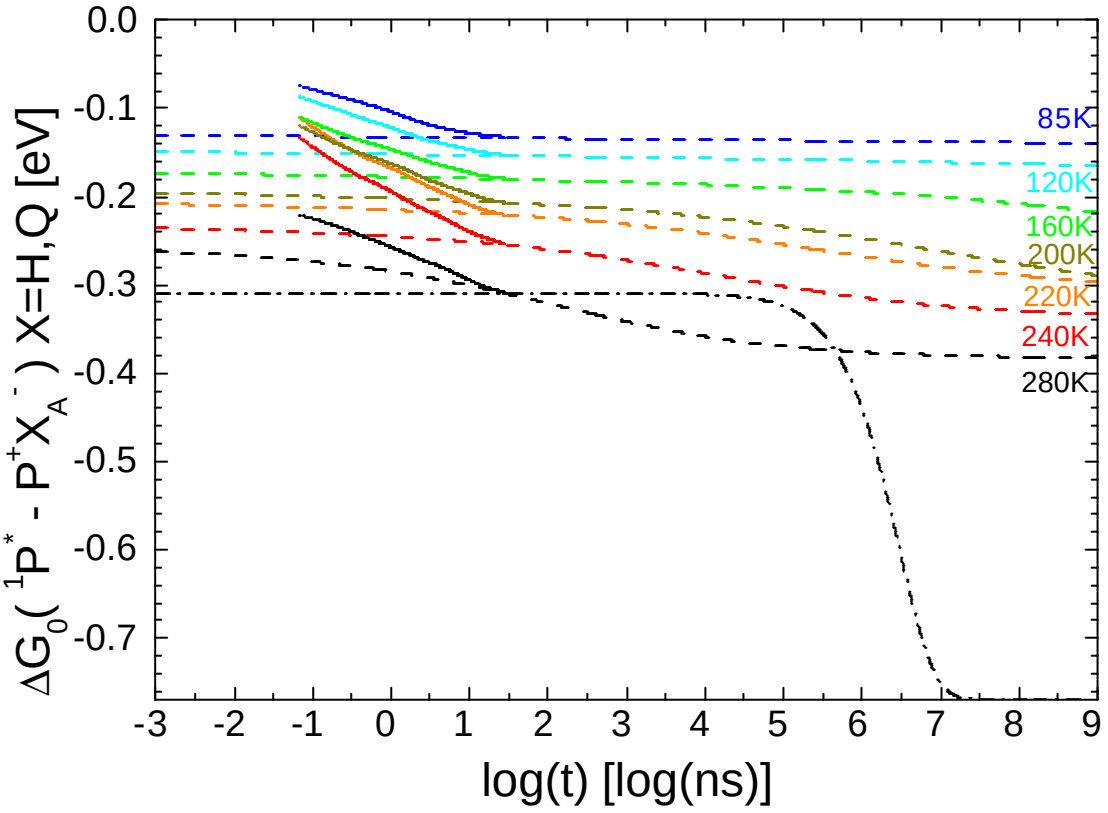

Fig. 4.9. Comparisson between our results for the protein relaxation of $P^+H_A^-$ radical pair and of the only experimental results for RCs available in the literature so far for $P^+Q_A^-$ radical pair. $\Delta G_0(t)$ with temperature dependent σ (see Fig. 4.6a) for the $P^+H_A^-$ radical pair in the 0.1-10 ns time window (solid lines) and in the 0.66-28 ns (dotted lines). $\Delta G_0(t)$ for the $P^+Q_A^-$ radical pair according to McMahon et al.[28] (dashed lines) and Leyser[118] (dashed-dotted lines). Since the literature data has been deduced only for slow time scales (ms-ks) we made the crossing point with our data at the end of our time window at 28 ns and preserved the relaxation amplitudes $\Delta G(\tau_{time\ resolution})$-$\Delta G(\infty)$ as reported[28, 118].

One can try to extrapolate the data of McMahon et al.[28] to the time scale of our experiment. According to these data, the relaxation process of $P^+H_A^-$ can be characterized by 4 different tiers of conformational states with following characteristics:

Tier	E_A	A_A	σ_A	Rel. Amplitude
CS0	1.14 eV	10^{25} s^{-1}	0.25 eV	21%
CS1	0.8e V	10^{21} s^{-1}	0.1 eV	28%
CS2	0.51 eV	10^{15} s^{-1}	0.1 eV	38%
CS3	0.17 eV	10^{13} s^{-1}	0.135 eV	13%

E_A: Arrhenius type average relaxation barrier, A_A: exponential prefactors, σ_A: half width of Gaussian distribution of relaxation barriers. For comparison with our results, we have simulated the relaxation of the various tiers at different temperatures in Fig. 4.9. The center of the lowest tier relaxes on the timescale of 1.2 ms at 80 K. However it only contributes 13% of the total amplitude. The next higher tier is essentially frozen since it has a central time constant of 10000 s. The complete relaxation functions of all tiers are also shown in Fig. 4.9 (equivalent to Fig. 8 in McMahon et al.[28]). At 85 K one would still expect considerable relaxation of $P^+Q_A^-$ proceeding at µs to ks time scale. From these simulations we conclude:

i) relaxation is not complete in our time window at any temperature. Thus we do not think that the flat parts of the relaxation curves in Fig. 4.7 should be taken as an indication for a complete ceasing relaxation. $\Phi(\infty)$ therefore cannot be derived from our experiment.

ii) It is dangerous to extrapolate relaxation functions from one time window to another according to Arrhenius or Ferry law. None of the simulations approximates the time dependent relaxation functions derived in our experiments. Much more they fail to reproduce the unusual temperature dependence obtained in our experiments.

Finally small uncertainties in $\Delta G_0(t)$ determination in the edges of the time window induce considerable variations of the stretched exponential parameter β in the order of ±0.05, even though $\Delta G_0(t)$ is affected only by a few % as shown in Fig. 4.5.

The activation energy E_a from eqs. (4.22, 4.24) can be interpreted as the characteristic barrier height of the conformational landscape[38]. Surprisingly small activation energies were deduced from the fits presented in Table 4.4. Particularly in the middle temperature essentially barrierless protein relaxation was observed. In the low temperature range an activation energy $E_a = 8.10^{-3}$ eV was in the order of k_BT. Such small effective barrier heights were not reported in the literature for the slower timescales. Typical effective barrier heights of ~0.1 eV (~10 kJ/mol) are extracted for myoglobin[97] and R26 *Rb. Sphaeroides* RCs[28] at ms to ks time scales.

The β values given in Table. 4.4 and Fig. 4.10 show opposite temperature dependence, i.e. β increases with increasing T, or in other words, the decay seems to become less dispersive at low T. In the picture of diffusion in a rough potential one would expect the contrary, i.e. an increase of

dispersion at low T. As already discussed, the derivation of β values from our data is problematic, due to the limited time window. It is not likely, however, that uncertainties in the radical pair lifetimes of the Q_A-depleted and Q_A-containing RC preparations are responsible for these results. As shown in Fig. 4.3 we have tested changes of these lifetimes and their influence on the stretched exponential parameter β, and found that this was not big enough to account for the observed temperature behavior in Fig. 4.10. It is evident, however, that at low temperatures the relaxation is less dispersive than at high temperatures.

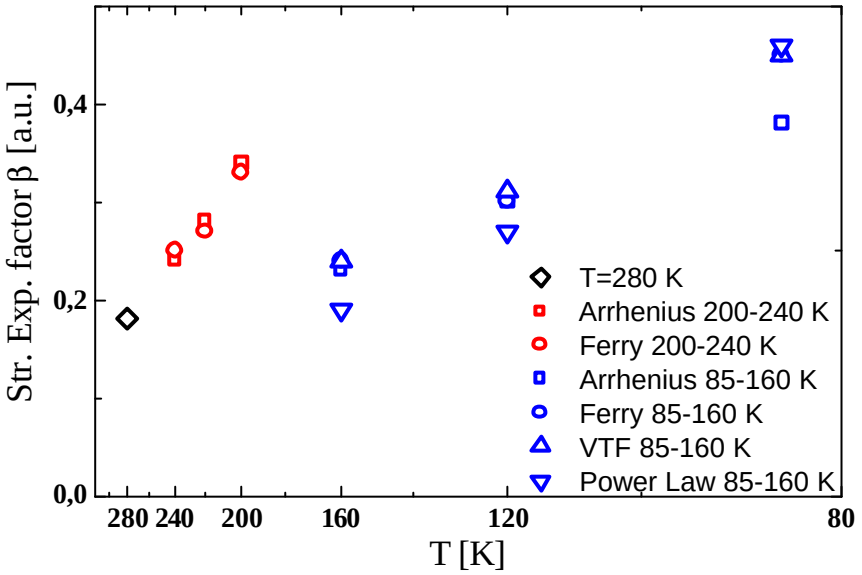

Fig. 4.10. Temperature dependences of the stretched exponential parameter β for the fit results presented in Table 4.4.

We therefore conclude that within the intermediate and low temperature range changes of β cannot be derived with sufficient accuracy to give information about the relaxation mechanisms. However, the relaxation processes observed in our experiments on the timescale of 200 ps-15 ns do not have the fingerprint of diffusive transitions between conformational substates in the energy landscape resembling a rough harmonic potential. This is consistent with the surprisingly small effective energy barriers determined by the stretched exponential fits in Table 4.4.

It is widely accepted that the protein relaxation takes place through very rough potential and changes its behavior at a dynamic transition temperature between 200 and 160 K. Above this temperature the protein is allowed to diffuse among a distribution of barriers in the conformational landscape with effective barrier height which is considerably smaller than the one below this temperature. The diffusion at low temperatures is strongly perturbed due to trapping of the protein in considerably deeper potential minimums than k_BT and consequently the relaxation becomes more dispersive which is just the opposite in our case.

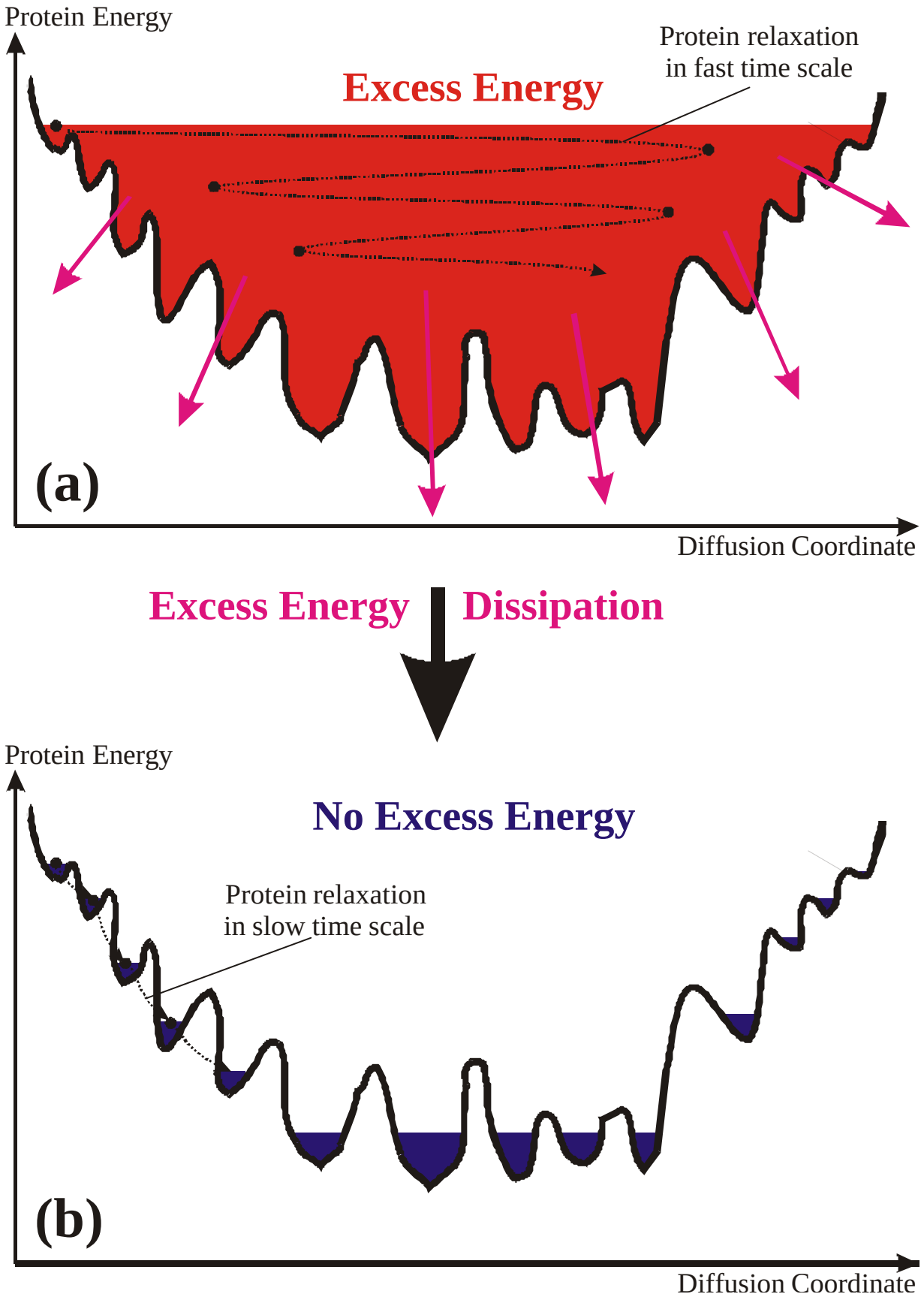

Fig. 4.11. (a) Suggestion for a model for protein relaxation via dissipating of excess excitation energy to the bath in fast (ps-ns) time range. (b) Model for protein relaxation through rough potential in slow (μs-ks) time range supported by numerous contributions in the literature.

Such behavior was determined with different experimental techniques and methods in slower timescales than in our experiment. As mentioned in the previous section there are preliminary results on conformational relaxation of small peptides investigated in similar timescale as in our case[119, 120]. The initial disturbance is a photoinduced trans-cis isomerisation of an azo-benzene dye which is attached in its opposite ends to a peptide chain. Upon this isomerisation the peptide experience strong conformational perturbation which relaxes in the ps to ns timescale. An ultrafast solvation takes place in the picosecond times and then structural relaxation proceeds up to 1 ns. Surprisingly this structural relaxation for such a small molecule, consistent of only 8 amino acids and a small azo-benzene dye molecule, doesn't stop but takes place even further up to ms.

One interpretation consistent with these results and the experiments presented in this chapter will be if we have an excess energy in our system higher than k_BT in this time scale (see Fig. 4.11). In this case the effective barrier height which is in the path of the protein evolution in the conformational landscape will not be the determining factor for the protein relaxation and will become such as soon as this excess energy dissipates. But still the protein relaxation will experience some influence from the landscape and will change its behavior upon approaching the dynamic transition temperature around 160-200 K as it is evident from Fig. 4.6 and Table 4.4. As the temperature goes down the excess energy taken from the protein is faster dissipated and the relaxation is becoming more dispersive. Lowering further the temperature we would expect to dissipate the excess energy faster. At certain temperature the diffusive type of transitions between the conformational states through rough potential will become the protein relaxation rate determining process and then the reverse temperature behavior of β will be observed. Unfortunately 85 K is close to the temperature where $\Delta G_0(t)$ could not be anymore extracted from the described method in this chapter since the delayed fluorescence freezes at 50-60 K. Nevertheless such a concept will have to be further elaborated and verified probably by other methods and we are working currently in this direction in our group.

4.8. Conclusions

In conclusion we have developed a method for determining the protein relaxation via delayed fluorescence. We have reported a considerable change in the kinetics of the protein relaxation upon electron transfer in R26 *Rb. sphaeroides* reaction centers. Above 160-200 K the characteristic relaxation time obeys very weak Arrhenius temperature dependence. Below 160 K the protein characteristic relaxation times obtain Ferry-type temperature dependence with effective activation energy of 8.10^{-3} eV. So a phase transition temperature in the protein

relaxation mechanisms is identified between 160 K and 200 K which is consistent with many experimental and theoretical contributions in various proteins in slower timescales. Since the solvent is water we are proving that such phase transition in proteins has not only slave character. Opposite temperature dependence of the stretched exponential parameter β than the reported one in the literature was observed and discussed.

5. Sequential *vs.* superexchange charge separation in Vinyl-B_{AB}-R26 reaction centers of *Rb. sphaeroides.*

5.1. Introduction

Bacterial photosynthetic RCs are membrane bound pigment-protein-complexes with a structure[71, 121, 122] optimized to store a photons energy via a series of electron transfer (ET) steps at ~100% quantum yield. The principle of this fundamental process is illustrated in Fig. 1.2. After excitation of the primary donor (P), a bacteriochlorophyll-dimer, an electron is transferred to the bacteriopheophytin H_A within 3 ps[123] to form the charge separated state $P^+H_A^-$. From $P^+H_A^-$ the electron is transferred to the ubiquinone Q_A within about 200 ps[124, 125] and subsequently to Q_B providing an electrochemical potential gradient which drives the dark reactions of energy conversion.

Although the structure is known for almost fifteen years two topics of photosynthetic ET are still in the focus of interest and not completely understood. First, in spite of the high symmetry of the two pigment branches (Fig. 1.2) charge separation (CS) almost exclusively proceeds via the pigment branch denoted A[1] and second, the detailed mechanism of primary ET was long years under debate (see Budil et al.[126] for a recent review). Experimental access to the origin of the highly unidirectional CS will be presented elsewhere [63, 127]. The role of B_A in the CS process is subject of this Chapter as well as to Chapter 6.

Conventionally, details of CS in photosynthetic RCs are modeled with nonadiabatic ET theory. The scenario for the weakly coupled states within this description is dominated by the free energy gap ΔG_{PB} of $P^+B_A^-$ relative to $^1P^*$ [128] ranging from the sequential mechanism, where $P^+B_A^-$ acts as real intermediate electron acceptor, to the superexchange mechanism where $P^+H_A^-$ is directly formed and $P^+B_A^-$ can act as a superexchange mediator, The prerequisites for the validity of nonadiabatic ET theory, weak electronic coupling between the states and thermal equilibration of the vibronic substates much faster than ET, are difficult to reveal experimentally and the functional relevance of alternative/additional processes like dynamic solvation[33, 129-131] and coherent motion of non thermalized vibrational states has been discussed[27, 132, 133]

In this Chapter we utilize the possibility of exchanging the accessory BChl by chemical modified substitutes in order to change ΔG_{PB} (compare Fig. 1.2 and Fig. 5.6).A suitable substitute replacing B_A is 3-vinyl-13^2-OH-BChl. This pigment is identical to BChl except that the acetyl-group at ring I is modified to a vinyl-group and the proton at position 13^2 is substituted against a hydroxy-group (see Fig. 5.1). The vinyl-modification *in vitro* increases the reduction potential by about 1000 cm^{-1} (0.12 eV) as compared to BChl[134] whereas the modification at C-13^2 for itself does not significantly change the redox properties[135] but serves as an anchor for

pigment incorporation into the RCs-matrix without and is not expected to influence the spectral and kinetic properties of the RCs[136-139].

Previous room temperature measurements showed that $^1P^*$ in RCs where the monomeric BChls at B_A and B_B were exchanged against the vinyl-analogue (Vinyl-B_{AB}-R26 RCs) decays with a time constant that is about l0 fold slower than in native RCs (32 ps instead of 3 ps[137]). Unfortunately, these measurements suffered from an incomplete exchange (only about 60% of B_A were exchanged[137]) complicating the evaluation of the exact P lifetime. We have reinvestigated[2] the temperature dependence of $^1P^*$ decay on a Vinyl-B_{AB}-R26 RCs in different solvent (PVA film), where more than 99% of the monomeric BChls were exchanged. In addition we have compared our results with similar measurements in other solvents and on Vinyl-B_A RCs from *Chloroflexus Aurantiacus* where the BChl in the B-branch is replaced by BPhe in comparison with *Rb. sphaeroides.* The results are discussed within conventional nonadiabatic ET and consequences for native RCs are evaluated.

5.2. Vinyl-RCs preparation

RCs of *Rb. sphaeroides* R26 were isolated by standard methods[140]. The isolation of BChl from *Rb. sphaeroides,* its hydroxylation at C-13 by MeOH treatment in the dark and the derivation into 3-vinyl-13^2-OH-BChl by reduction of the 3-acetyl group with $NaBH_4$ and subsequent dehydration is described elsewhere[141] (see Fig. 5.1).

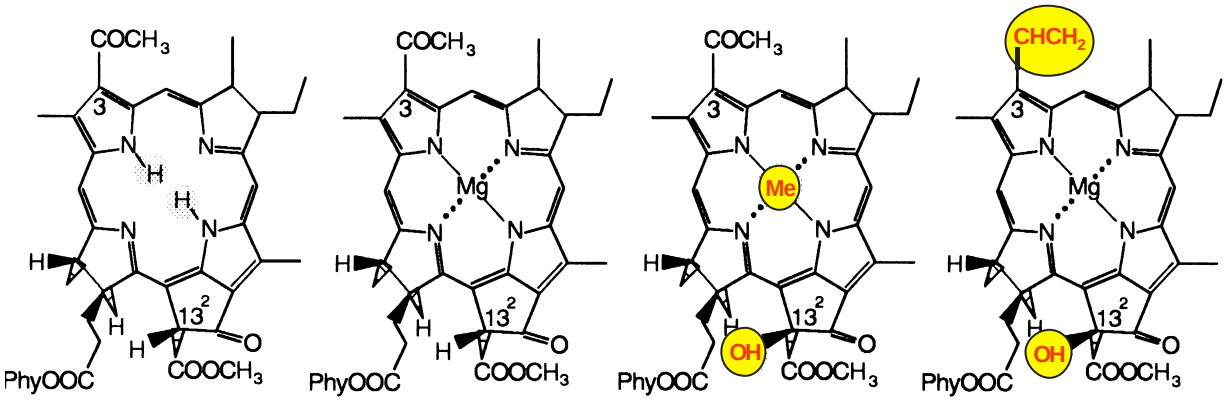

Fig. 5.1. Chemical structure of native and some modified bacteriochlorophylls.

Simultaneous substitution of BChl at B_A and B_B against 3-vinyl-13^2-OH-BChl is achieved by reversible thermal unfolding of the protein RCs of *Rb. sphaeroides* R26 in the presence of an excess of exogenous pigment[136, 138, 139, 142]: RCs in TL-buffer (aqueous buffer at pH = 8.0

containing 10 mM tris(hydroxymethyl)amine-methane and 0.1 Vol% lauryl-dimethylaminoxide (LDAO)) are mixed with a tenfold molar excess of 3-vinyl-13^2-OH-BChl, dissolved in MeOH (final MeOH-concentration: 7 Vol%), incubated for 90 min at 42.7 °C and subsequently purified from exogenous pigment or denatured protein by repeated DEAE-chromatography. Repeating the incubation/purification three times yields RCs with more than 99% of the monomeric BChl exchanged according to HPLC.

5.3. Control of RCs modification

The influence of the thermal exchange of monomeric bacteriochlorophyll at B_A and B_B was put to test by the "self-exchange" of BChl with 13^2-OH-BChl, which *in vitro* and *in vivo* is almost identical to BChl with negligible changes in the spectral properties (5 nm-blue shift of the Q_x-band[136]) and reduction potential (0.01 eV[136]). Introduction of this pigment into the $B_{A,B}$ sites of the RCs does neither affect the kinetics[137] nor properties in absorption[136], fluorescence[5], circular dichroism, ENDOR, ADMR[138, 139] or Stark spectroscopy[5]. It seems well justified to conclude that neither the dynamics nor the protein/cofactor arrangement is influenced by the exchange procedure *per se*. The invariance of the RCs structure to the exchange procedure is additionally supported by X-ray structure and linear dichroism[143] for RCs of *Rb. sphaeroides* where the $B_{A,B}$ and $H_{A,B}$ sites were exchanged showing that the modified pigments are oriented identical to the native ones. Further evidence comes from magnetic field dependent recombination dynamics of $P^+H_A^-$, which are supposed to be very sensitive to structural differences. Both the singlet (k_S) and the triplet recombination rate (k_T) show a reduction by approximately a factor of two, which can be attributed to a weaker superexchange interaction, due to the shift or $P^+B_A^-$ to higher energies [86]. Selfexchanged RCs, i.e. which were subject to the same heating procedure as for the vinyl-exchange, but with native BChl present, show essentially no change within the error of measurement, with a slight tendency to an increased rate.

Furthermore, BChl analogues with different spectral and/or energetic properties conserve these differences after incorporation into the RCs[44, 138, 139, 141-147] but restricted to spectral regions or energy levels determined by the exchanged pigment. No influences on the spectral or energetic properties of the other pigments present have been observed yet. Alterations of excitation energy transfer[147], triplet energy transfer[142, 146], or primary charge separation[44, 137, 144] in such RCs can be assigned to property changes inherent to the modified pigment.

In accordance with the aforementioned are the following observations. The absorption properties of Vinyl-B_{AB}-R26 RCs are identical to those of the unmodified RCs (R26 RCs) in all spectral regions, except the Q_x-and Q_y-bands of monomeric BChl, both of which are blue-shifted

(from 600 to 575 nm and from 800 to 775 nm respectively[142]). There is almost no change of the rate $k_Q(P^+H_A^- \rightarrow P^+Q_A^-)$[148] indicating that the energetics and electronic couplings connected to the states $P^+H_A^-$ and $P^+Q_A^-$ should be (almost) identical to native RCs. On basis of the energetics of $P^+B_A^-$ in native RCs, which is supposed to lie ~0.06 eV below $^1P^*$[44, 128], the increase of the *in vitro* redox potential by 0.12 eV is expected to put $P^+B_A^-$ ~0.06 eV above $^1P^*$ in Vinyl-RCs.

5.4. Temperature Dependence of the Primary Donor Lifetime in Vinyl-RCs

The optically thick solution of RCs was incorporated in an aqueous solution with 0.1 Vol% concentration of LDAO and ~10% concentration of fully dissolved poly-vinyl-alcohol (PVA). The pH was fixed to 8.0 using Tris-Cl buffer with optimal concentration of 60 mM. The PVA solution was dried on a glass plate while purging with dry nitrogen for 35 h at 4°C. A PVA film was obtained with excellent optical quality and high electrical breakdown voltage of more than 2 MV/cm (see Chapter 6). The thickness of the PVA film was estimated to be 9±1 µm. The absorption at 860 nm of the RCs imbedded in the film was OD_{860} ~ 0.05 cm^{-1}. The PVA film is sandwiched between the long sides of two rectangular Plexiglas prisms forming a rectangular cube. Two orthogonal faces of the cube were positioned perpendicular to the direction of excitation and fluorescence detection, orienting the film in 45° to both directions thus minimizing refraction effects. ITO coated mylar foils were placed between the film and the Plexiglas prisms serving as transparent electrodes for electric field dependent time resolved measurements of the film investigated in Chapter 6.

The RCs samples were excited with a portion of the white-light continuum generated in a sapphire plate using the output of RegA 9000, Coherent cw-pumped Ti:Sapphire regenerative amplifier (~200 fs pulses at 800 nm with energy of ~1 µJ at 100 kHz repetition rate). The excitation spectrum was centered at 864nm using interference band-pass filter (10 nm full width at half maximum) with ~200 fs pulses. The rest of the white-light continuum was rejected with at least 3 orders of magnitude. In order to achieve such a rejection for the pump light at 800 nm a holographic notch filter was used with an absorption of more than 4 OD throughout the whole spectrum of the excitation laser (>6 OD at 800 nm). The diameter of the excitation spot was 3-4 mm at maximal pulse energy of 100 pJ corresponding to an average excitation power of <20 µW/cm^2 or 0.04 photons per second per RC. The fluorescence decay collected within a 33 ns time window was detected at right angle with time correlated single photon counting (TCSPC) technique[34]. The instrumental response function (IRF) was 40 ps full width at half maximum. The samples were cooled down to 85 K using RDK 6-320, Leybold Vacuum Cryostat capable of temperature variation between 4 and 400 K. After thermalization the temperature was increased

stepwise. The temperature of the sample was equilibrated for at least half an hour before measuring first the IRF and the fluorescence decay.

Time constants were extracted from the fluorescence decay pattern by fitting a convolution of the IRF and four exponential decay functions to the data using the Levenberg-Marquardt method[7]. Quality of the fit is judged by observing the residuals and values of the reduced $\chi^{(2)}$. This deconvolution method allows resolving lifetimes down to around one half of the IRF.

The $^1P^*$ decays in Vinyl-B_{AB}-R26 RCs at a set of 7 temperatures between 85 and 300 K (same as in Chapter 4) is shown in Fig. 5.2. The fluorescence decay of Vinyl-B_{AB}-R26 RCs can be fitted at all temperatures with four decay times τ_i and the corresponding amplitudes A_i. The data sets obtained from the fits are listed in Table 5.1.

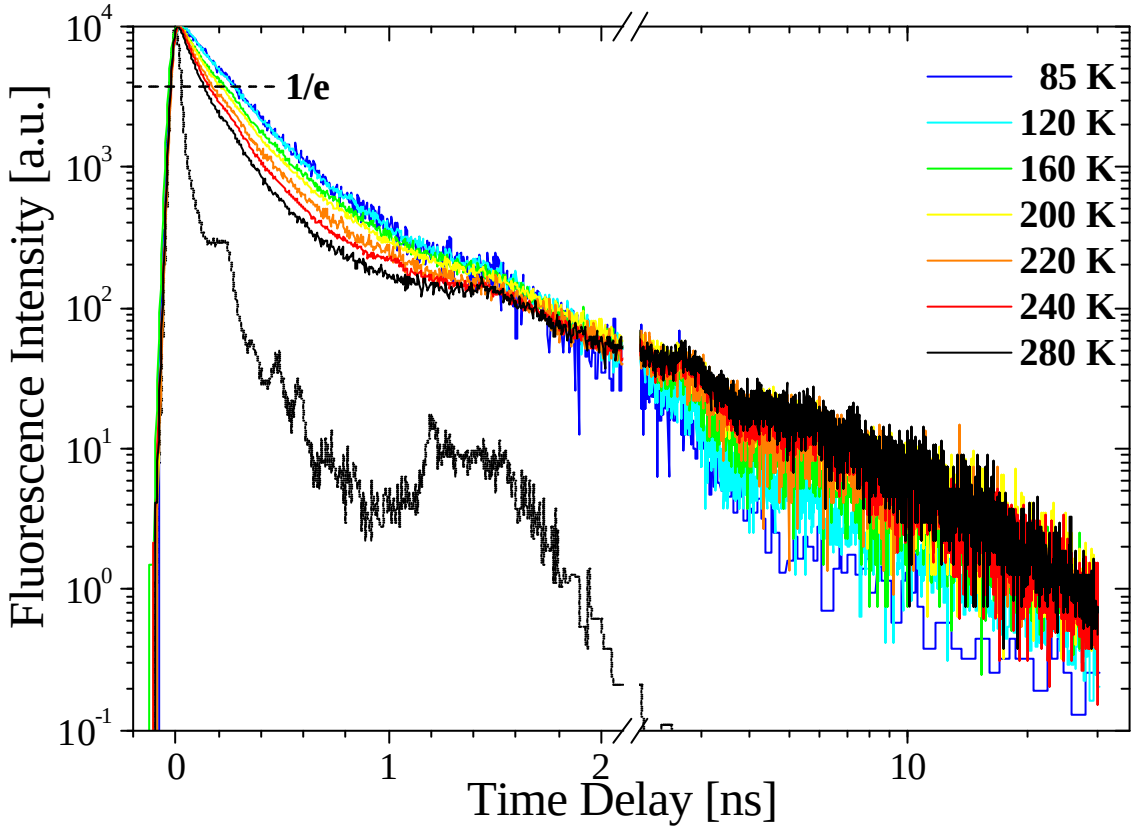

Fig. 5.2. Fluorescence decays of Vinyl-B_{AB}-R26 RCs at temperatures of 85, 120, 160, 200, 220, 240 and 280 K colored in the same way as in Chapter 4. The IRF is represented with dotted line.

As it is evident from Table 5.1, the fluorescence decays are close to mono-exponential, in particular at low temperatures, with dominant amplitude around 90 %. Similarly to native R26 RCs (see chapter 4) a second major components is observed with amplitudes around 10 % at all temperatures indicating dispersive primary charge separation. Slower components with amplitudes below 1 % in the ns range can either result from

(i) delayed fluorescence from minority of Q_A-free RCs; or

(ii) (ii) slow prompt fluorescence reflecting dispersive primary charge separation.

In a Q_A-free minority of RCs the $^1P^*$ fluorescence is always superimposed by some amount of delayed fluorescence from recombination of the radical pair state $P^+H_A^-$as worked out in Chapter 4 for native R26 RCs. From magnetic field dependent measurements of the lifetime of the triplet state $^3P^*$ in vinyl-RCs, it could be shown, that the $P^+H_A^-$ state is 0.165 eV above $^3P^*$, i.e. $P^+H_A^-$ is 0.010 eV higher than in native R26 samples[86]. Thus delayed emission should not be larger than a factor of 1.6 in Vinyl-B_{AB}-R26 RCs as compared to the native samples. Therefore the contribution of delayed fluorescence is becoming significant in comparison to the prompt fluorescence at times smaller than 10 ns. This is evident from the temperature dependent fluorescence decays in Fig. 5.2 because the delayed and the prompt fluorescence experience opposite temperature dependent characteristics in this time range[35] (see Chapter 4). Thus the delayed fluorescence contribution is assumed to be considerably small in comparison with the prompt fluorescence before 10 ns. Indeed the amplitudes of the two slow components are considerably higher than the amplitudes of the same components in Q_A-free R26 RCs (see Table 4.3). In Chapter 4 it was shown they to be dominated by delayed fluorescence. Nevertheless small contribution of delayed fluorescence could be not entirely excluded above 10 ns. It is difficult to determine the exact time when the delayed fluoresce from Q_A-free minority of RCs will become dominant in fluorescence since the time-resolved fluorescence decays are recorded in 33 ns time window. Thus a correct determination of time decay components longer than one third of the experimental time window is obscured[149].

Table 5.1. Results from the fits of the deconvolution of the fluorescence decays with IRF at different temperatures including the ones from Fig. 5.2. $\langle\tau\rangle$ and $\tau_{1/e}$ are calculated from the fit data according to eq. (5.9) and eq. (5.10), respectively

T [K]	$\chi^{(2)}$	τ_1 [ps]	τ_2 [ps]	τ_3 [ns]	τ_4 [ns]	A_1 [%]	A_2 [%]	A_3 [%]	A_4 [%]	$\tau_{1/e}$ [ps]	$\langle\tau\rangle$ [ps]
300	1.32	24	122	0.99	7	71	28	1.0	0.06	38	66
290	1.33	50	163	1.1	8	74	24	1.3	0.11	67	99
280	1.31	38	153	1.1	8	72	26	1.2	0.08	55	87
270	1.43	63	245	1.5	9	85	14	0.77	0.07	75	105
260	1.25	71	295	1.7	11	89	10	0.58	0.04	81	107
250	3.79	80	348	1.9	9	87	13	0.50	0.06	95	129
240	1.71	89	404	2.1	9	90	9.2	0.44	0.07	101	132
230	1.80	98	505	2.9	12	94	5.4	0.26	0.04	106	132
220	1.12	97	437	2.6	17	89	10	0.31	0.04	111	146

210	1.53	94	380	2.0	10	85	14	0.45	0.07	113	150
200	1.13	98	404	2.3	12	86	14	0.39	0.05	117	155
190	1.18	96	412	2.4	13	86	14	0.33	0.04	115	153
180	1.41	139	568	2.6	14	91	8.4	0.19	0.04	154	185
170	1.37	131	507	3.4	17	87	12	0.16	0.02	152	187
160	1.19	111	430	2.7	20	84	16	0.20	0.02	134	170
140	1.11	107	410	2.5	13	81	18	0.12	0.02	133	168
120	1.48	120	402	2.0	12	77	23	0.15	0.02	156	190
100	1.06	138	452	2.2	20	83	17	0.087	0.01	166	194
85	2.32	218	766	1.7	20	97	2.9	0.023	0.01	225	236

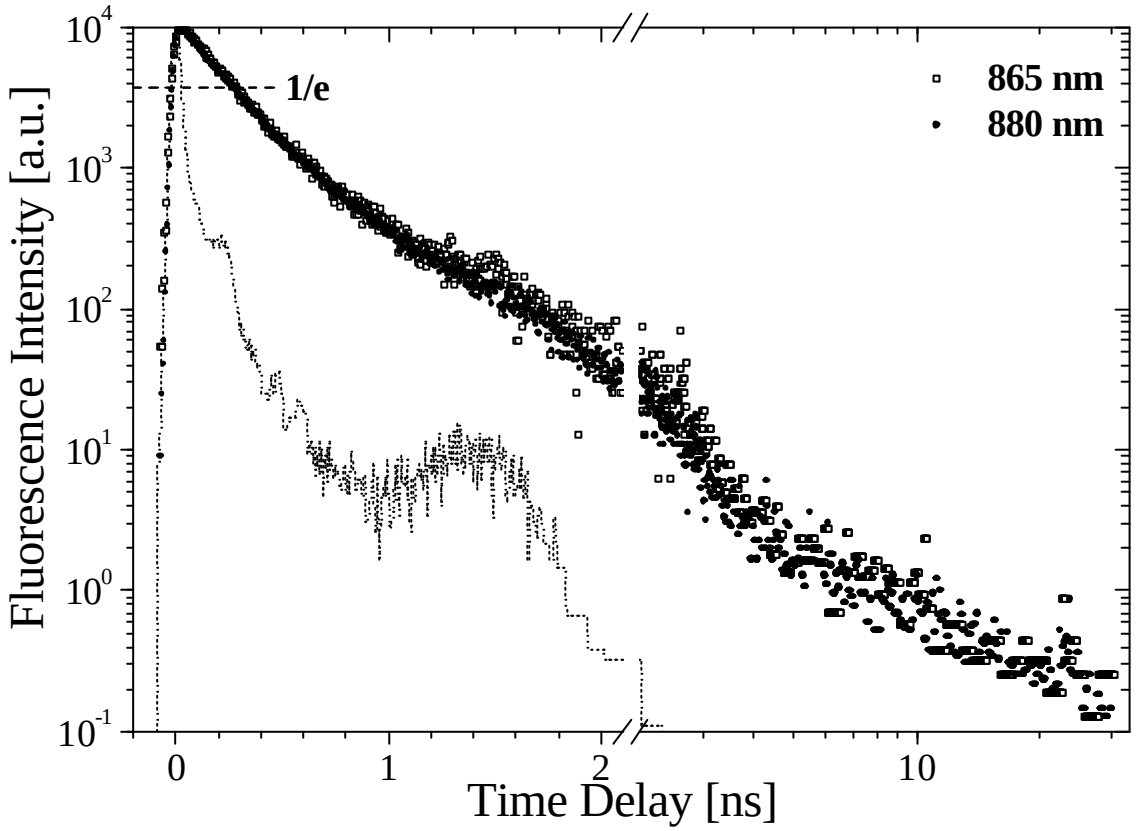

Fig. 5.3. Wavelength dependence of the fluorescence decay at 85 K. The fluorescence decay at 865 nm is plotted with empty squares while the one at 880 nm is plotted with filled circles. The IRF is plotted with dotted line.

In native RCs the existence of more than one $^1P^*$ fluorescence component in addition to delayed fluorescence[44, 69, 73, 150-154] was attributed to dispersive slow primary charge separation[150, 151, 153] resulting from a (static) heterogeneity of the RCs sample as discussed in

Chapter 4. Accordingly, the observation of more than one fluorescence components in the Vinyl-RCs should also reflect (static) heterogeneity. Such heterogeneity arises from a distribution of the free energy differences $\Delta G_{PB}(^1P^* - P^+B_A^-)$ between the excited special pair state and the BChl radical pair state. Since the *in vitro* redox potential of the Vinyl-BChl is altered with ~0.12 eV in comparison with the native BChl, we would expect positive ΔG_B in the order of 0.06 eV. Thus in the Vinyl RCs we will observe heterogeneously activated primary charge separation leading to much more slower and dispersive ET rates than in the nearly temperature activationless primary ET in the native RCs. Such heterogeneity will reflect only the prompt fluorescence and thus the effect due to delayed fluorescence should be much smaller.

The actual use of four decay components for the description of fluorescence is arbitrary as in Chapter 4 and is aimed to describe not distinct kinetic rates but rather to roughly represent a fluorescence decay distribution. In accordance with theoretical considerations of heterogeneous primary CS[128] the relative quantum yield of the second and third components, $a_2.\tau_2$ and $a_3.\tau_3$ increase with decreasing temperature (Table 5.1). To enable comparability at different temperatures a mean $^1P^*$ lifetime could be introduced calculated according to[85, 155]

$$\langle\tau\rangle = \int_0^{+\infty} \frac{F[^1P^*](t)}{F[^1P^*](0)}\,dt = \frac{\sum_{i=1}^{4} a_i.\tau_i}{\sum_{i=1}^{4} a_i} \tag{5.1}$$

where $F[^1P^*](t) = k_F.N[^1P^*](t)$ is the time-dependent fluorescence proportional to the time dependent population $N[^1P^*](t)$ of $^1P^*$. k_F is the radiative decay rate of $^1P^*$ (proportional to the oscillator strength).

Since very slow components contribute strongest to this average time, it is not a good measure of the main components of decay, and could be dominated even by delayed fluorescence components. Instead we use the 1/e lifetime or $\tau_{1/e}$ for comparison of the fluorescence decay at different temperatures. We define $\tau_{1/e}$ as the time at which the fluorescence decay reaches 1/e level (see Fig. 5.2) of its maximum:

$$\frac{F[^1P^*](t=\tau_{1/e})}{F[^1P^*](t=0)} = \frac{1}{e} \tag{5.2}$$

where e is the Euler number. $\tau_{1/e}$ is calculated only numerically and is presented in Table 5.2.

If the fluorescence decay is mono-exponential with effective rate k_{eff} then the 1/e time and the average lifetime are simply equal to the reciprocal of k_{eff}:

$$k_{eff}(T) = \frac{1}{\tau_{1/e}(T)} = \frac{1}{\langle\tau\rangle(T)} \tag{5.3}$$

If a multi-exponential decay of the fluorescence state is anticipated the average lifetime becomes bigger than the 1/e lifetime:

$$k_{eff}(T) \approx \frac{1}{\tau_{1/e}(T)} > \frac{1}{\langle\tau\rangle(T)}. \tag{5.4}$$

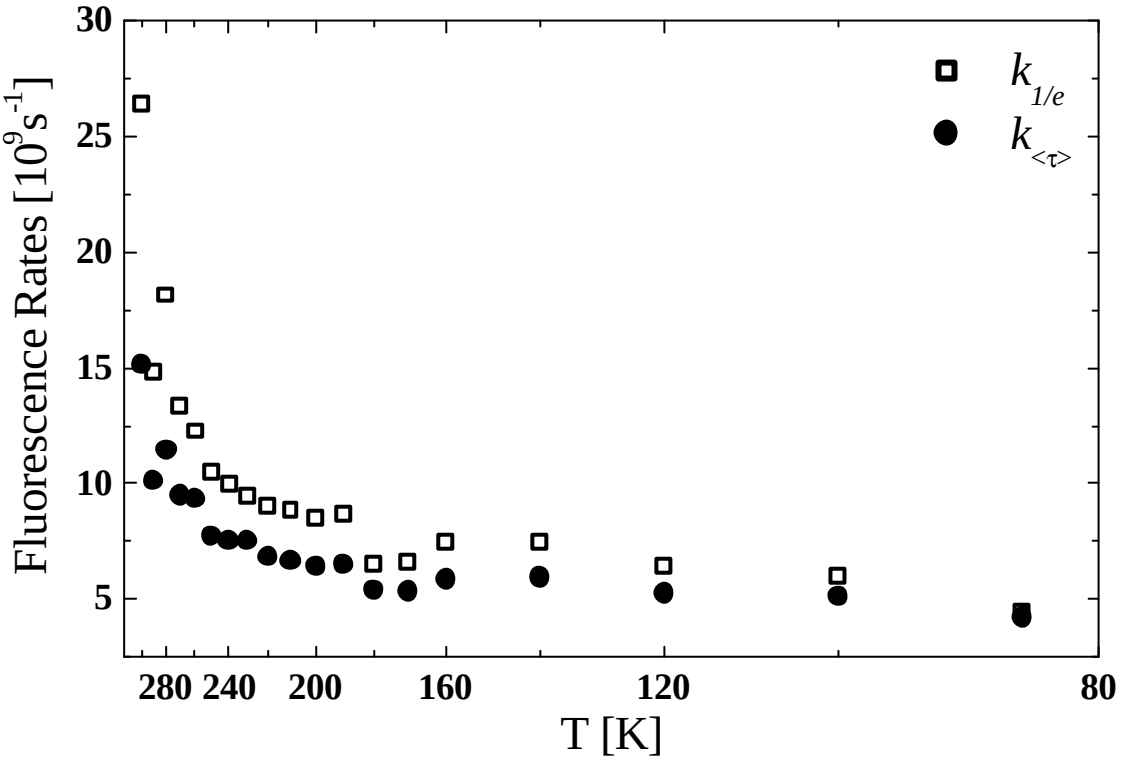

Fig. 5.4. Arrhenius plots of $k_{<\tau>} = <\tau>^{-1}$ (filled circles) and $k_{1/e} = \tau_{1/e}^{-1}$ (empty squares) of the $^1P^*$ decays of Vinyl-B_{AB}-R26 RCs in PVA film.

<τ> experiences large influence of long tails of the fluorescence with very small amplitudes but still considerable quantum yields. Accordingly, a qualitative criterion of dispersion of the fluorescence decay could be introduced by accounting the difference between $\tau_{1/e}$ and <τ>. The bigger <τ> - $\tau_{1/e}$ is the more dispersive the fluorescence. 1/e lifetime is therefore reflecting the fluorescence of the majority of the RCs more correctly than the average lifetime. In Fig. 5.4 the Arrhenius plots or temperature dependence of the 1/e rate $k_{1/e}$ and the average rate $k_{<\tau>}$ defined as reciprocal of the 1/e and the average lifetimes are presented. It is evident from Fig. 5.4 that at high

temperature we have pronounced dispersion of the prompt fluorescence reflecting the dispersive CS through $P^+B_A^-$. At low temperatures especially below 200 K less dispersive behavior of the prompt fluorescence is obtained speaking for a change in the primary CS kinetics. Such a quasi monoexponential fluorescence could be obtained if the direct CS process takes place because it is expected to be almost activationless and thus less dispersive.

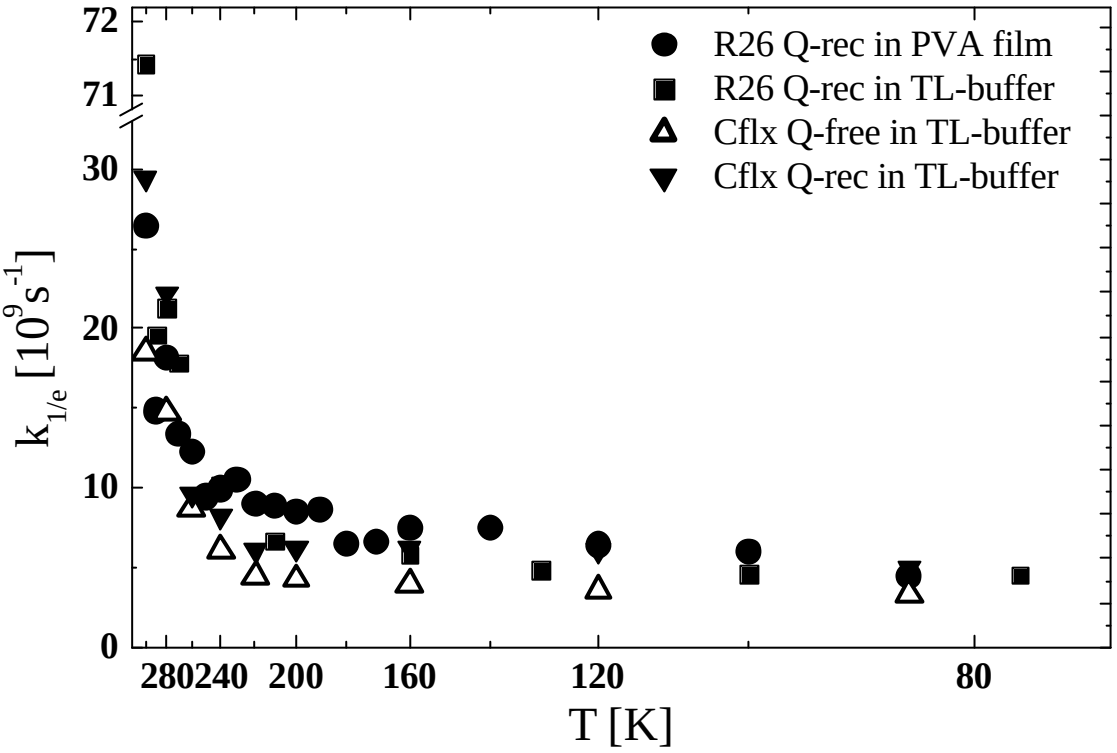

Fig. 5.5. Arrhenius plots of $k_{1/e} = \tau_{1/e}^{-1}$ for Q_A-containing Vinyl-B_{AB}-R26 *Rb. sphaeroides* RCs in TL-buffer (filled circles) and imbedded in PVA film (filled squares) and for Q_A-free and Q_A-containing Vinyl-B_A *Chloroflexus Aurantiacus* RCs in TL-buffer (empty and filled triangles, respectfully).

While the absorption band of $P \rightarrow {}^1P^*$ experiences a temperature dependent red shift from the maximum absorption wavelength at 865 nm at ambient temperature to 890 nm at 10 K [156], the fluorescence band of ${}^1P^* \rightarrow P$ has a temperature independent maximum at around 920 nm. In case of constant excitation and detection conditions, such an excitation wavelength dispersion could potentially induce a changes in $<\tau>$ and $\tau_{1/e}$ not originating from the activation of charge separation, but rather reflecting selective excitation of different subpopulations of P. Therefore we examined the excitation wavelength dependence of the fluorescence in Fig. 5.3. It is evident that there is no excitation wavelength dependence between the fluorescence decays at excitation at the blue wing and at the maximum of the absorption band at 85 K.

In Fig. 5.5 the temperature dependence of $k_{1/e}(T)$ (Arrhenius plot) is presented for Vinyl-B_{AB}-R26 RCs at a set of 19 temperatures. It is evident from there that above 180-200 K we have a strongly activated temperature dependence of the $k_{1/e}(T)$ while below this temperature $k_{1/e}(T)$ is almost temperature independent. The data is compared with the experiments on a similar sample[2] in aqueous solution which give equivalent Arrhenius plots within the experimental uncertainty at low temperatures. At high temperatures the 1/e lifetimes are decreasing with temperature faster in aqueous solution than in PVA. This speaks that the 1/e time of the fluorescence decay and thus the primary CS in Vinyl-RCs are stronger activated in TL-buffer (aqueous solution) than in PVA showing influence from solvent polarity, viscosity or freezing point on the ΔG_{PB}.

The same measurement procedure was applied for studying Vinyl exchanged RCs from *Chloroflexus Aurantiacus* (Cflx) bacteria[51, 157]. The difference between RCs from R26 *Rb. sphaeroides* and Cflx is that the B-branch BChl is replaced by BPhe. Thus their kinetics would be interesting for examination of the influence of possible B-branch ET in Vinyl exchanged RCs via comparing with R26 Rb. sphaeroides. The results of the preliminary measurements of these RCs are shown in Fig. 5.5. One can see that there is slightly different behavior in the Arrhenius plot comparable with the solvent induced differences on R26 RCs. One reason could be the 10 fold higher concentration of LDAO into the Cflx Q_A-containing sample in comparison with the other 3 samples presented in Fig. 5.5. The Cflx Q_A-free Arrhenius plot shows a small offset which could be due to a small contribution of delayed fluorescence. For more quantitative analysis a comparison with Q_A-free R26 RCs is needed.

5.5. Kinetic model

The fluorescence decay kinetics in Fig. 5.2 and Table 5.1 shows a slight dispersion of kinetics, which is most pronounced at high temperatures, where the kinetics are thermally activated. Thus kinetic dispersion seems to result from a distribution of activation barriers. We therefore refer the maximum of the kinetics represented by $k_{1/e}$ to a minimum of the activation barriers. We propose these barriers to result from the increased redox potential of $P^+B_A^-$ on the basis of the kinetic and energetic scheme sketched in Fig. 5.6, and will try to model the temperature dependence of the $^1P^*$ decay of Vinyl-RCs. In the following we will consider only the maximum $k_{1/e}$ of the distribution of rates.

According to Fig. 5.6 the CS process can be either sequential ($^1P^* \rightarrow P^+B_A^- \rightarrow P^+H_A^-$) or direct ($^1P^* \rightarrow P^+H_A^-$). In the following we will explicitly allow for a simultaneous contribution of both kinetic pathways at all temperatures (sequential and direct mechanism[128, 158]). The first step in

the sequential pathway is expected to be activated and thus, the reverse recombination process $^1P^* \leftarrow P^+B_A^-$ has to be taken into account. Since the minor delayed fluorescence contributions can be neglected from the overall $^1P^*$ fluorescence before ~10 ns, we may neglect both, the direct CS and the second step of sequential CS.

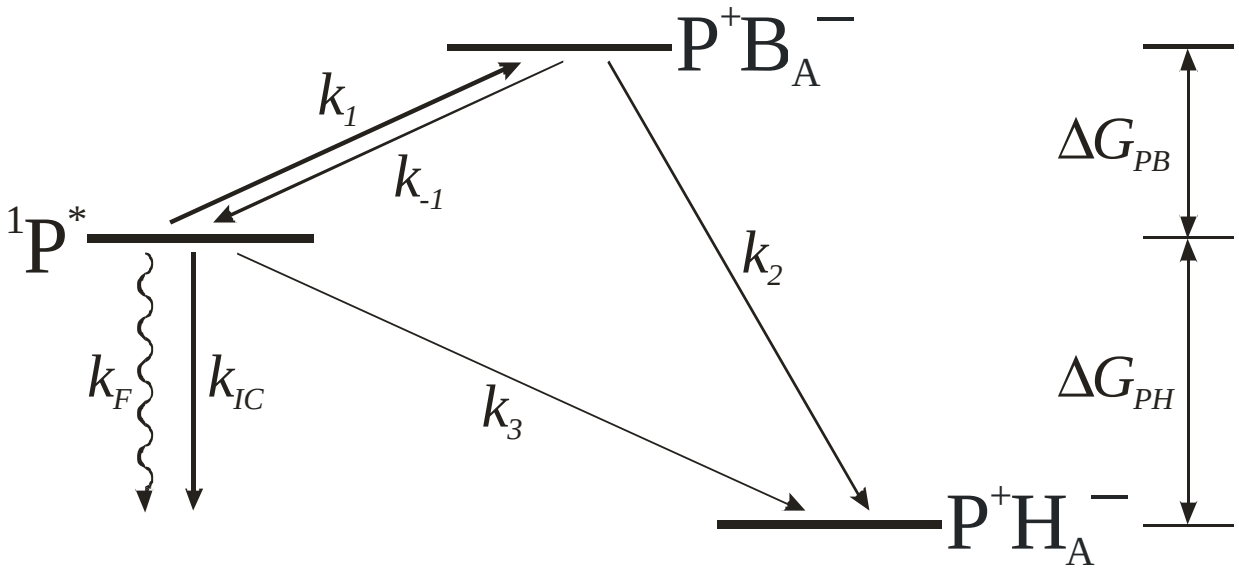

Fig. 5.6. Kinetic model assuming single states for $^1P^*$, $P^+B_A^-$ and $P^+H_A^-$. The free energy difference between $^1P^*$ and $P^+B_A^-$ is denoted with ΔG_{PB} (positive) and between $^1P^*$ and $P^+H_A^-$ is denoted with ΔG_{PH} (negative).

Due to the rather long $^1P^*$ lifetimes in Vinyl-RCs (Table 5.1) deactivation channels other than primary (A-branch) charge separation may operate. Possible channels are internal conversion (IC) to the ground state of P, intersystem crossing (ISC) to the triplet state of P, natural fluorescence (F) or even B-branch ET. Natural fluorescence ($k_F \sim (18\ \text{ns})^{-1}$[159]) and ISC ($k_{ISC} < (6\ \text{ns})^{-1}$[148]) are slow and can be neglected without loss of accuracy. In view of the extremely low quantum yield of B-branch CS in native RCs (~0.1%Hartwich, 1997 #794; Kellogg, 1989 #1149]) this contribution can also be neglected for the symmetrically modified Vinyl-B_{AB}-R26 RCs. For both samples IC has to be considered as quantum yield measurements on similar samples[148] reveal an IC rate of $k_{IC} \sim (1\ \text{ns})^{-1}$ (which also applies for native RCs). Thus, the kinetic model in Fig. 5.6 provides an adequate description of the $^1P^*$ decay (Table 5.1) and the relevant differential equations are:

$$\frac{d[^1P^*]}{dt} = -(k_1 + k_3 + k_{IC}) \cdot [^1P^*] + k_{-1} \cdot [P^+B_A^-] \qquad (5.5a)$$

$$\frac{d[P^+B_A^-]}{dt} = k_1 \cdot [^1P^*] - (k_{-1} + k_2) \cdot [P^+B_A^-] \qquad (5.5b)$$

where the rates k_{IC}, k_1, k_{-1}, k_2 and k_3 correspond to the reactions defined in Fig. 5.6. [$^1P^*$] and

$[P^+B_A^-]$ are the concentrations of the states. These equations can be facilitated assuming steady state for the concentration of the state $P^+B_A^-$, i.e. $d[P^+B_A^-]/dt = 0$. This assumption is justified since the following two conditions[149, 160] are met at all temperatures: (i) an equilibration time $(k_{-1}+k_1)^{-1}$, which is fast compared to the actual decay and (ii) a low steady state concentration of $P^+B_A^-$ relative to $^1P^*$. Substitution of $[P^+B_A^-]$ in Eq. (5.5a) according to $[P^+B_A^-] = k_1/(k_{-1}+k_2).[^1P^*]$ shows that the $^1P^*$ deactivation covered by the scheme in Fig. 5.6 essentially is mono-exponential (see Appendix C) with an effective rate:

$$k_{eff} = \frac{k_1 k_2}{k_{-1} + k_2} + k_3 + k_{IC} \tag{5.6}$$

Due to detailed balance the ratio between the forward and the backward primary ET rate from $^1P^*$ to $P^+B_A^-$ is represented by the approximated Boltzmann factor (see Appendix B):

$$\frac{k_1}{k_{-1}} = exp\left(-\frac{\Delta G_{PB}}{k_B T}\right) \tag{5.7}$$

and thus the effective decaying rate of the fluorescence from eq. (5.6) can conveniently be presented as:

$$k_{eff}(T,\Delta G) = \frac{1}{\tau_B} exp\left(-\frac{\Delta G}{k_B T}\right) + k_3(T) + k_{IC}(T) \tag{5.8}$$

where k_B is the Boltzmann constant and

$$\tau_B = k_{-1}^{-1} + k_2^{-1} \tag{5.9}$$

is the effective $P^+B_A^-$ radical pair depopulation time. This time is supposed to be very weakly temperature dependent for the following reasons:

(i) k_{-1} is expected to be similar to k_1 in the native RCs, because the energy of $P^+B_A^-$ is expected to be about 0.12 eV higher than in native RCs. Since the energy difference between $P^+B_A^-$ and $^1P^*$ in native R26 RCs is around -0.06 eV one would expect an energy difference ΔG_B between $P^+B_A^-$ and $^1P^*$ in Vinyl-B_{AB}-R26 RCs also in the order of +0.06 eV, i.e. for the rate k_{-1} we have the same negative driving force as for k_1 in native RCs. Assuming that the reorganization energy does not change(λ is around 0.06 eV, see Chapter 3) we would expect k_{-1} to be activationless.

(ii) k_2 is found to be almost activationless in native R26 RCs[144]. Due to the difference in redox

potential, the driving force is expected to increase to ΔG = -0.18eV with the consequence that the rate should be slightly in the inverted region. With $\lambda \tilde{} 0.06$ eV we get an activation barrier of only 0.0073 eV, which still leads to an inverted temperature dependence to the rate between 290K and 180K, since:

$$\sqrt{\frac{180K}{290K}}\frac{e^{-\frac{0.0073}{k_B 290K}}}{e^{-\frac{0.0073}{k_B 180K}}}=0.943$$

We will see from the results of our analysis, that the assumptions concerning the energetics are justified.

The kinetic model yielding eq. (5.8) was exploited for deconvolution of the temperature dependent $k_{eff}(T)$ in Fig. 5.6 and Fig. 5.7. The temperature dependence of the internal conversion rate $k_{IC}(T)$ was taken from experimental data on a similar sample[148] and was approximated with:

$$k_{IC}(T) = k_{IC}(\infty)exp\left(-\frac{E_a}{k_B T}\right) \tag{5.10}$$

where $k_{IC}(\infty)$ = (0.6 ns)$^{-1}$ and E_a = 0.005 eV. Such a lack of pronounced temperature dependence is quite common for internal conversion processes. The temperature dependence of $k_3(T)$ was assumed to be described by the nonadiabatic, high temperature Marcus equation eq. (3.19) (see Chapter 3):

$$k_3(T) = \frac{1}{\sqrt{T}}.\left[k_3^0\, exp\left(-\frac{E_{3a}}{k_B T}\right)\right] \tag{5.11}$$

where k_3^0 and the effective activation energy E_{3a} were fit parameters. The results of the fit are presented in Fig. 5.7. An unusually high temperature barrier of more the 0.2 eV was deduced from the fit. Such a value would yield an increase of the redox potential of the Vinyl-BChls *in vivo* by 0.32 eV, which is significantly larger than value of 0.12 eV observed *in vitro*. Furthermore unphysical short depopulation times of $P^+B_A^-$ of sub-fs are derived from the fit data, and which are in gross contradiction to the ~4 ps observed in native RCs at more favorable energy conditions. In fact such fast time is already well in the adiabatic range of electron transfer. Such a tremendous difference would imply an increase of the coupling by at least a factor of 50 without any visible reason. Thus it is evident that the description of the primary ET in Vinyl-B_{AB}-R26 RCs with the above made assumptions is questionable.

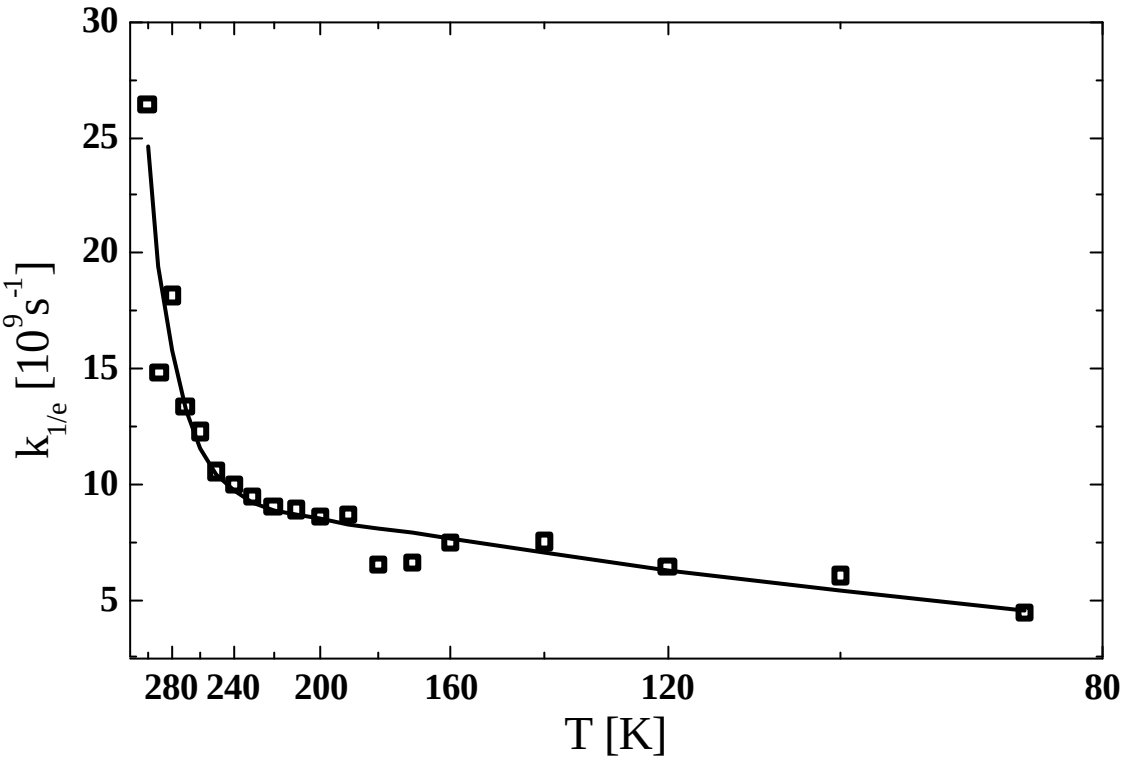

Fig. 5.7. Arrhenius plot of the 1/e rate (empty squares) and fit with the kinetic model from eq. (5.8). The fit parameters are τ_B = 0.3 fs, ΔG_{PB} = 0.32 eV, k_3(280 K) = (71 ps)$^{-1}$ and E_{3a} = 0.014 eV.

5.6. Kinetic model including temperature dependence of the depopulation rate of $P^+B_A^-$.

As discussed above the energy ΔG_{PB} is expected to be around 0.06 eV, so that the backward rate k_{-1} (see Fig. 5.6) could be similar to k_1, the primary CS rate ($^1P^* \rightarrow P^+B_A^-$) in native R26 RCs, i.e. activationless. It has been already established by temperature dependent measurements, that this rate is satisfactorily described by single mode approximation in the ET theory[71, 144] (see Chapter 3). The secondary rate k_2 in native R26 RCs ($P^+B_A^- \rightarrow P^+H_A^-$) is also well described by the single mode approximation, but with 3 times lower frequency for the low frequency averaged mode of the surrounding[144]. In Fig. 3.8 a simulation of the free energy dependence of the logarithm of the ET rate in the case of Marcus, single mode and multi mode ET regime is shown. It turns out that around the activationless point in the Marcus parabola the Marcus formula is a good approximation to the Marcus-Jortner-Levich formula for the single mode ET. Checking the literature data from Lauterwasser et al.[144] it becomes evident that even for 85 K the both dependences coincide within 2 % up to 0.2 eV (see Fig. 3.8.).

From the 3D structure we do not expect a dramatic simultaneous increase of the couplings for both rates ($^1P^* \rightarrow P^+B_A^-$) and ($P^+B_A^- \rightarrow P^+H_A^-$). This notion is further supported by the observed similarity of recombination rates, as discussed above. Accordingly, as a first approximation we assume that the reorganization energies and average protein mode frequencies are similar to the ones determined for native R26 RCs. Then the only free parameter different from the native case is the energy of the $P^+B_A^-$. Consequently in the approximation of the ET rate based on the Marcus equation (3.19) we obtain for the depopulation time τ_B of $P^+B_A^-$ from eq. (5.9):

$$\tau_B = \frac{\hbar}{2\pi}\sqrt{4\pi k_B T}\left\{\frac{\sqrt{\lambda_{12}}}{|V_{12}|^2}\exp\left[\frac{(-\Delta G_{PB}+\lambda_{12})^2}{4\lambda_{12}k_BT}\right]+\frac{\sqrt{\lambda_{23}}}{|V_{23}|^2}\exp\left[\frac{(\Delta G_{PH}-\Delta G_{PB}+\lambda_{23})^2}{4\lambda_{23}k_BT}\right]\right\} \quad (5.12)$$

where[144] $\lambda_{12} \sim 0.06$ eV, $\lambda_{23} \sim 0.19$ eV, $V_{12} \sim 20$ cm^{-1}, $V_{23} \sim 40$ cm^{-1}. At these values and assuming activationless ET for the native RCs ($\Delta G_{PH} = -\lambda_{12} - \lambda_{23}$) the values of the two terms in the brackets in eq. (5.12) are comparable. So we can deduce a working formula for the temperature dependence of τ_B:

$$\tau_B = \frac{\hbar}{2\pi}\sqrt{4\pi k_B T}\left\{\frac{\sqrt{\lambda_{12}}}{|V_{12}|^2}\exp\left[\frac{(-\Delta G_{PB}+\lambda_{12})^2}{4\lambda_{12}k_BT}\right]+\frac{\sqrt{\lambda_{23}}}{|V_{23}|^2}\exp\left[\frac{(\Delta G_{PB}+\lambda_{12})^2}{4\lambda_{23}k_BT}\right]\right\} \quad (5.13)$$

where T is temperature and ΔG_{PB} is the energy difference between $^1P^*$ and $P^+H_A^-$. Now we can insert eq. (5.13) in eq. (5.8) and a new expression for the effective rate will be derived considering the temperature dependence of the depopulation time τ_B of $P^+B_A^-$, the internal conversion rate from eq. (5.10) and the direct rate from eq. (5.11):

$$k_{eff} = \frac{1}{\tau_B(T,\Delta G_{PB},\lambda_{12},\lambda_{23},V_{12},V_{23})}\exp\left(-\frac{\Delta G_{PB}}{k_BT}\right)+k_3(T)+k_{IC}(T) \quad (5.14)$$

The results of the fit are presented in Fig. 5.8. The fit showed week dependence on the couplings, which we have varied slightly keeping the ratio between them between $1:2$ [144] and $1:\sqrt{3}$ [161]. A value for the activation energy of ΔG_{PB} of around 0.05 eV comprising for the energy shift *in vivo* of the redox potential of Vinyl-BChls a value of 0.11 eV close to the redox potential shift *in vitro*. A larger value of ΔG_{PB} would be expected for the Vinyl-B_{AB}-R26 RCs in aqueous solution, as it is evident from Fig. 5.5.

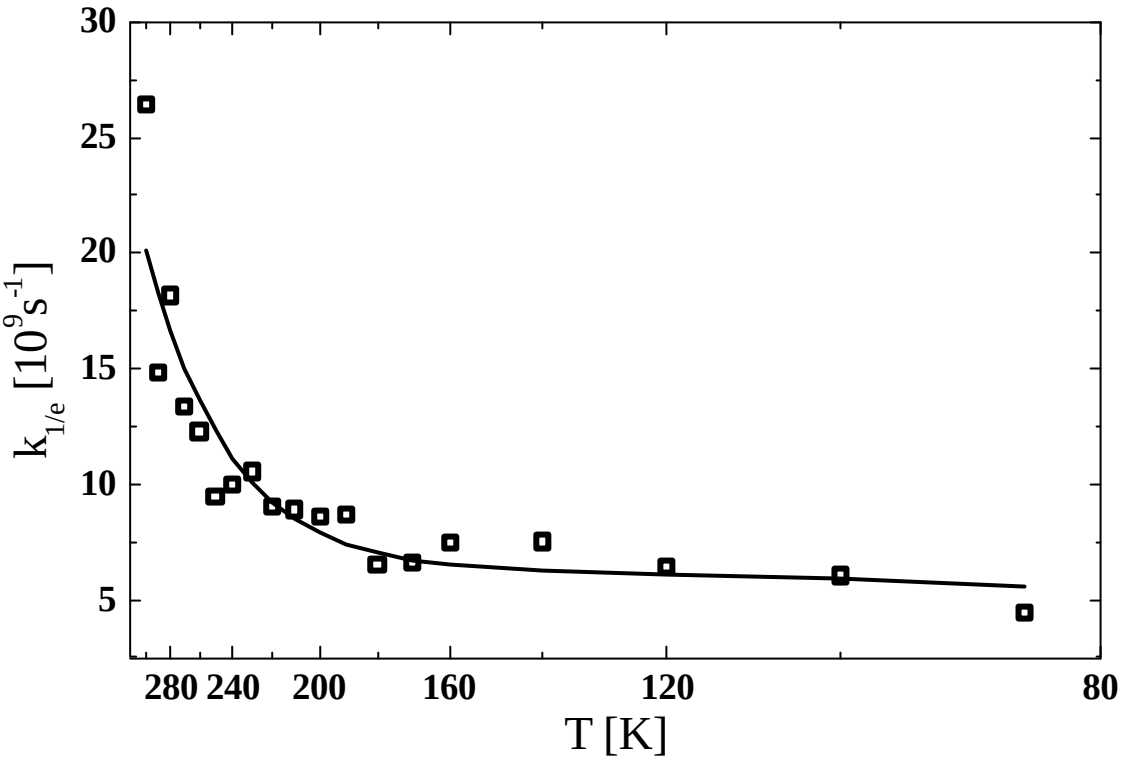

Fig. 5.8. Convolution of the Arrhenius plot for the $k_{1/e}$ rate according to the eq. (5.14) implying eq. (5.10 - 5.11) and eq. (5.13). The fit gave ΔG_{PB} = 0.05 eV, λ_{23} = 0.04 eV, E_{3a} = 0 eV within the fit uncertainty and $k_3^0 = k_3$ = (350 ps)$^{-1}$. The fitted parameters yielded a τ_B value of ~5 ps at 300 K.

Reasonable fit results were obtained for reorganization energies of the secondary ET step ($P^+B_A^- \rightarrow P^+H_A^-$), which turns out to be smaller than the reorganization energy for the primary ET step ($^1P^* \rightarrow P^+B_A^-$). Indeed simulations show, that the temperature dependence of τ_B becomes dominant in eq. (5.14) only when $\lambda_{12} > \lambda_{23}$ (see Fig. 5.9). In this case it is more pronounced than the temperature dependence due to the Arrhenius factor in eq. (5.14), reflecting k_1.

Due to the limited accuracy of the experimental data there is considerable uncertainty of the reorganization energies and of the couplings which were obtained from the fit. Nonetheless it is evident according to our assumption for $\Delta G_{PH} = -\lambda_{12} - \lambda_{23}$ that λ_{23} should be much smaller than previously determined (0.04 eV vs. 0.19 eV[144]). Such an effect could explain also the small values of the free energy difference between the special pair and the BPhe radical pair determined in Chapter 4 and Appendix C. Indeed the reorganization energies λ_{12} and λ_{23} have different character since the first reflects ET involving creation of a strong dipole moment and the second reflects charge shift reaction considering an increase of the already created dipole moment and thus having smaller distance dependence[21].

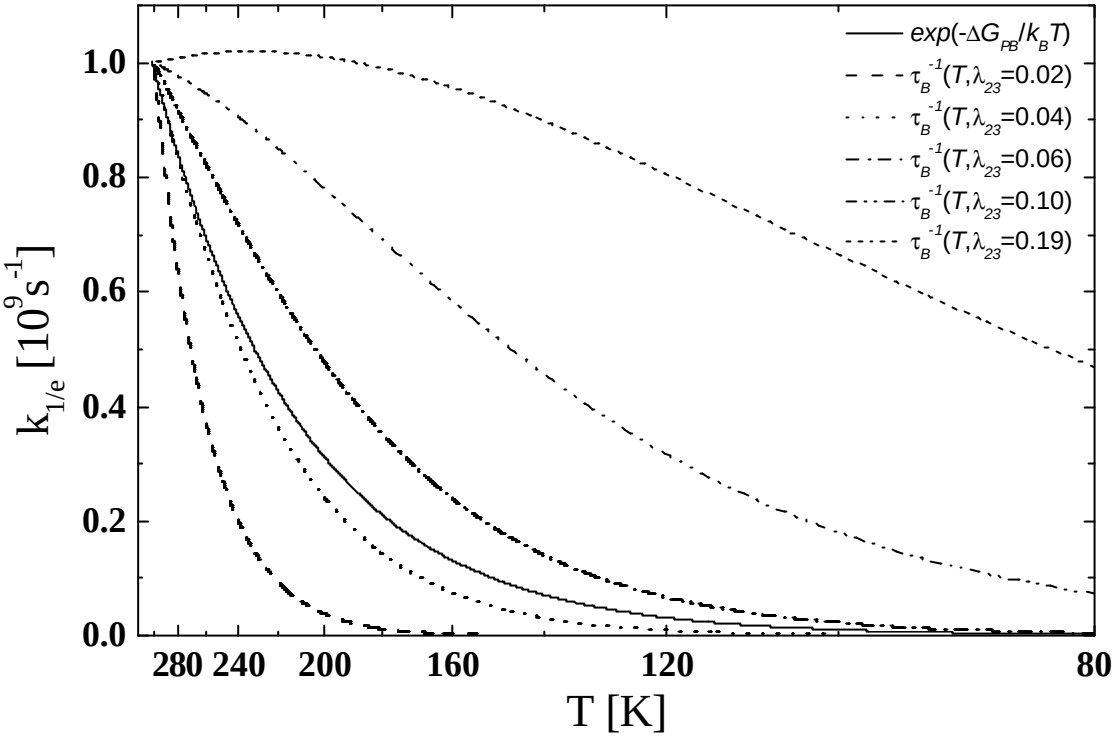

Fig. 5.9. Temperature dependence of τ_B^{-1} for V_{12} = 20 cm^{-1}, V_{23} = 40 cm-1, $\lambda_{12} = \Delta G_{PB}$ = 0.06 eV and λ_{23} = 0.04, 0.06, 0.10 and 0.19 eV (nonsolid lines) in comparison with exponential decay with activation energy of ΔG_{PB} = 0.06 eV (solid line). All functions are normalized to their values at 300 K.

5.7. Kinetic model considering the inhomogeneous distribution of $P^+B_A^-$ radical pair free energies

In native RCs the existence of more than one $^1P^*$ fluorescence component in addition to delayed fluorescence[44, 69, 73, 150-154] was attributed to dispersive slow primary charge separation[34, 35, 85, 150, 151, 153] resulting from a heterogeneity of the RCs sample as discussed in Chapter 4. Accordingly, the observation of more than one fluorescence components in the Vinyl-RCs should also reflect energetic heterogeneity. Such heterogeneity arises from a distribution of the free energy differences ΔG_{PB} ($^1P^*$ - $P^+B_A^-$) between the excited special pair state and the BChl radical pair state. Thus in the Vinyl RCs we expect to observe heterogeneously activated primary charge separation leading to much more slower and dispersive ET rates than in the nearly temperature activationless primary ET in the native RCs. Such heterogeneity will be reflected in prompt fluorescence. In order to account for the inhomogeneity of the $P^+B_A^-$ radical pair free energies the effective decaying rate of the fluorescence from eq. (5.14) can be replaced by:

$$k_{eff}^{in}(T) = \int_{-\infty}^{+\infty} d(\Delta G_{PB}) \int_{-\infty}^{+\infty} d(\Delta G_{PH})\rho(\Delta G_{PB})\rho(\Delta G_{PH})k_{eff}(T, \Delta G_{PB}, \Delta G_{PH}) \quad (5.15)$$

where $\rho(\Delta G_{PB})$ reflects the distribution of $P^+B_A^-$ radical pair free energies and $\rho(\Delta G_{PH})$ reflects the distribution of $P^+H_A^-$ radical pair free energies. The different parts of the rate distribution contribute differently to the fluorescence[85, 91].

The relatively small activation energy deduced for k_3 speaks for the activationless character of the direct rate. Consequently we will expect very weak dependence on the inhomogeneous distribution of the free energy between the special pair and the BPhe radical pair ΔG_{PH} ($^1P^*$ - $P^+H_A^-$). Similarly we would expect weak dependence also for the backward rate k_1. Larger dependence on the inhomogeneous distribution of both ΔG_{PB} and ΔG_{PH} is expected for the k_2 rate, which is slightly in the inverted region. As a first approximation we will consider all of the rates, couplings and reorganization energies in eq. (5.14) independent of the inhomogeneity except of the Boltzmann factor. Then for $k_{eff}^{in}(T)$ assuming a Gaussian distribution for $\rho(\Delta G_{PB})$ (see Appendix A) we obtain:

$$k_{eff} = \frac{1}{\tau_B\left(T, \Delta G_{PB}^{app}, \lambda_{12}^0, \lambda_{23}^0, V_{12}^0, V_{23}^0\right)} exp\left(-\frac{\Delta G_{PB}^{app}}{k_B T}\right) + k_3^0(T) + k_{IC}^0(T) \quad (5.16)$$

where ΔG_{PB}^{app} is the apparent energy defined as if we would have single states for $^1P^*$ and $P^+B_A^-$. According to Appendix B we obtain:

$$\Delta G_{PB}^0 = \Delta G_{PB}^{app} + \frac{\sigma^2}{2k_B T} \quad (5.17)$$

where ΔG_{PB}^0 is the mean value or center of gravity and σ is the half width of the distribution. According to this most simplest approach treating the influence of the inhomogeneity in Vinyl RCs we would have to correct our fit values for ΔG_{PB}^0 adding a temperature dependent factor $\frac{\sigma^2}{2k_B T}$.

$$k_{eff} = \frac{1}{\tau_B\left(T, \Delta G_{PB}^0 - \sigma^2/2k_B T, \lambda_{12}^0, \lambda_{23}^0, V_{12}^0, V_{23}^0\right)} exp\left[-\frac{\Delta G_{PB}^0}{k_B T} + \frac{\sigma^2}{2(k_B T)^2}\right] + k_3^0(T) + k_{IC}^0(T) \quad (5.18)$$

In Chapter 4 we have deduced a value of σ = 0.025 eV for the width of the Gaussian distribution of the $P^+H_A^-$ free energy, assuming that it is temperature independent, and σ = 0.033 eV,

assuming that it is temperature dependent similar to Warshel et al.[66]. According to the only one contribution in the literature[66] we may consider that the inhomogeneity of the free energies of the radical pairs are induced only by the presence of charge and not of a dipole moment in the protein. In this case one would expect a similar value for the width of the Gaussian distribution for $P^+B_A^-$ and $P^+H_A^-$ free energy distributions[66]. Using σ=0.025 eV, a fit of eq. (5.18) to the experimental data yields a value of ΔG_{PB}^0=0.08 eV. If we perform fit of the Arrhenius plot using eq. (5.18) with the temperature dependence of σ as given in Appendix C, then the result gives us similar value for ΔG_{PB}^0 of 0.06 eV. This value comprises a shift of the redox potential shift from native BChl to the Vinyl BChl *in vivo* identical to the one obtained *in vitro*.

With decreasing temperature ΔG_{PB}^{app} from eq. (5.16) and eq. (5.17) is decreasing according to eq. (5.18). This accounts for the fact that more and more high lying states in the radical pair energy distribution are obtaining slower ET rates in comparison with the cutoff rates of the direct CS to $P^+H_A^-$ and internal conversion processes.

More exact treatment of the inhomogeneity contribution to the 1/e fluorescence lifetime could be performed numerically solving eq. (5.15). Such an approach is hindered by the very small temperature range in which the experimental data show thermally activated behavior and by the small time range in which CS is accessible before cutoff due to internal conversion and direct CS becomes effective.

Since the lifetime of $P^+B_A^-$ is very short during the CS process, protein relaxation as a response to the dipole moment of $P^+B_A^-$ is negligible in our investigations in this Chapter.

5.8. Superexchange enhanced electron transfer below 200 K.

The values for the direct rate k_3 obtained from the fit in Fig. 5.8 and its lack of temperature dependence show that it is an activationless rate of k_3 = (350 ps)$^{-1}$. There are two possibility for such a temperature independent direct rate i) nuclear tunneling or ii) activationless ET rate. The nuclear tunneling although is expected at much lower temperatures $k_BT << \hbar\omega$. For the protein phonon spectrum we have information that it is significantly different from zero between 80 and 100 cm^{-1}[28, 152]. This would imply a highest limit ($k_BT \approx \hbar\omega$) for nuclear tunneling in RCs to be around 120-140 K which is considerable lower than 200 K.

Therefore we assume case (ii) yielding $\Delta G_{PH} = \lambda_{13}$. Using ΔG_{PH}(t < 200 ps) ˜ 0.1 eV (determined from the delayed fluorescence of the unmodified RC at low temperatures (see Chapter 4) and from the temperature dependence of the Vinyl-$B_{A,B}$-RCs in section 5.6) we would

obtain $\lambda_{13} \sim \lambda_{12}+\lambda_{23}$ = 0.1 eV. According to eq. (3.19) we determine the effective electronic coupling for the direct rate k_3 as V_{13} = 1.4 cm^{-1}.

The value of $\lambda_{13} \sim$ 0.1 eV is smaller than the corresponding parameter for the back reaction into the triplet state: ${}^3k_{31}({}^3P^+H_A^- \rightarrow {}^3P^*)$ for which a value of $\lambda_{13} \sim$ 0.2 eV was determined[62], while the electronic coupling for ${}^3k_{31}$ of V_{31} = 1 cm^{-1} is smaller than the coupling which is derived for an activationless k_{13}. It was shown for the back transfer rate that the electronic coupling is increased by superexchange (approximately by a factor of 2)[62]. Thus we also expect the coupling V_{13} to be governed by the superexchange mechanism[161]. Due to the smaller vertical energy difference $\delta E = \Delta G+\lambda$ between ${}^1P^*$ and $P^+B_A^-$ being effective for V_{13} according to eq. (3.24) as compared to the vertical energy difference between $P^+H_A^-$ and $P^+B_A^-$ responsible for V_{31}, we indeed expect a slight increase of the superexchange coupling for V_{13} This indeed corroborates the notion that the superexchange mechanism might be effective for these processes.

The relatively small contribution of the superexchange enhancement to the direct coupling (~40%) could also suggest that uncertainties of the interpigment distances as well as distance dependence parameters for the RC protein could also be responsible for it. Deviation in the β value for the proteins (1.4 $Å^{-1}$) of ±0.1 would imply deviations in the deduced direct coupling of ±20% which is still smaller than 40%. Therefore within the precision of the 3D structure of RCs[1] we can elucidate a surprisingly small superexchange enhancement of factor of ~2 of the direct rate (${}^1P^* \rightarrow P^+H_A^-$) via virtual population of the $P^+B_A^-$ radical pair.

5.9. Conclusion.

In this chapter we have derived the effective CS rate from the 1/e fluorescence lifetime of the temperature dependent time resolved fluorescence of Vinyl-B_{AB}-R26 RCs. At room temperature an energy shift of the redox potential of the Vinyl BChl relative to native BChl of 0.12 eV *in vivo* was determined. At temperatures below 200 K excited state lifetime becomes nearly temperature independent. This feature could be modeled assuming that activated CS via $P^+B_A^-$ freezes at low temperatures and direct ET from ${}^1P^*$ to $P^+H_A^-$ prevails at low temperatures. This conclusion will be proven in the Chapter 6 using a specially designed independent experimental method based on the sensitivity of electron transfer rate on electric fields. It could be shown that the nearly activationless direct rate is slightly superexchange enhanced ET process.

6. Time-resolved electric field effects on the fluorescence of Vinyl-B_{AB}-R26 RCs of *Rb. sphaeroides*

6.1 Introduction

In Chapter 5 we have developed a kinetic model describing the nature of the primary ET in Vinyl-B_{AB}-R26 RCs. As discussed there a heterogeneous thermally activated electron transfer (ET) via Vinyl-B_A to H_A is dominant at temperatures above 200 K while a nearly activationless ET proceeds below 200 K. The hypothesis that the latter process is an ET directly to the bacteriopheophytin as a primary acceptor arose there and will be rigorously examined at a temperature of 85 K with the method of Time-Resolved Electric Field Induced Fluorescence Anisotropy (TREFIFA) in this chapter. Using the TREFIFA method and the activationless nature of the ET below 200 K we will determine the width of the $P^+H_A^-$ radical pair free energy distribution independently from the determined one by the delayed fluorescence method in Chapter 4.

The identity of the primary electron acceptor in native RCs has been discussed controversially ever since the location of the "accessory" BChls as nearest neighbors to the primary donor has been revealed from x-ray structure data. The direct spectroscopic access to the potential intermediate $P^+B_A^-$ state is difficult due to a variety of phenomena and their mutual interplay, for example: (a) the superposition of main absorption bands, (b) nonspecific background absorption throughout the relevant spectral regions, (c) strong, overlapping and opposing electrochromic shifts in crucial spectral ranges, (d) significant excitonic coupling of the whole pigment system, (e) a small transient population of the possible intermediate $P^+B_A^-$, (f) processes such as intra- and inter-pigment nuclear relaxation and conformational changes of the protein dynamically affecting both spectral characteristics and ET dynamics, (g) coherent optical effects in the ultra short time domain[152] and (h) a static heterogeneity of RCs as discussed in Chapters 4 and 5. The issue of the identity of the primary acceptor has been convincingly solved by manipulating the redox potential of the primary acceptor via chemical exchange as in Vinyl-RCs, which has been discussed in the preceding chapter. At high temperatures the primary acceptor $P^+B_A^-$ has become evident from the thermal activation of primary CS after the exchange of B_A. The nature of the primary acceptor at low temperatures however is not unambiguous, since the temperature independence could either reflect activationless ET to $P^+H_A^-$ or low temperature nuclear tunneling to $P^+B_A^-$ in case a large reorganization energy and not a positive driving force is responsible for the thermal activation.

Direct spectroscopic identification of the primary acceptor will be impeded by the same list of

problems as described for native RCs. Most of these features become irrelevant, however, when using a method which directly identifies the orientation of the initially formed electric dipole moment. Since the dipole moments of $P^+B_A^-$ and $P^+H_A^-$ differ in their orientations by ~31° in RCs of *R. viridis*[162], we could unambiguously determine the primary electron acceptor on the basis of such an experiment. Such an experiment can monitor the response of $^1P^*$ decay kinetics to an external electric field, which is sensitive to the orientation of this field. By its nature such an approach is insensitive to the problems (a) - (g) and not affected by the short lifetime or the small transient concentration of a kinetic intermediate.

The structural prerequisite for applying this method rests on the determination of the relevant dipole moments from the X-ray structural data available for RCs of *R. viridis*[163] and *Rb. sphaeroides*[1, 126]. Via interaction of these dipole moments $\vec{\mu}$ with an external electric field $\vec{E}$ the free energies of the radical pair states can be manipulated according to the scalar product $\vec{\mu} \cdot \vec{E}$. Thus the free energy depends on the orientation of $\vec{\mu}$ in the electric field. As a consequence, the ET rate for these radical pairs depends on the orientation as well. Since the primary ET provides the dominant decay channel of the excited state in RCs, any change of this rate can be monitored on the excited state lifetime, e.g. via the prompt fluorescence. The orientation of the dipole moment of the initially formed radical pair can be determined from the angular dependence of the electric field effect on the primary charge separation rate with respect to the RC orientation in an external electric field.

This idea was first reported by Lockhart et al.[162] together with an experimental attempt to measure the orientation of $\vec{\mu}$. This first effort to obtain the angle between the primary dipole moment and the transition moment of fluorescence of $^1P^*$ in nonexchanged RCs consisted in measurements of the anisotropy of the fluorescence quantum yield with respect to an external electric field under the condition of isotropic excitation. This experimental approach suffered from two serious drawbacks[164, 165]: (a) In addition to the relevant prompt fluorescence with ps lifetime, slow fluorescence components could contribute to or even dominate the steady state fluorescence signal. Such additional slow components may also be sensitive to electric fields. (b) The dipole moments of both radical pairs $P^+B_A^-$ and $P^+H_A^-$ happen to project similarly onto the transition moment of fluorescence from $^1P^*$. Therefore the conclusions obtained by Lockart et al. were not unambiguous.

In this chapter the method of time-resolved electric field induced fluorescence anisotropy (TREFIFA) is presented, which overcomes the two problems described above. The time resolution allows discriminating between the electric field effect on the fluorescence in different time scales. Thus we can eliminate the contribution from delayed fluorescence or minorities of RCs with slow prompt fluorescence giving sufficient contribution to the fluorescence quantum yield.

We can also overcome the difficulty of discriminating between dipole moments accidentally projecting almost identically onto the transition moment of fluorescence by photoselection with a polarized excitation beam, which selectively excites appropriate transition moments by spectral selection [166, 173]. This method determines the angles κ (Fig. 6.2b) of the effective dipole moment relative to the chosen transition moments. The influence of a heterogeneous free energy distribution of the bacteriochlorophyll and bacteriopheophytin radical pairs is eliminated for the majority of RCs because the angle is insensitive when determined in a time-resolved manner.

6.2 How does an electric field influence electron transfer?

Depending on whether primary charge separation occurs in two steps or in one step, which may be enhanced by the superexchange mechanism, the radical pair first formed will be either $P^+B_A^-$ or $P^+H_A^-$, respectively. Due to the large distance of the radical ions, both radical pairs have large electric dipole moments amounting to $\mu_{P^+B_A^-}$ = 50 Debye and $\mu_{P^+H_A^-}$ = 82 Debye. These large dipole moments give rise to significant interaction with an externally applied electric field, as indicated in Fig. 6.1. For example, an external electric field of 1 MV/cm will cause a maximal shift of the free energy of the radical pair states $P^+B_A^-$ and $P^+H_A^-$ by 0.12 eV and 0.16 eV, respectively, after correcting for the dielectric properties of the sample[156, 167]. The free energy difference between the equilibrium configuration of the state prior to the ET process (with dipole moment $\vec{\mu}_{1P^*}$) and thereafter ($\vec{\mu}_{D^+A^-}$) is

$$\Delta G = \Delta G_0 + \left(\vec{\mu}_{1P^*} - \vec{\mu}_{D^+A^-}\right)\cdot \vec{E} \qquad (6.1)$$

with ΔG_0 being the free energy difference in absence of a field. μ_{1P*} can be estimated from the difference in dipole moments between ground and excited state $\Delta\mu$ as determined from Stark effect measurements ($\mu_{1P*} \sim \Delta\mu$ = 8 Debye)[167-169].

As a consequence of changes in ΔG both the energy and the horizontal position of the transition state on the generalized reaction coordinate Q change. The change in free energy leads to a change of the activation energy $E_a(E) = (\Delta G(E)-\lambda)^2/4\lambda k_B T$ in the Franck-Condon factor of the ET rate described by Marcus equation (see Chapter 3):

$$k = V^2 \frac{1}{\sqrt{4\pi\lambda k_B T}} e^{-\frac{E_a(E)}{k_B T}} \qquad (6.2)$$

The change in nuclear configuration of the transition state $Q_{TS}(E)$ may be reflected in a variation

of the electronic coupling matrix element $V(Q_{TS}(E))$, if Born-Oppenheimer approximation is not strict. In case ET is enhanced due to superexchange coupling, additional variations are expected:

$$V(E) = V_{13}(Q_{TS}(E)) + V(E)_{super}, \text{ where } V(E)_{super} = \frac{V_{12}V_{23}}{\Delta E_V(Q_{TS}(E))} \tag{6.3}$$

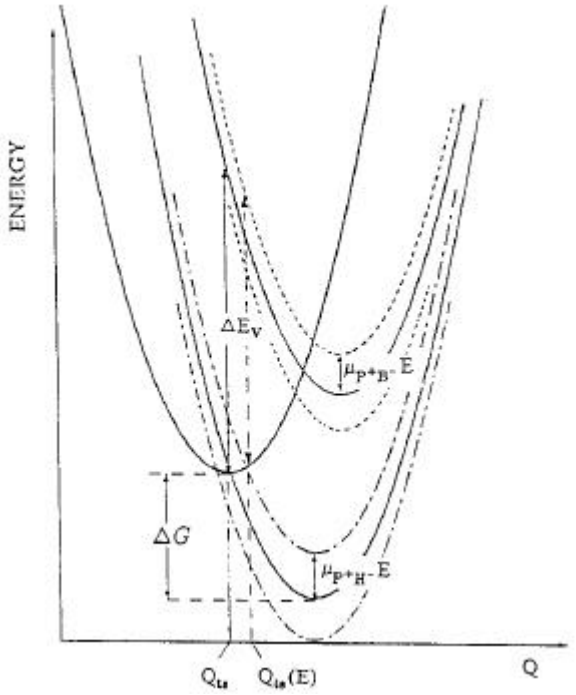

Fig. 6.1. Simplified energy diagram, of an excited neutral state ($^1P^*$) prior to charge separation and of the radical pair state formed after ET ($P^+H_A^-$) together with a virtually populated radical pair intermediate ($P^+B_A^-$) as a function of reaction coordinate (Q) and their changes due to interaction of the radical pair states with an external electric field.

with V_{12} being the coupling between the initial state ($^1P^*$) and the mediator state ($P^+B_A^-$) and V_{23} being the coupling between the mediator state and the final state ($P^+H_A^-$) and V_{13} being the direct coupling between the initial state ($^1P^*$) and the final state ($P^+H_A^-$). ΔE_V is the energy difference between $^1P^*$ and $P^+B_A^-$ radical pair states. V_{super} depends on the electric field, since the vertical energy difference between the transition state and the multidimensional potential surface of the mediating state changes due to vertical shifts of the potential surfaces and due to horizontal motion of Q_{TS}. This complicated interplay is treated elsewhere in more detail[161, 162].

According to eq. (6.1) the interaction of the electric field with the vector of the effective electric dipole moment depends on their mutual orientation. This angular dependence is the basis for a method to determine the orientation of the primary formed radical pair, as described in the next chapter. This orientation can be compared with X-ray structural data in order to identify the pathway of primary charge separation.

In a randomly oriented sample, the orientational dependence of the electric interaction gives rise to a continuous distribution of free energy differences, being reflected in a corresponding distribution of ET rates. The decay characteristics of the intrinsically heterogeneous sample have to be calculated by averaging over all possible orientations in the space. The kinetics will be nonexponential, with decay components differing from the decay components observed without field. In case the rate is activationless as reported in the previous chapter, it can not be further enhanced. Therefore a kinetic dispersion only to slower decay time constants will be expected. Two different approaches have been made to handle the difficulties arising from such complex kinetics when studying the rather slow recombination of $P^+Q_A^-$. By fast modulation of the electric field during the ET process, effort has been made to isolate the electric field effect in an experimentally elegant way[170]. Alternatively, the kinetic trace has been analyzed rigorously by numerical fitting and making use of cumulant expansion techniques[171, 172]. Such an analysis necessarily rests on an extreme reliability of experimental data with high dynamic range and very good linearity. Experiments in vectorially oriented RC preparations are very attractive[172], since they avoid this intrinsic heterogeneity but are unfortunately very difficult to realize with high time resolution techniques, since membrane preparations with sub-monolayer concentrations have to be utilized. Because of the long dead time of the RCs due to long living intermediates and because of very low fluorescence quantum yields, experiments with such low concentrations or in the single molecular regime are practically impossible.

6.3 The TREFIFA method

The orientational dependence of electric field induced change of the ET rates will be reflected in the anisotropic properties of any signal related to the speed of ET. In this context we consider the anisotropy monitored on changes of the time resolved prompt fluorescence F(t) of the primary donor $^1P^*$ which is know to be quenched almost exclusively by ET. Thus this anisotropy is due to electric field induced change in the charge separation rate, which is directly reflected by the lifetime of $^1P^*$.

We assume that there is a quadratic electric field dependence on the time resolved fluorescence as it has been proven for the fluorescence quantum yield of native R26 RCs[156] (see section 6.5.). Therefore this method is based on the same assumption as the DELFY method reported in [166, 173] relating to the signal of overall fluorescence quantum yield. The DELFY and TREFIFA methods are based on the selective excitation of appropriate transitions with polarized light, thereby achieving a defined orientational selection of RCs with respect to the electric field. In TREFIFA experiments the registration of this anisotropy pertains to the different contribution of the various

fluorescence components to different time intervals and thus leads to obtaining the time-resolved orientation of the dipole moment for the different ET processes.

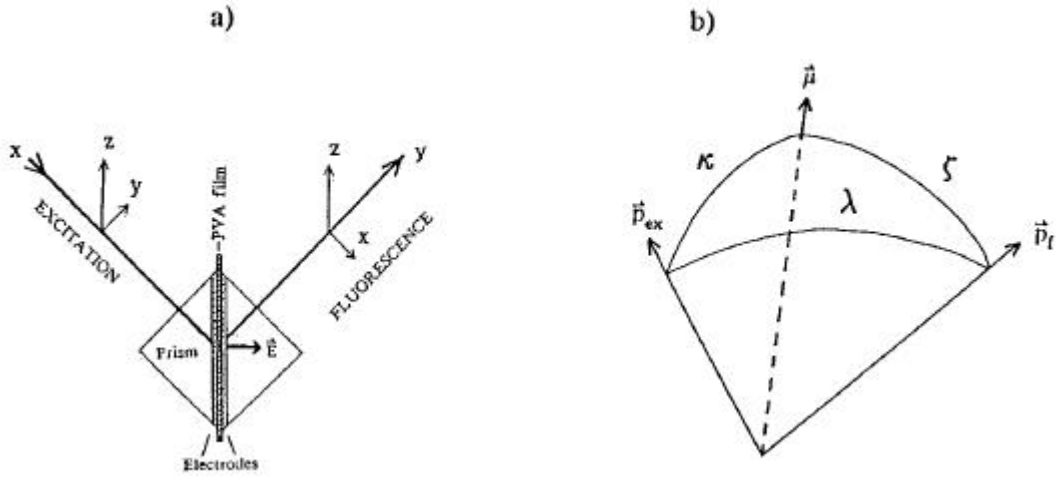

Fig. 6.2. (a) Sample configuration: sample sandwiched between two prisms, providing refractive index matching for excitation beam (in x direction) and for emitting fluorescence (in y direction). Both excitation and emission enter the prism perpendicularly and the PVA film under 45°. Excitation may be polarized in the z and y direction and the fluorescence in the z and x direction. The electric field $\vec{E}$ is applied perpendicularly to the film by two electrodes. (b) Internal configuration of dipole moment $\vec{\mu}$, transition moment of excitation $\vec{p}_{ex}$ and emission $\vec{p}_f$ spanning a tripod with the angles κ, ξ and λ.

Polarized excitation of selected transition moments photoselects RCs out of a given isotropic distribution. The assumption is made that energy transfer from any excited cofactor to P occurs exclusively within the same RC. This assumption has been justified by linear dichroism experiments determining the same orientation of the fluorescence dipole moments as expected from X-ray structure[143, 166, 173].

Additional photoselection is achieved by detecting the fluorescence at a defined angle of polarization. These photoselection conditions define an orientational distribution of RCs with corresponding projections of the radical pair dipole moment onto the electric field direction and thus with corresponding changes of the fluorescence. Since different transitions with different projection angles κ can be selected by appropriate excitation wavelengths, the knowledge of the orientation of the transition moments enables the construction of the vector of the dipole moment of the primary radical pair in the coordinate system of the RC. According to the X-ray structural data[1, 126, 163], the various pigments in the RC supply transition moments which differ significantly in κ for the two possible states $P^+B_A^-$ and $P^+H_A^-$[165, 166, 174]

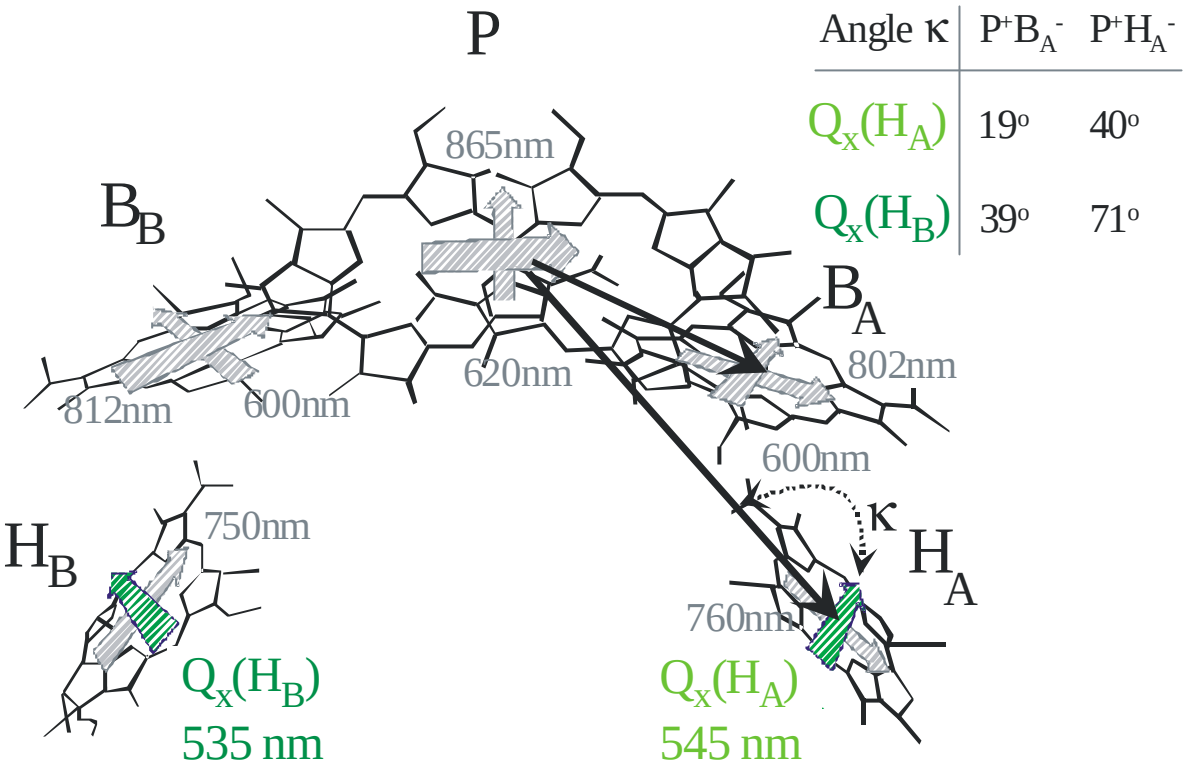

Fig. 6.3. Photoselective excitation of suitable transition moments leads to an orientation of the electric dipole moment in an external field depending on κ. The most suitable spectral regions are $Q_x(H_A)$ and $Q_x(H_B)$ (see Table 6.1).

The magnitude of the electric field effect of all RCs with respect to a given condition of photoselection has to be calculated by averaging over all their possible orientations. Such calculations are the theoretical basis of both DELFY and TREFIFA experiments and have been worked out in detail[165]. In this averaging procedure a quadratic electric field dependence of the fluorescence change $\Delta F(t) = F(t,E) - F(t,0)$ has been taken. A quadratic field dependence of $\Delta\Phi(E) = \int_0^\infty \Delta F(t,E)dt$ has been verified experimentally up to fields of ~ 10^6 V/cm[164, 166, 174]. In isotropically oriented RCs, any linear contributions have to cancel due to mirror symmetry with respect to the electric field. An analytical solution of the orientational integration is not possible. Thus calculations have to be solved numerically, in principle allowing for any field dependence to be accounted for.

From DELFY experiments ruled out any influence of electric field induced spectral shifts[166, 174-176]. The respective angular dependences of such electrochromic shifts can enhanced by the field effect on the fluorescence yield leading to complex field induced spectral features, which can be considerably larger in amplitude than the Stark effect[175, 176].

In the context of this chapter, the relevant quantity is the *anisotropy* of the electric field effect rather than its magnitude and field dependence. Therefore uncertainties with respect to the local strength of the electric field do not affect the reliability of the method. However, the assumption

has to be made that the distortion of the internal field due to the anisotropy of the dielectric properties is negligible.

Table 6.1. The angles between the transition moments given in the first column and the dipole moment of either $P^+B_A^-$ or $P^+H_A^-$ together with the correspondent anisotropy ratios $\Delta F(yx)/\Delta F(zx)$

	μ_{B_A} ($P^+B_A^-$)		μ_{H_A} ($P^+H_A^-$)	
	Angle κ	$\Delta F(yx)/\Delta F(zx)$	Angle κ	$\Delta F(yx)/\Delta F(zx)$
$Q_x(H_B)$	39° ± 3°	1.25 ± 0.10	70° ± 3°	0.75 ± 0.07
$Q_x(H_A)$	20° ± 4°	$1.65^{+0.30}_{-0.15}$	49° ± 4°	$1.0^{+0.15}_{-0.10}$
$Q_y(H_B)$	48° ± 6°	1.05 ± 0.15	40° ± 6°	$1.2^{+0.25}_{-0.20}$
$Q_y(H_A)$	88° ± 3°	$0.70^{+0.20}$	58° ± 3°	$0.9^{+0.10}_{-0.12}$
$Q_y(P)$	57° ± 7°	$0.85^{+0.15}_{-0.20}$	61° ± 6°	0.82 ± 0.10

The analysis of the electric field induced changes of the fluorescence under the condition of polarized excitation and emission has shown that the angle κ between the dipole moment of the primary radical pair and the transition moment of excitation can be deduced from the ratio $\Delta F(yx)/\Delta F(zx)$[165]. The electric field induced change of F given in the numerator refers to the geometry given in Fig. 6.2 with the polarizations of excitation in y-direction and of fluorescence in the x-direction, the one in the denominator is with polarizations of excitation in z-direction and of fluorescence in x-direction, The difference in photoselection conditions can be appreciated by noting that for $\Delta F(yx)$ the electric field vector is in the plane defined by the two directions of polarization, while for $\Delta F(zx)$ it is out of the plane. Thus, the angle between polarization of absorption and the electric field changes from 45° to 90° while the angle between polarization of emission and the field remain unchanged at 45° in both cases. Thus the anisotropy ratio $\Delta F(yx)/\Delta F(zx)$ is most sensitive to the orientation of the electric dipole moment μ with respect to the transition moment of excitation (angle κ) while in general it is only slightly sensitive to the angle (ξ) between μ and the transition moment of fluorescence. This weak sensitivity holds as long as the angle (λ) between the transition moment of excitation and emission is not too small, since then of course ξ and κ are identical and the orientation of the transition moment of emission is indirectly selected via photoselection of the transition moment of absorption. In this case $\Delta F(yx)/\Delta F(zx)$ should reveal the same dependence on ξ and κ.

Defining the anisotropy ratio $\Delta F(yx)/\Delta F(zx)$ the polarization vectors of excitation and emission remain orthogonal while the polarization of excitation is rotated with the consequence that the detectability of the fluorescence in absence of an electric field remains unchanged, i.e. $\Delta F(yx)/\Delta F(zx) = 1$ for $E = 0$. This restriction dispenses us from normalizing $\Delta F(yx)$ and $\Delta F(zx)$

and guarantees that ΔF(yx)/ΔF(zx) is only weakly dependent on λ. This is illustrated by Fig. 4., where the calculated dependence of ΔF(yx)/ΔF(zx) on κ is shown for different values of λ, setting ξ ~ 60°. Due to the small slope of ΔF(yx)/ΔF(zx) the discrimination of κ for large values of κ becomes difficult. In complete analogy to the determination of κ, the value of ξ can be obtained from the ratio ΔF(yx)/ΔF(yz) when the polarization of emission is rotated[162]. The value of ξ ~ 60° measured in native RCs at an excitation wavelength of 870 nm[162, 164] cannot discriminate between $P^+B_A^-$ and $P^+H_A^-$, since ξ is similar in both cases. Thus we prefer photoselection with respect to excitation, since it offers a large choice of transition moments of the other cofactors with more discriminative orientations.

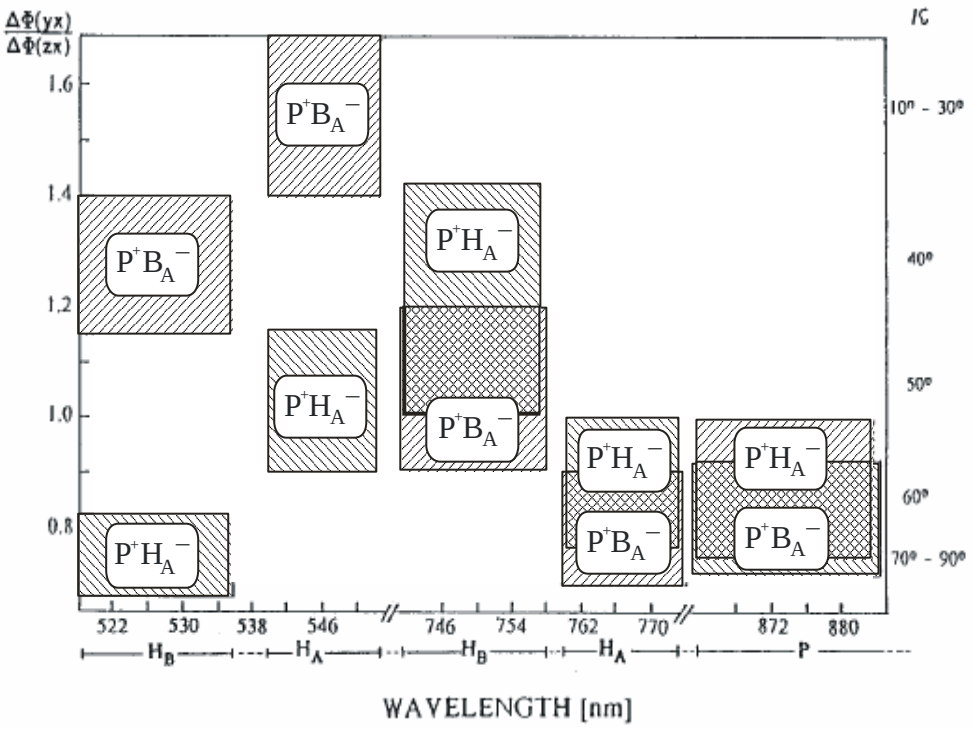

Fig. 6.4. Simulation of anisotropy values for the both radical pairs

In Table 6.1 the angles κ between the investigated transition moments and μ_B or μ_H are compiled together with the corresponding calculated values of ΔF(yx)/ΔF(zx) from Fig. 6.4. The bacteriochlorophyll transitions around 600 nm and 800 nm are omitted, because they overlap strongly and prohibit sufficient photoselection. The directions of the dipole moments are based on electron density distributions according to quantum chemical calculations[165, 177, 178] and X-ray structural data[1, 126, 163]. In the Q_x region, the directions of transition moments were assumed to be parallel to the line connecting the nitrogen atoms In ring II and IV, being consistent with linear dichroic measurements[122]. In the Q_y region, we referred to the transition moments deduced from excitonic coupling[178]. Three of the transitions exhibit values of κ differing for μ_B and μ_H almost as much as the angle of 31° between μ_B and μ_H. As an example, the angles κ

differing most for μ_B and μ_H. i.e. the one with respect to the Q_x transition of H_B at 530 nm, have been marked in Fig. 6.3. For this transition the experimental value of $\Delta F(yx)/\Delta F(zx) = 0.85\pm0.06$ has been determined earlier giving a value of $\kappa > 52°$ for nonexchanged RCs of *Rb. sphaeroides* R26 at low temperatures[166]. For the $Q_x(H_A)$ transition the angles κ are small and the small uncertainty in λ plays a larger role in this case. On the other hand the large slope of $\Delta F(yx)/\Delta F(zx)$ for small κ's in Fig. 6.3 makes the discrimination easier. For the $Q_y(H_A)$ transition the values of κ are large and consequently the discrimination is more difficult. This transition has the additional complication of partial spectral overlap with the Vinyl exchanged bacteriochlorophyll absorption band invoking some uncertainty in determination of κ.

6.4 Experimental features and results

The time-resolved electric field induced fluorescence anisotropy was measured in a single photon counting setup with 40 ps time resolution in orthogonal (right-angle) geometry (see Chapter 2 and Chapter 5). The sample was excited with ~200 fs pulses at a repetition rate of 100 kHz from a portion of a single filament white-light continuum. The excitation wavelength was determined by 10 nm bandpass filter. Rejection of the rest of the white-light continuum light was achieved with more than 3 orders of magnitude as described in Chapter 5. The excitation power was reduced with a wave-plate – polarizer couple to 800 $\mu W/cm^2$ corresponding to 0.3 - 0.5 turnovers/sec. This turnover rate was found to be sufficient to avoid trapping of the RCs in the bottleneck state $P^+Q_A^-$. Quinone containing RCs of *Rb. sphaeroides* R26 with bacteriochlorophylls (BChls) exchanged versus 3-Vinyl-13^2-OH-BChls (Vinyl-B_{AB}-R26 RCs) were imbedded in PVA yielding a film of 9±1 µm thickness with an optical density of 0.04 OD at 860 nm. The same film was investigated in Chapter 5, where a detailed description of the preparation features is presented. The film was sandwiched between two rectangular Plexiglas prisms and two mylar foils, yielding a cube (see Fig. 6.2). The mylar foils were coated with optically transparent electrodes (several tens of nanometers of ITO coating) supplying the electric field, and were oriented together with the film in the diagonal of the cube. A very small quantity of Silicon Grease with was used as a refractive index matching fluid between the film, the electrodes and the Plexiglas prisms preventing parasite reflections. Its total contribution to the interelectrode distance was estimated to be less than 1 µm. Two orthogonal faces of the cube were positioned perpendicularly to the directions of excitation and emission, thus eliminating refraction effects and orienting the electric field 45° to both directions. In order to avoid electrical breakdown, the temperature was kept constant at 85 K. This guaranteed safe operation at external fields up to 1.8 MV/cm. The light was gathered with an aspheric condenser lens and focused

through two 920 nm bandpass filters (bandwidth 10 nm) achieving an effective stray light rejection of ~10^{-7}. Single photons were detected with a microchannel plate photomultiplier (Hamamatsu R2809U with S1-cathode) which was cooled to 190 K in order to obtain a dark count rate of less than 2 cps. The fluorescence decay was measured using the time correlated single photon counting technique. The photomultiplier output was fed through an attenuator and an amplifier to a constant fraction discriminator supplying the start pulse to a time-to-amplitude converter. This was read out by an 8k analog digital converter to a 32k multichannel analyzer. The stop pulse was obtained from the trigger output of the laser supply and controlling unit. The total instrument response function had a FWHM of 40 ps. A measuring session of 8 h consisted of alternating 10 minute intervals in which either the response function was accumulated from the excitation light scattered off the sample or the 920 nm fluorescence response was accumulated. Initially the peak position of these response functions shifted with less than 11 ps. The residual shifts were taken into account before adding the fluorescence traces of the individual measuring intervals.

Time traces in the presence and absence of the external electric field, which was modulated at 100 Hz, were accumulated simultaneously. For this purpose the multichannel analyzer was modified in such a way that the incoming 8k data from the ADC were switched between four 8k segments by the electric field unit: the first segment was recording the fluorescence with electric field; the second – without field; the third – with opposite field; the fourth - again without field. The four detection segments were time-calibrated by accumulating steady state ambient light prior to the experiment. Any changes of the excitation pulse profile or residual drift of the detection electronics are expected to affect the four fluorescence decay traces in the same way. Taking the difference of the fluorescence signals with and without electric field should cancel such effects. This assumption was confirmed by the observation that the profiles of the instrumental response function with and without a field showed a maximum deviation of less than 10^{-3}. The dichroic ratio $\Delta F(yx)/\Delta F(zx)$ has the virtue of being insensitive to possible stray light and to field independent background fluorescence contributions since they cancel, when differences F(t,E) - F(t,0) are taken.

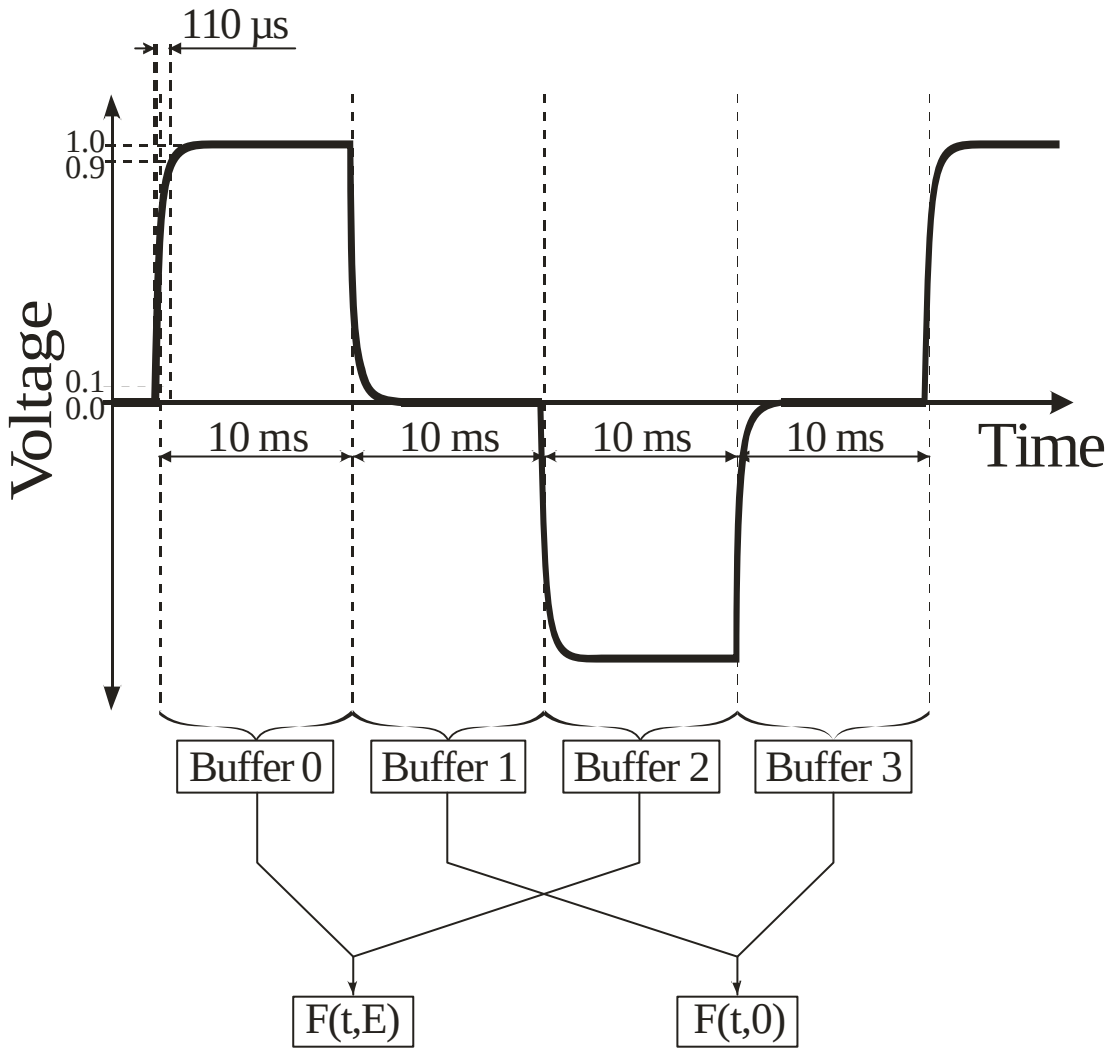

Fig. 6.5. Timing of the applied external electric field. The fluorescence is collected in 4 different 8 kBit buffers. F(t,E) from buffer 0 and buffer 2 are identical which proves the quadratic dependence of the electric field effect (see Fig. 6.7).

Time resolved fluorescence traces measured at 85 K in presence F(t,E) and absence F(t,0) of an electric field are shown in Fig. 6.6.a) and b) for yx and zx polarization. The difference $\Delta F(t,E)=F(t,E) - F(t,0)$ between both simultaneously accumulated traces is shown in Fig. 6.6c) and d) respectively. It is more pronounced at times below 0.7 ns where it is negative. Above 0.7 ns $\Delta F(t,E)$ is positive, but its absolute value is not as big as in the negative range. Integration over time thus yield a negative electric field effect on the quantum yield with a value of $\Delta\Phi/\Phi=-18\%$. The electric field effect on fluorescence slower than 2 ns, where we expect the delayed fluorescence, is very noisy, due to the small signal. Thus of uncertainty in the time resolved dichroic ratio is very large in this range, since dividing by the small difference of two large numbers $\Delta F(zx) = F_{zx}(t,E) - F_{zx}(t,0)$. In principle we expect a strong, exponential field dependence of the delayed emission [156] while prompt emission should not contribute at long times due to cutoff by internal conversion. However, the intrinsic energetic dispersion of $P^+H_A^-$

can reduce this effect significantly and may even lead to saturation, in particular at low temperature. Thus, for investigating the interesting issue of delayed emission in an electric field high temperature measurements at low fields have to be preformed. In this case longer data accumulation and simultaneous monitoring of laser fluctuations are necessary to yield sufficiently reliable results in the corresponding temporal range.

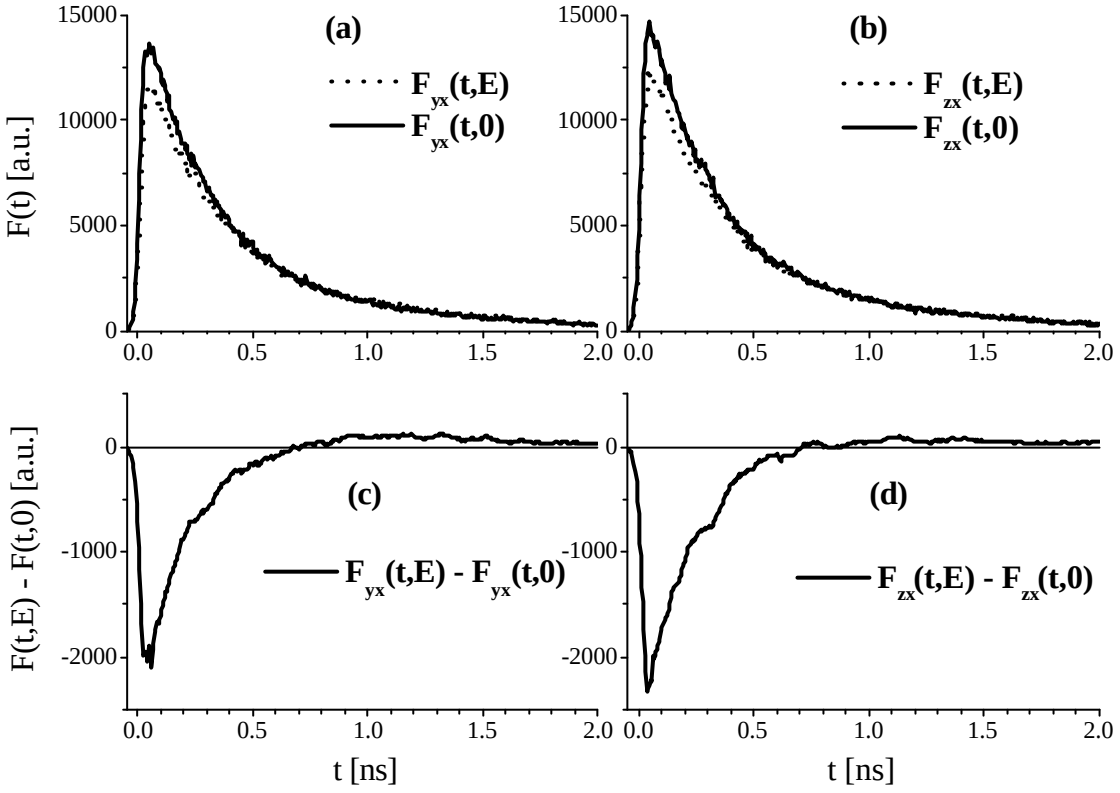

Fig. 6.6.a) Time resolved fluorescence traces F(t,0) in absence and F(t,E) in presence of an electric field of $1.4 \cdot 10^6$ V/cm detected at 920 nm after 550 nm excitation of $Vinyl_{AB}$ RCs at 85 K at yx polarization configuration. **b)** the same as a) but for zx polarization configuration. **c)** Difference F(t,E) - F(t,0) of the fluorescence traces In presence and absence of electric field as given above at yz polarization configuration. **d)** the same as (c) but for the zx polarization configuration.

The results of fitting the fluorescence decays with and without electric field at both polarization conditions with four global time constants are presented on Table 6.2. It is evident that the amplitude of the fastest component around 130 ps shows the strongest electric field effect $\Delta\Phi/\Phi$ of almost -40%. All the other components at 500ps, 1.5ns and ≈10ns exhibit effects of ≈10%, with the 1.5ns component however having positive sign. The time window of the experiment (33 ns) is not sufficient for resolving the fourth component with high reliablity.

Table 6.2. Results from the global fit with four exponents of the four fluorescence decays measured at yx and zx polarization configuration with and without applied electric field from Fig. 6.6.a) and b). At each polarization state the amplitudes are normalized to sum of the amplitudes without applied field $\Sigma A_i(0)$. Similarly the quantum yields are normalized to the sum of the quantum yields without applied electric field $\Sigma\Phi_i(0)$ for the corresponding polarization state. Consequently the amplitudes and quantum yields without field are in [%] while the amplitudes and quantum yields with field are in arbitrary units. For clarity all the values are in arbitrary units.

Polarization	i	1	2	3	4	Total
State	τ_i [ns]	0.136	0.514	1.61	10	
yx	$A_i(E)$ [a.u.]	38.8	30.8	1.47	0.0433	70.6
	$A_i(0)$ [a.u.]	64.0	34.6	1.29	0.0529	100
	$\Phi_i(E)$ [a.u.]	17.1	50.9	7.71	5.63	81.3
	$\Phi_i(0)$ [a.u.]	28.2	58.1	6.80	6.89	100
	$\Delta\Phi_i=\Phi_i(E)-\Phi_i(0)$	-39.5	-12.4	13.3	-18.2	-18.7
zx	$A_i(E)$ [a.u.]	40.6	30.6	1.49	0.0441	72.7
	$A_i(0)$ [a.u.]	63.5	35.1	1.35	0.525	100
	$\Phi_i(E)$ [a.u.]	17.7	50.9	7.8	5.7	82.1
	$\Phi_i(0)$ [a.u.]	27.7	58.4	7.06	6.78	100
	$\Delta\Phi_i=\Phi_i(E)-\Phi_i(0)$	-36.0	-12.9	10.4	-15.9	-17.9
yx/zx	$\Delta\Phi(yx)_i/\Delta\Phi(zx)_i$	1.10	0.96	1.28	1.15	1.05

A more adequate analysis of the electric field effects would have to account for the dispersion in lifetimes induced by the random orientation of the RCs in the electric field in a similar approach as demonstrated elsewhere[171, 172] (see section 6.6.). Irrespective of this difficulty, two important statements can be summarized:

a) The fluorescence is dominated by the 130 ps and 500 ps components, as discussed in Chapter 5, yielding a 1/e lifetime of 225 ps.

b) The main contribution to the electric field effect originates from the 130 ps decay time-constant.

6.5. Time-dependent orientation of the transition moment of the primary charge separation

In order to apply the TREFIFA method for determination of the time-dependence of the orientation dipole moment we have to verify our working hypothesis that the electric field effect

on fluorescence has a quadratic dependence on the applied electric field. Measurements of the electric field effect (in yx polarization configuration) have been performed at different field strengths. Again the fluorescence decays were globally fitted with four exponents. The results from the fit are presented in Table 6.3. We define the relative field effect on each component as:

Table 6.3. Four exponential fits of the fluorescence decays at different applied high voltages on the RCs imbedded in a PVA film. The relative electric field on each component is defined as in eq. (6.3)

Applied Voltage	i	1	2	3	4	total
	τ_i [ns]	0.136	0.514	1.61	40	
1.1 kV	$A_i(E)$ [a.u.]	60	24	1.1	0.011	85
	$A_i(0)$ [a.u.]	74	26	0.8	0.007	100
	$\Phi_i(E)$ [a.u.]	33	51	7.2	1.8	92
	$\Phi_i(0)$ [a.u.]	40	54	5.2	1.2	100
	ϕ_i [%]	-18	-5.6	40	53	
1.2 kV	$A_i(E)$ [a.u.]	56	23	1.0	0.004	80
	$A_i(0)$ [a.u.]	75	35	1.3	0.053	100
	$\Phi_i(E)$ [a.u.]	23	38	5.0	0.5	66
	$\Phi_i(0)$ [a.u.]	32	56	6.5	6.6	100
	ϕ_i [%]	-26	-32	-23	-93	
1.3 kV	$A_i(E)$ [a.u.]	54	23	1.1	0.0048	79
	$A_i(0)$ [a.u.]	76	24	0.6	0.0004	100
	$\Phi_i(E)$ [a.u.]	31	51	7.3	0.81	91
	$\Phi_i(0)$ [a.u.]	43	52	4.3	0.07	100
	ϕ_i [%]	-28	-2	70	1000	
1.4 kV	$A_i(E)$ [a.u.]	38.8	30.8	1.47	0.0433	70.6
	$A_i(0)$ [a.u.]	64.0	34.6	1.29	0.0529	100
	$\Phi_i(E)$ [a.u.]	17.1	50.9	7.71	5.63	81.3
	$\Phi_i(0)$ [a.u.]	28.2	58.1	6.80	6.89	100
	ϕ_i [%]	-39.5	-12.4	13.3	-18.2	-18.7

$$\phi_i(E) = \frac{\Phi_i(E) - \Phi_i(0)}{\Phi_i(E)} \qquad (3)$$

Only the relative electric field effect of the first decay component is consistent with quadratic behavior (see Fig. 6.7). Different field dependence is expected for the other components, since

the field changes the time constants, while in the global fit we assume the time constants to be field independent. This is due to the fact that the $P^+H_A^-$ free energy has an intrinsic distribution which is broadened in external electric field. The first time constant, which represents the maximum of the distribution, should not change, because the maximum does not shift, but merely becomes smaller in amplitude due to the broadening of the distribution (see Fig. 6.10). The slower time constants although are changed due to the electric field induced redistribution of the ET rate spectrum as shown in Fig. 6.10. In addition to this effect the internal conversion k_{IC} with not clear response to the external field is playing the role of a cut off rate in the 1 ns time range[148]. Even if k_{IC} is field independent the cut contribution of the prompt fluorescence would be more preferential for the fluorescence in presence of electric field since it is dominant in slower times.

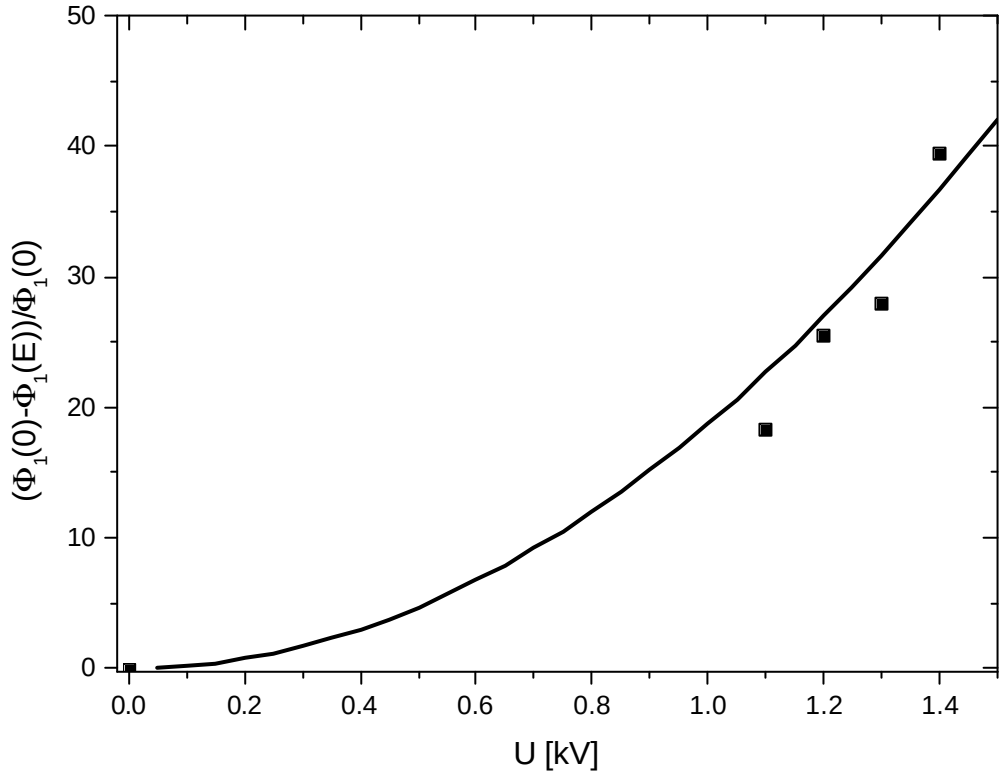

Fig. 6.7. Quadratic dependence on the applied voltage of the opposite relative electric field effect on the fluorescence quantum yield of the first decay component from the fits in Table 6.3.

It is evident from Fig. 6.7 that the field dependence is close to quadratic within the uncertainty of the experiment. The local electric field should be proportional to the external field via[179]:

$$E_{loc} = \frac{\varepsilon + 2}{3} E_{ext} \qquad (6.4)$$

where ε is the dielectric constant or permittivity of the medium. It is determining the dielectric response and is frequency dependent. Since the pulselength of the electric field is ~10 ms (see Fig. 6.5) the relevant dielectric constant is almost the static one and up to the MHz frequency range is usually not frequency dependent. In [156] it was reported that the corresponding dielectric constant for the PVA is around 3.4. Thus the local electric field was estimated to be 1.8 times higher than the external field. Thus, accounting for the determined thickness of the PVA film as 9±1 μm, at 1.4 kV external voltage the local field E_{loc} would be around 2.8±0.4 MV/cm. The corresponding dipole energy of the applied electric field could be calculated as[156]:

$$\mu E[eV] = 0.00059\mu[D]E_{loc}\left[\frac{MV}{cm}\right] \tag{6.5}$$

and is μE = 0.12 eV.

Stronger deviations could be expected from the presence of local parasitic electric fields in the protein. Recently it was shown that in Myoglobin local fields of up to 10 MV/cm could be present with unidentified origin so far. Such fields are in the same order as in our experiment (~3 MV/cm). Since there are no experimental evidences[180] we exclude for the presence large intraprotein electric fields in RCs.

In Table 6.2. the values of the electric field induced fluorescence anisotropy $\rho = \Delta\Phi(yx)/\Delta\Phi(zx)$ of the quantum yields of the different decay components are ρ = 0.96 for the 514 ps component and ρ = 1.10 - 1.15 for the 136 ps and 40 ns components. The anisotropy of the 1.61 ns component finally is ρ = 1.28. From the quadratic field dependence of the quantum yields for the different decay components we can conclude that the first, second and fourth components of the fluorescence decay definitely correspond to direct transition between $^1P^*$ and $P^+H_A^-$ using the simulation on Fig. 6.4. The electric field induced anisotropy on the quantum yield of the third fluorescence decay component is in the middle range between the values expected for primary electron transfer to $P^+H_A^-$ and to $P^+B_A^-$, respectively. Slow primary two-step CS is also not likely at 85 K because the cut off rates of the superexchange enhanced uni-step CS and internal conversion should depopulate the $^1P^*$ state up to 1 ns. This effect could be introduced by a contribution of the electric field to superexchange matrix element, shifting the vertical energy difference to high values, slowing down the rate to $P^+H_A^-$ but having part of the anisotropic signature of $P^+B_A^-$. The relative contribution of the field effect on the Franck Condon Factor and on the superexchange matrix element should be field dependent.

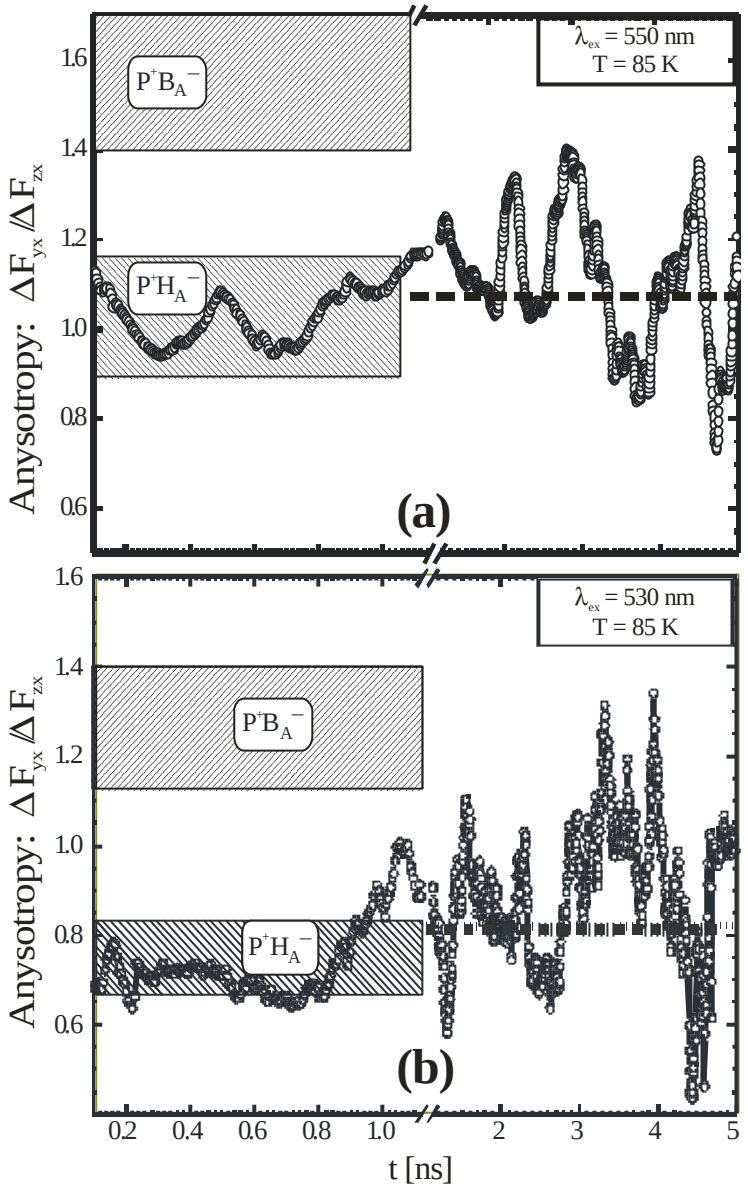

Fig. 6.8. (a) TREFIFA (circles) with averaged value taken between 0 and 2 ns of 1.08 at excitation of 550 nm at the $Q_x(H_A)$ band. (b) TREFIFA (circles) with averaged value taken between 0 and 5 ns of 0.81 at excitation of 530 nm at the $Q_x(H_B)$ band. The square bar is the theoretical calculated DELFY value (Fig. 6.4) in case of ET directly to the bacteriopheophytin.

The fit with four decay components is not aiming to present four distinct kinetic processes but rather to represent a distribution of ET rates. Therefore an inspection for the correctness of the fit would be to directly determine the electric field induced anisotropy on the time-resolved experimental data presented in Fig. 6.6. In Fig. 6.8a. it can be seen that no indication for electric field induced anisotropy of $Q_x(H_A)$ band of more than 1.20 at any time could be identified in the time window of well behavior for the anisotropy function. Similarly it can be seen that no indication for electric field induced anisotropy of $Q_x(H_B)$ band of more than 1.0 in the same time window (see Fig. 6.8b). Thus we can unambiguously define the primary CS process in

Vinyl-B_{AB}-R26 RC at 85 K as uni-step, i.e. direct from $^1P^*$ to $P^+H_A^-$. This conclusion confirms the kinetic model developed in Chapter 5 at 85 K.

6.6. Width of the $P^+H_A^-$ radical pair free energy distribution at 85 K

$P^+H_A^-$ radical pair has an intrinsic inhomogeneous distribution of free energies which is commonly taken as Gaussian (see Chapter 4). If in absence of such an intrinsic inhomogeneity $P^+H_A^-$ is initially located at G_i, the random orientation of the RCs in an external electric field would induce a Top Hat or unitary distribution of the radical pair energies with center at G_i and a width of $2\mu E$:

$$\rho_{TopHat}(G,G_i,\mu E)=\frac{\Theta(G-G_i+\mu E).\Theta(G_i+\mu E-G)}{2\mu E}=\begin{cases}1/2\mu E, & -2\mu E<G-G_i<2\mu E\\ 0, & G-G_i<2\mu E \text{ or } G-G_i<2\mu E\end{cases} \quad (6.6)$$

The intrinsic Gaussian distribution of free energies around G_0 is defined as in eq. (4.6). In this case broadening of the radical pair free energy distribution is expected to be a convolution between the both distributions:

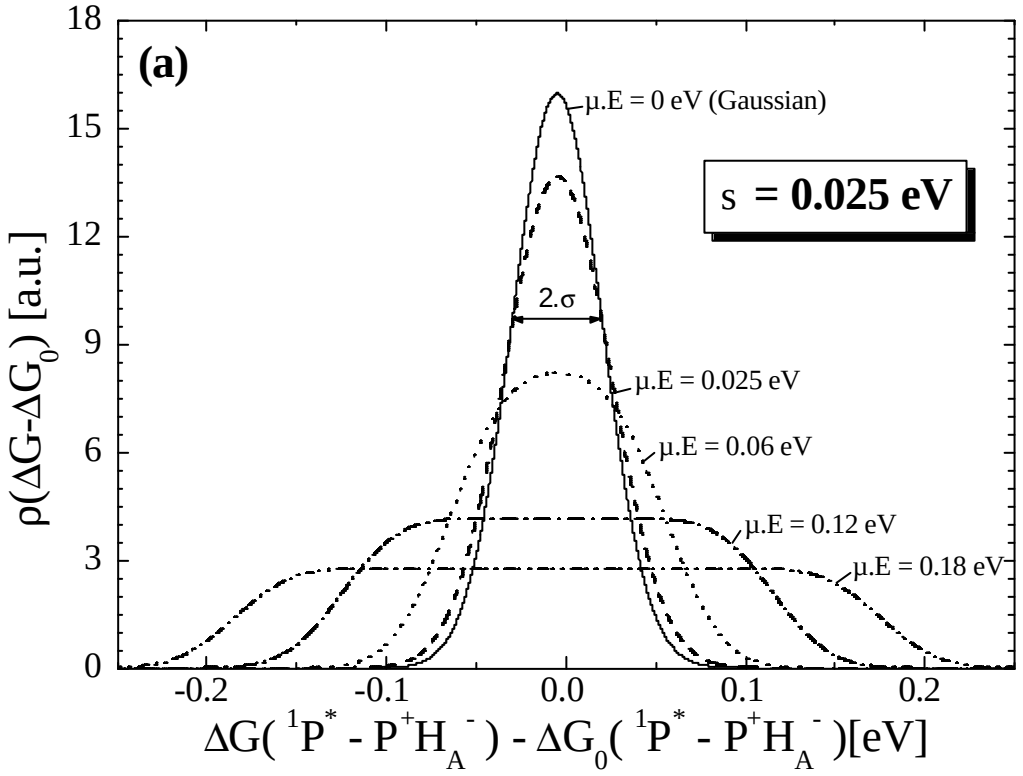

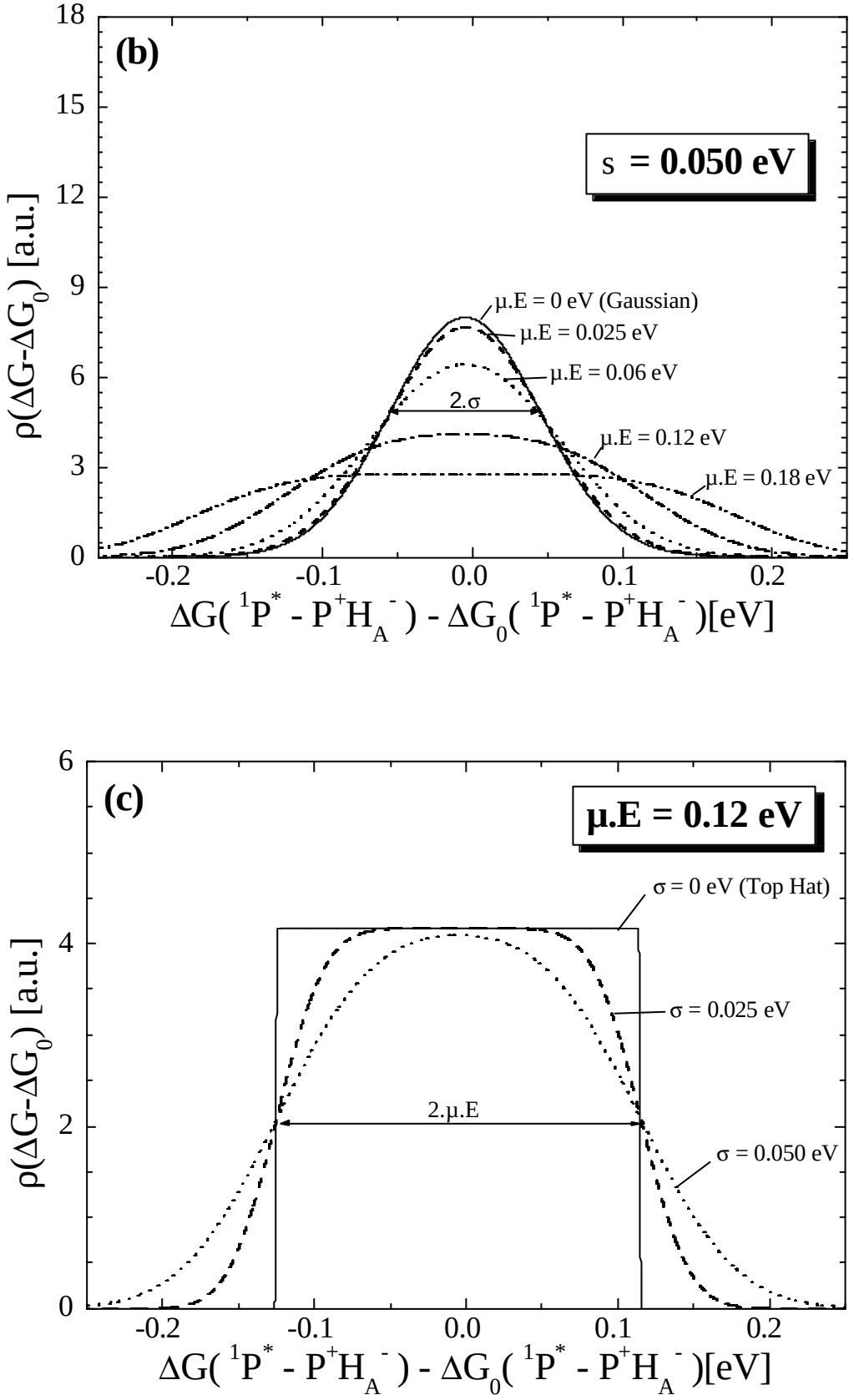

Fig. 6.9. Electric field induced $^1P^*$-$P^+H_A^-$ radical pair free energy difference distribution with σ = 0.025 eV (a) and σ = 0.050 eV (b) as determined in Chapter 4 (see Fig. 4.7) and field strengths of

μE = 0, 0.025, 0.06, 0.12 and 0.18 eV. (c) The same distribution is given for field strength μE = 0.12 eV for σ = 0, 0.025 and 0.050 eV

$$\tilde{\rho}(G,G_0,\mu E) = \rho_{Gauss} * \rho_{Top\,Hat} = \int_{-\infty}^{+\infty} \rho_{Gauss}(G_i,G_o).\rho_{Top\,Hat}(G,G-G_i,\mu E)dG_i \qquad (6.7)$$

The resultant distribution $P^+H_A^-$ radical pair free energies after applying an external electric field will be:

$$\tilde{\rho}(G,G_0,\sigma,\mu E) = \frac{1}{4\mu E}\left[erf\left(\frac{G-G_0+\mu E}{\sigma\sqrt{2}}\right) - erf\left(\frac{G-G_0-\mu E}{\sigma\sqrt{2}}\right)\right] \qquad (6.8)$$

All of the distributions are normalized to unitary area.

This distribution is shown for different field strengths and σ in Fig. 6.9. It is evident that as soon as $\mu E << \sigma$ the $\tilde{r}$ is essentially Gaussian with a width σ. At $\mu E >> \sigma$ the distribution becomes unitary having a width of $2\mu E$ and sigmoid edges (see Fig. 6.9).

For $P^+H_A^-$ the dipole moment is 82 D. For the local electric field of 2.8 MV/cm in our experiment we obtain a maximum energy shift of μE=0.12 eV. As shown in Fig 6.10 this leads to a significant broadening of the radical pair energies. As a result we expect a significant change of the distribution of ET rates. We have simulated such a distribution of ET rates and its field induced changes using simple high temperature Marcus formula (eq (3.19)) with T= 85 K and with the parameters deduced in Chapter 5: V = 1.4 eV, λ_{13} = 0.1 eV. The classical Marcus Law (eq. (3.19)) is a suitable approximation for near activationless ET even if it is induced by a nonclassical mechanism (see Fig. 3.8). The simulation is shown in Fig. 6.10. It can easily be seen that the both crossing points between the both distributions in presence and in absence of electric field will be projected exactly in the rate k_{cross} where 0 electric field effect is obtained, i.e. where the ET is independent on the electric field. Note that the both crossing points have the same deviation in energy $\Delta G_{cross} = G_{cross} - G_0$ from G_0 in the activationless case. From Fig.6.6. τ_{cross} is determined as ~700 ps Due to the linearity of the Laplace transformation we can unambiguously transform $\tau_{cross} = k_{cross}^{-1}$and thus yield for $k_{cross} \approx (700\ ps)^{-1}$. Then using the eq. (6.2) we deduce a value for the crossing point between the widened distribution from eq. (6.8) and the Gaussian distribution at energy of ΔG_{cross} = 0.053 eV. Now in order to obtain the width of the Gaussian distribution σ we have to solve:

$$f(\sigma,\Delta G_{cross},\mu E) = \frac{1}{4\mu E}\left[erf\left(\frac{\Delta G_{cross}+\mu E}{\sigma\sqrt{2}}\right) - erf\left(\frac{\Delta G_{cross}-\mu E}{\sigma\sqrt{2}}\right)\right] - \frac{1}{\sqrt{2\pi}\sigma}\exp\left(-\frac{(\Delta G_{cross})^2}{2\sigma^2}\right) = 0 \qquad (6.9)$$

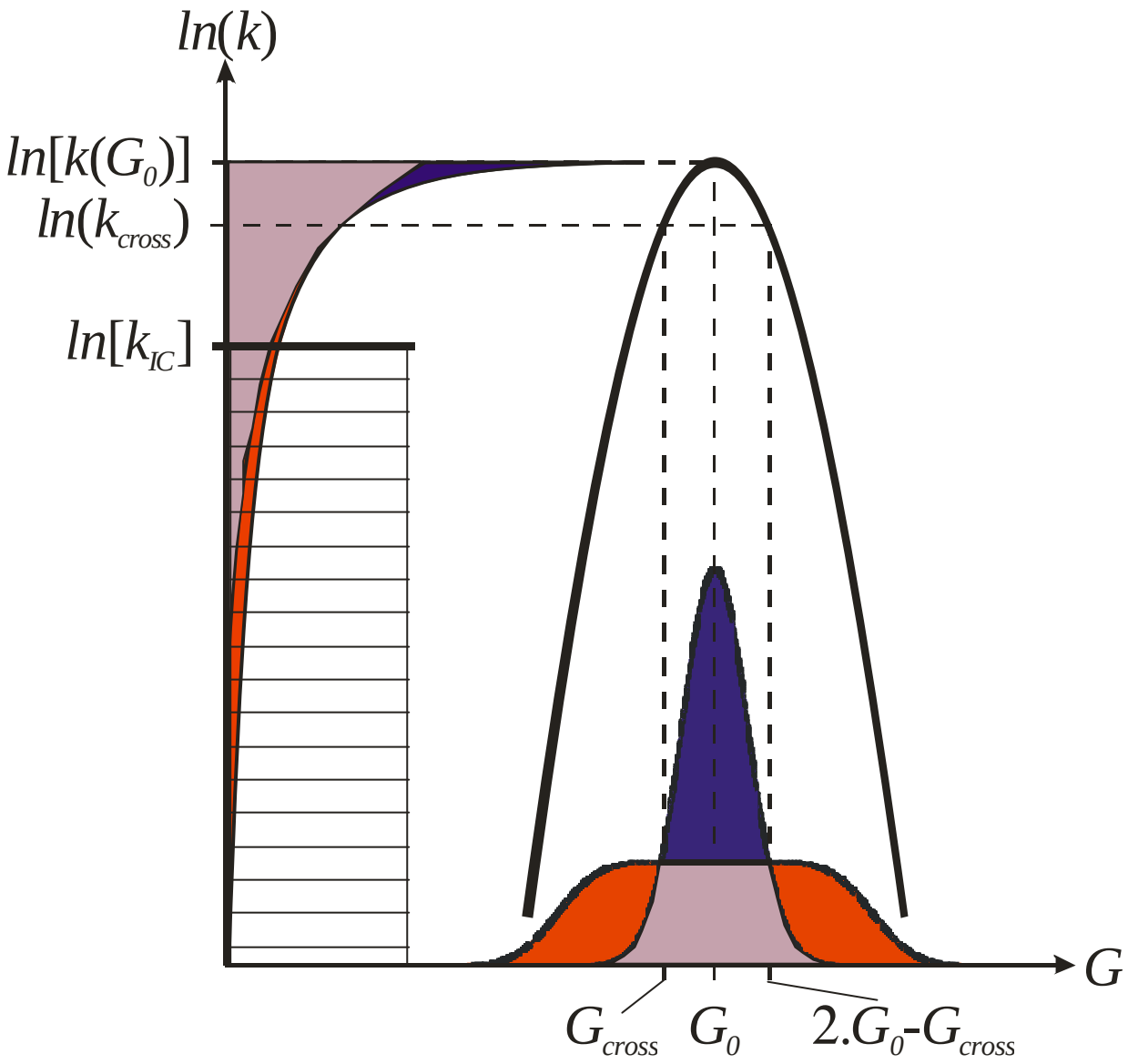

Fig. 6.10. Projection of the radical pair free energy distribution to ET rates ln(k) via Marcus parabola in the activationless case. The energy distribution in absence of external electric field is in blue and in presence of such is in red.

Unfortunately this is not an explicit equation for $\sigma(\Delta G_{cross})$ and we have to solve it numerically. The result for the width σ of the $P^+H_A^-$ radical pair free energy distribution is 0.031 eV. This value is consistent with the value of 0.025 eV determined in the case of temperature independence of σ. (see Fig. 4.7a) and with the value of 0.033 eV determined in the case of temperature dependence of σ. (see Fig. 4.7b). The value of σ determined using the TREFIFA method is very sensitive to the coupling of the direct ET from $^1P^*$ to $P^+H_A^-$ determined in Chapter 5 via temperature dependent time-resolved fluorescence measurements of the same sample. Deviations of only 0.2 cm^{-1} would imply for variation of σ in the order of ±0.010 eV.

The fact that the ET rate is activationless is very important for the validity of the method presented above. In case of deviation from the activationless case it is not trivial to connect G_{cross}

with the rate where 0 electric field effect is obtained. The two crossing points would yield different rates and k_{cross} should be in between them. There are some results pointing to a slight activation of the $^1P^* \rightarrow P^+H_A^-$ rate (see Fig. 5.7 and 5.8) which we have assigned to an effect of the inhomogeneously broadening of the $P^+B_A^-$ radical pair free energy in Chapter 5. A small deviation from activationless case of G_0 with ±0.02 eV would perturb σ significantly with ±0.015 eV calculated according to the activationless approximation. But this deviation would yield only a E_a = 0.001 eV in the eq. (6.2), (5.11) and (3.19), which is close to the precision of the fit in Fig. 5.8 justifying the activationless ET for k_3.

Nevertheless the remarkable coincidence of σ with the one measured by completely different method in Chapter 4 points out that its real value is around 0.03 eV at 85 K and the two methods are comparable.

It is evident from Fig. 6.10. why the electric field effect is more pronounced at early times and is negative. The reason for this is that the internal conversion rate plays the role of a cut off rate depopulating $^1P^*$ before the slow part of the rate distribution can be effective. This is the reason for the strong asymmetry of the positive and negative contributions to the electric field effect (see Fig. 6.6). More detailed investigation including numerical simulation of the interplay between electric field effect on the superexchange enhanced k_3 would give us a possibility also to access the electric field effect on the internal conversion rate k_{IC}. A temperature dependence of TREFIFA could in the other hand access the temperature dependence of σ.

6.7. Conclusion

In this chapter we have developed the TREFIFA method, which is an extension of the DELFY method by introducing time resolution as an additional degree of freedom. Thus for the first time the electric field induced anisotropy has been time-resolved. This method allows determining the time-dependence of the direction of the primary ET. We have applied this method to Vinyl-B_{AB}-R26 RCs in order to distinguish between $P^+B_A^-$ and $P^+H_A^-$ as a primary acceptor state. At 85 K we could verify that ET directly proceeds to the BPhe acceptor forming $P^+H_A^-$ in a single step.

If the driving force of an electron transfer reaction is not homogeneous an electric field will lead to an additional broadening of this distribution. Thus the distribution function will decrease around its center G_0 and increase in both high and low energy wings beyond a certain crossing point $G_0 \pm \Delta G_{cross}$. ΔG_{cross} is closely correlated to the width of the distribution function σ. A corresponding change of sign will also show up on the time resolved field effect of the fluorescence which reflects the distribution of electron transfer rates. Thus ΔG_{cross} can be derived

from the experimental data using the k_3 parameters derived from temperature dependent time-resolved fluorescence of the same sample in Chapter 5. It yields a value of $\sigma \approx 0.03$ eV in excellent agreement with the value derived from delayed emission from native R26 RCs in aqueous solution in Chapter 4.

7. Summary

After the **introduction** in **Chapter 1** the **experimental methods** are described in **Chapter 2** and an overview of **electron transfer theory** is given in **Chapter 3.**

In **Chapter 4 protein relaxation** triggered by charge separation has been monitored between ~50 ps to ~50 ns, a time range which so far is very poorly characterized. Based on the observation of the delayed fluorescence the protein induced change of free energy of the radical pair state $P^+H_A^-$ was traced. At low temperatures we found fast dielectric relaxation by $\Delta G \approx 0.1$ eV to occur prior to our observation window. Above the melting point of the aqueous solvent (270 K) this relaxation phase increased to $\Delta G \approx 0.2$ eV. This behavior may either result from freezing of the reorientational response of the water molecules or from restrictions of protein conformational motions imposed by the fluid-solid transition of the matrix (slaved transition). Within our observation window relaxation exhibited dispersive kinetics, which can be characterized by a Kohlrausch – Williams - Watt function. Above ~180 K the characteristic relaxation time is almost temperature independent with a very weak Arrhenius dependence. Below ~180 K the relaxation time follows a Ferry-type temperature law with an activation energy of 8.10^{-3} eV. Such a change of the temperature dependence at a characteristic transition temperature around 180 K has been observed on the relaxation time of various proteins with other methods referring to other timescales. For comparison we have tried to extrapolate relaxation data of $P^+Q_A^-$ obtained in the time range of 100 ms[28] and found that both time domains cannot be described by a single Kohlrausch – Williams - Watt function. With this in mind the unusual temperature dependence of the stretching exponent β may be attributed to an insufficient time window.

In **Chapter 5** the **mechanism of charge separation** has been scrutinized by deliberately modifying the redox potential of the supposed primary electron acceptor B_A and monitoring changes of the primary electron transfer kinetics via the spontaneous prompt fluorescence. Such modifications of redox potential have been achieved by exchanging the bacteriochlorophyll in native reaction centers against 3-vinyl-13^2-OH-BChl, the *in vivo* redox potential of which is shifted up by 0.12 eV. Earlier investigations pertaining to reaction centers of *Rb. sphaeroides* R26 in solution have been extended to reaction centers embedded in a PVA matrix and to modified RCs of *Chloroflexus Aurantiacus* in solution. In all these preparations at room temperature slows down by a factor of 10 and exhibits thermal activation with an activation

barrier of 0.6 eV, in contrast to the activationless behavior of native RCs, thus proving the direct involvement of B_A as the primary electron acceptor. At temperatures below 200 K primary charge separation becomes nearly temperature independent due to freezing of $P^+B_A^-$ formation and activationless superexchange mediated formation of $P^+H_A^-$ in a single step.

In **Chapter 6 the anisoptropy of charge separation in an external electric field** has been investigated, which allows to determine the spatial direction of the first electron transfer step. For the first time the temporal dependence of this anisotropy has been monitored confirming primary formation of $P^+H_A^-$ in Vinyl-B_{AB}-R26 RCs at 85 K. Furthermore the electric field effect allows to determine the inhomogeneous energetic broadening of the primary acceptor level $P^+H_A^-$ in a very elegant way. Due to the random orientation of the RCs with respect to the electric field, an additional broadening of the energetic distribution is imposed by the field. This leads to a decrease of the distribution around its maximum and an increase in its wings. Such changes are directly reflected in corresponding changes of the distribution of charge separation rates, which was observed as a field induced decrease of fluorescence below 700 ps and an increase at longer times. Based on the electron transfer parameters derived in Chapter 5 this translates to a energetic width of $\sigma = 0.03$ eV in excellent agreement with the results derived in Chapter 4.

8. Appendices

Appendix A

An approximated formula for the function of $\Delta G_0 = \Delta G_0[\Delta G_{app}(t),\sigma(t),T]$ was obtained via fitting of the numerical simulations (see Fig. A.1 and Fig. A.2) performed with MathCAD program as will be shown below.

If we consider the second derivative of ΔG_{app} from ΔG_0 one can see that it has a constant positive sign for all $\Delta G_0 < 0$ determining $\Delta G_{app}(\Delta G_0,\sigma,T)$ as a concave function. The first derivative is changing its sign at $\Delta G_0^{max} < 0$ which is defined as:

$$\left.\frac{d\Delta G_{app}(\Delta G_0,\sigma,T)}{d\Delta G_0}\right|_{\Delta G_0 = \Delta G_0^{max}} = 0 . \qquad \text{(A1)}$$

In this case the function $\Delta G_{app}(\Delta G_0,\sigma,T)$ is convex and this makes $\Delta G_0(\Delta G_{app},\sigma,T)$ not a single value function (see Fig. A.1). Since the concavity of the function is determined by the upper boundary of the integral which is restricted by

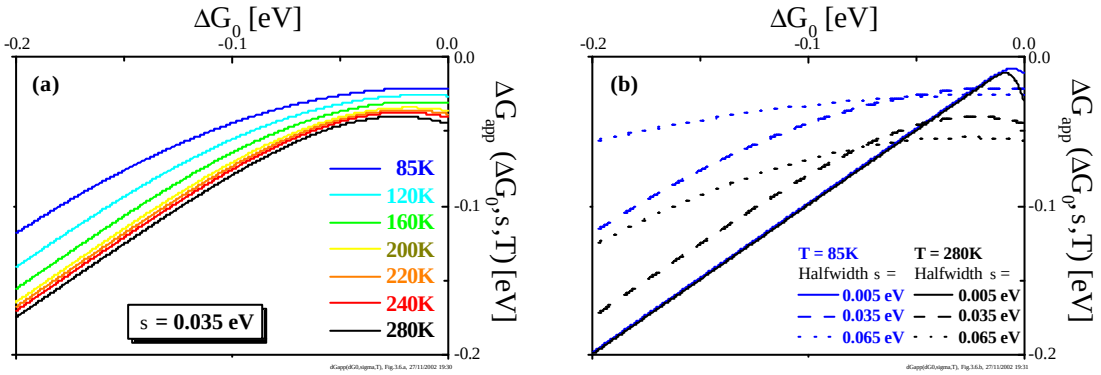

Fig. A.1. Numerical simulations of $f(\Delta G_0) = \Delta G_{app}(\Delta G_0,\sigma,T)$ for different temperatures T at half width σ of 0.035eV(a) and for different half widths σ at temperatures T of 85K and 280K(b).

the definition of the delayed fluorescence artificial by its nature, the meaningful values of $\Delta G_0(\Delta G_{app},\sigma,T)$ are for values $\Delta G_0 < \Delta G_0^{max}$ and consequently $\Delta G_0(\Delta G_{app},\sigma,T)$ is correctly defined only for $\Delta G_{app} < \Delta G_{app}\left(\Delta G_{app}^{max},\sigma,T\right) = \Delta G_{app}^{max}$. The numerical values of $\Delta G_0^{max}(\sigma,T)$ and $\Delta G_{app}^{max}(\sigma,T)$ are presented on Fig. A.2.

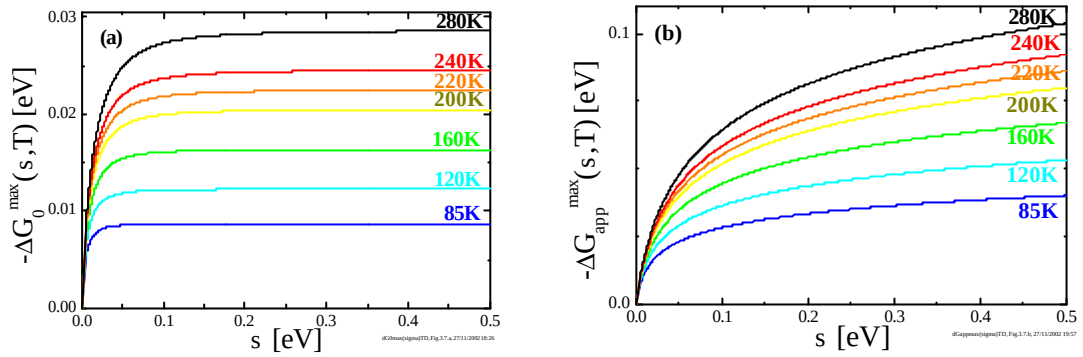

Fig. A.2. Numerical simulations of $\Delta G_0^{max}(\sigma,T)$ (a) and $\Delta G_{app}^{max}(\sigma,T)$ (b) for different temperatures.

When the width of he intermediate free energy distribution and the temperature are significantly small the upper boundary could be extrapolated to + infinity and the Boltzmann distribution could obtain the usually used approximate form[35]:

$$\rho_{Boltzmann}(\Delta G,T)=\frac{e^{\frac{\Delta G}{k_BT}}}{1+e^{\frac{\Delta G}{k_BT}}}\rightarrow e^{\frac{\Delta G}{k_BT}}=\tilde{\rho}_{Boltzmann}(\Delta G,T) \qquad \text{(A2)}$$

In this condition the function $\Delta G_{app}[\Delta G_o,\sigma,T]$ has an analytical expression of $\Delta G_0+\frac{\sigma^2}{2k_BT}$ (see Appendix B), which determines the opposite function as:

$$\Delta G_0 \xrightarrow[\sigma,k_BT\rightarrow 0]{} \Delta G_{app}-\frac{\sigma^2}{2k_BT}$$ [35].

Such a linear dependence at small σ and T should be asymptotic of an approximation formula for $\Delta G_0(\Delta G_{app},\sigma,T)$ which was obtained by the following procedure: numerical simulation of $\Delta G_{app}(\Delta G_0)$ were obtained for numerous values of σ and T (see Fig. A.1 and Fig. A.2). Indeed for $\Delta G_{app} >> \sqrt{\sigma T}$ the predicted linear asymptotic behavior was evident. Then we supposed a guess function for $\Delta G_0(\Delta G_{app},\sigma,T)$:

$$\Delta G_0=\Delta G_{app}-\frac{\sigma^2}{2k_BT}+Ampl(\sigma,T)\cdot Dec\left(\left(\Delta G_{app}-\Delta G_{app}^{max}\right),\sigma,T\right) \qquad \text{(A3)}$$

where the function Ampl(σ,T) doesn't depend on ΔG_{app} and has a meaning as an amplitude of the nonlinear function $Dec\left(\left(\Delta G_{app} - \Delta G_{app}^{max}\right),\sigma,T\right)$ which is supposed to be some type of a decaying function with an initial value of 1 converging to 0 at sufficiently big ΔG_{app} (see Fig. A.3). Then at the other boundary condition of $\Delta G_{app} = \Delta G_{app}^{max}$ we receive

$$Ampl(\sigma,T)\cdot 1 = \Delta G_0^{max} - \Delta G_{app}^{max} + \frac{\sigma^2}{2k_B T} \tag{A4}$$

Additional simulations were performed on $\Delta G_0^{max}(\sigma,T)$ and $\Delta G_{app}^{max}(\sigma,T)$ presented on Fig. A.2 and were fitted with various guess functions with dimension energy until the following global fits with $\chi^{(2)}<10^8$ were obtained:

$$\Delta G_0^{min}(\sigma,T) = -\frac{7}{6}k_B T\, erf\left(\sqrt{\frac{\sigma}{2k_B T}}\right) \tag{A5a}$$

$$\Delta G_{app}^{min}(\sigma,T) = -11k_B T\left[1-\exp\left(\sqrt{\frac{\sigma}{2k_B T}}\right)\right] - \frac{\sigma^2}{40k_B T} \tag{A5b}$$

Finally the decay function $Dec\left(\left(\Delta G_{app} - \Delta G_{app}^{max}\right),\sigma,T\right)$ was isolated and the performed numerical simulations are presented on Fig. A.3 for the same parameters as in Fig. A.1. Fits were performed with 3 different guess functions namely (exp), (1-tanh) and (1-erf) and the last one appeared to fit the simulations at best. After performing a global fitting of numerous simulations at a set of parameters {ΔG_0 = 0..1.5 eV, step of 0.00075 eV}, {σ = 0.01-0.15 eV, step of 0.005 eV} and {T = 85, 120, 160, 200, 220, 240 and 280 K} a global fit of all this simulation with $\chi^{(2)}<10^4$ was obtained for the following approximation formula:

$$\Delta G_0 = \Delta G_{app} - \frac{\sigma^2}{2k_B T} + \left(\Delta G_0^{max} - \Delta G_{app}^{max} + \frac{\sigma^2}{2k_B T}\right)\left\{1 - erf\left[\frac{\left(\Delta G_{app} - \Delta G_{app}^{max}\right)^{\frac{2}{3}}}{3\sigma^{\frac{1}{3}}\left(k_B T\right)^{\frac{1}{3}}}\right]^{\frac{2}{3}}\right\}, \tag{A6}$$

which indeed reach the asymptotic values predicted above.

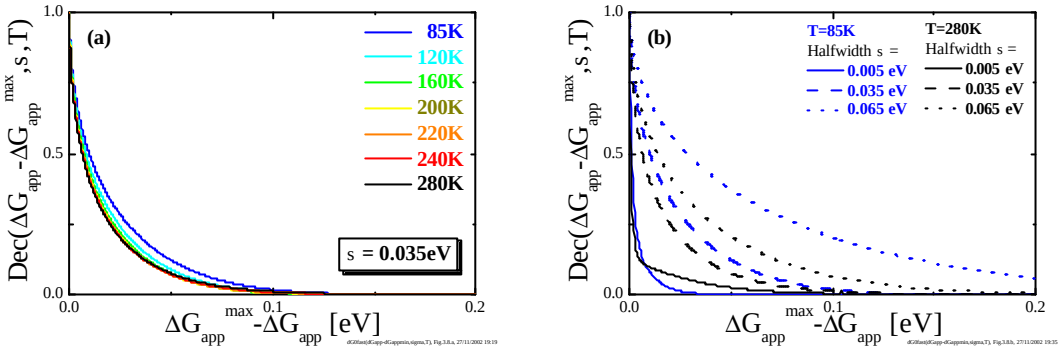

Fig. A.3. Numerical simulations of $Dec\left(\left(\Delta G_{app}-\Delta G_{app}^{max}\right),\sigma,T\right)$ for different temperatures T at half width σ of 0.035eV(a) and for different half widths σ at temperatures T of 85K and 280K(b).

Typically at ambient temperatures and less down to 85 K we have convergence to the asymptotic linear expression at ΔG_{app} ($Dec\left(\left(\Delta G_{app}-\Delta G_{app}^{max}\right),\sigma,T\right)<0.05$) not more than -0.2 eV at σ less than 0.05 eV. Thus the eq. (B5) is describing the relation between $\Delta G_0(t)$ and $\Delta G_{app}(t)$ not sufficiently well for the bacteriopheophytin radical pair in reaction centers described as discussed in the following section.

Note that such an approximate solution (eqs. (A5a-A5b)) (or its asymptotic solution[35] from eq. (B5) in the simpler case in the Appendix B) justifies a straightforward dependence between the apparent free energy and the mean value and the half width of the distribution of free energies of the radical pair state at each time t. Thus by extracting the time dependent values of the apparent free energy from experiment by the described above procedure using delayed fluorescence we can follow the relaxation of the free energy of the radical pair with time in terms of both free energy mean value and width as time dependent functions:

$$\Delta G_0(t)=\Delta G_{app}(t)-\frac{\sigma(t)^2}{2k_BT}+\left(\Delta G_0^{min}[\sigma(t)]-\Delta G_{app}^{min}[\sigma(t)]+\frac{\sigma(t)^2}{2k_BT}\right)\cdot\left\{1-erf\left[\sqrt[3]{\frac{\left\{\Delta G_{app}(t)-\Delta G_{app}^{min}[\sigma(t)]\right\}^2}{27\sigma(t)k_BT}}\right]^2\right\} \quad \text{(A7)}$$

Appendix B:

In this appendix we will present an exact solution for the relation between $\Delta G_0(t)$ and $\Delta G_{app}(t)$ at each time t approximating the exact form (eq. (4.3)) of the amplitude of the delayed fluorescence from eq. (4.1) with

$$\frac{a_{delayed}}{a_{prompt}} = \int_{-\infty}^{+\infty} \rho_{Gauss}(\Delta G_0, \sigma)\tilde{\rho}_{Boltzmann}(\Delta G, T)\, d\Delta G \qquad \text{(B1)}$$

where we are assuming Boltzmann distribution $\tilde{\rho}_{Boltzmann}(\Delta G, T) = e^{\frac{\Delta G}{k_B T}}$ (eq. (A2)) and that the distribution $\rho(\Delta G) = \rho_{Gauss}(\Delta G, \Delta G_0, \sigma) = \frac{1}{\sqrt{2\pi}\sigma} e^{-\frac{(\Delta G - \Delta G_0)^2}{2\sigma^2}}$ from eq. (4.7).

Under these conditions and using eq. (B1) we obtain for the delayed fluorescence

$$\frac{a_{delayed}}{a_{prompt}} = \frac{1}{\sqrt{2\pi}\sigma} \int_{-\infty}^{+\infty} e^{-p\Delta G^2 - q\Delta G} d\Delta G = \frac{1}{\sqrt{2\sigma^2 p}} e^{-\frac{\Delta G_0^2}{2\sigma^2}} e^{\frac{q^2}{4p}} \qquad \text{(B2)}$$

where $\begin{vmatrix} p = \frac{1}{2\sigma^2} \\ q = \frac{1}{k_B T} + \frac{\Delta G_0}{\sigma^2} \end{vmatrix}$ and finally we obtain

$$\frac{a_{delayed}}{a_{prompt}} = e^{\frac{1}{k_B T}\left(\Delta G_0 + \frac{\sigma^2}{2k_B T}\right)} \qquad \text{(B3)}$$

Consequently for the apparent energy (eq. (4.2)) extracted with the approximated Boltzmann distribution (eq. (4.4)) we have an exact expression in terms of ΔG_0 and σ.

$$\Delta G_{app}(\Delta G_0, \sigma, T) = k_B T . ln\left[\frac{a_{delayed}}{a_{prompt}}\right] = \Delta G_0 + \frac{\sigma^2}{2k_B T} \qquad \text{(B4)}$$

Now we can see that under the assumption in the beginning of the Appendix B an exact analytical solution is obtainable in the form:

$$\Delta G_0(t) = \Delta G_{app}(t) - \frac{\sigma(t)^2}{2k_B T} \qquad \text{(B5)}$$

Appendix C:

The exact solution of the system of equations from eqs. (5.5a - 5.5b) is as follows:

$$N[^1P^*](t) = \frac{\lambda_2 + k_P}{\lambda_2 - \lambda_1}.e^{\lambda_1 t} - \frac{\lambda_1 + k_P}{\lambda_2 - \lambda_1}.e^{\lambda_2 t} \quad \text{(C1a)}$$

$$N[P^+B_A^-](t) = \frac{(\lambda_1 + k_P)(\lambda_2 + k_P)}{k_{-1}(\lambda_2 - \lambda_1)}\left[e^{\lambda_1 t} - e^{\lambda_2 t}\right] \quad \text{(C1a)}$$

where $k_B = k_{-1} + k_2$, $k_P = k_1 + k_3 + k_{IC}$ and

$$\lambda_{1,2} = \frac{1}{2}\left[-(k_B + k_P) \pm (k_B - k_P).\sqrt{1 + \frac{4k_1k_{-1}}{(k_P - k_B)^2}}\right] \quad \text{(C2)}$$

are the eigenvalues of the system of equations eqs. (5.5a - 5.5b). If we introduce $k_1^* = \frac{k_1k_{-1}}{k_B - k_P}$ it is evident that

$$k_1^* = \frac{k_1k_{-1}}{k_B - k_P} \sim k_1 \langle\langle k_B \quad \text{(C3)}$$

and thus the square root in eq. (C2) is approximated via the Bernoulli formula as:

$$\left(1 + \frac{4k_1k_{-1}}{(k_P - k_B)^2}\right)^{1/2} = 1 + \frac{1}{2}.\frac{4k_1k_{-1}}{(k_P - k_B)^2} \quad \text{(C4)}$$

and thus for the population of $^1P^*$ we have:

$$N[^1P^*](t) \approx \frac{k_1^*}{k_B - k_P + 2k_1^*}.exp\left[-\left(k_B + k_1^*\right).t\right] + \left(1 - \frac{k_1^*}{k_B - k_P + 2k_1^*}\right).exp\left[-\left(k_P - k_1^*\right).t\right] \quad \text{(C5)}$$

Consequently from eq. (C3) the first amplitude is much smaller than the second and we can approximate the fluorescence decay as a monoexponential:

$$F[^1P^*](t) = k_F.N[^1P^*](t) = k_F.exp\left[-\left(k_P - k_1^*\right).t\right] \quad \text{(C6)}$$

where k_F is the oscillator strength of $^1P^*$. Consequently if we consider that

$$k_B \rangle\rangle k_P - k_1^* \tag{C7}$$

we receive the effective rate form eq. (5.6).

$$\frac{k_1^*}{k_B - k_P + 2k_1^*} : \frac{k_B - k_P + k_1^*}{k_B - k_P + 2k_1^*} < \frac{k_1^*}{k_B - k_P + k_1^*} << 1 \tag{C8}$$

9. References

[1] H. Komiya, T. O. Yeates, D. C. Rees, J. P. Allen, G. Feher, *Proc. Nat. Acad. Sci. USA* **1988**, *85*, 9012.

[2] H. Lossau, Ph.D. thesis, TU Munich, **1999**.

[3] A. Kummer, Ph.D. thesis, TU Munich, **2000**.

[4] W. Keup, Ph.D. thesis, TU Munich, **1994**.

[5] M. Friese, Ph.D. thesis, TU Munich, **1996**.

[6] T. Häberle, Ph.D. thesis, TU Munich, **1995**.

[7] P. R. Bevington, D. K. Robinson, *Data Reduction and Error Analysis for the Physical Sciences*, 2nd ed., McGraw-Hill, International, **1992**.

[8] G. J. Kavarnos, *Fundamentals of Photoinduced Electron Transfer*, Wiley-VCH, New York, **1993**.

[9] *Electron Transfer in Chemistry*, V. Balzani, Eds., Wiley-VCH, Weinheim, **2001**.

[10] F. C. De Schryver, S. De Feyter, G. Schweitzer, *Femtochemistry*, Wiley-VCH, Weinheim, **2001**.

[11] J. Jortner, M. Bixon, *Electron Transfer: From Isolated Molecules to Biomolecules*, Wiley, New York, **1999**.

[12] *Molecular Electronics*, J. Jortner, M. A. Ratner, Eds., Blackwell Science Ltd., Oxford, **1997**.

[13] R. A. Marcus, N. Sutin, *Biophys. Biochim. Acta* **1985**, *811*, 265.

[14] R. A. Marcus, *J. Chem. Phys.* **1956**, *24*, 966.

[15] R. A. Marcus, *J. Chem. Phys.* **1956**, *24*, 979.

[16] S. Pekar, *Investigations of the Electronic Theory of Crystals*, English Translation: US AEC document AEC-tr-5575, Moscow, **1951**.

[17] V. G. Levich, R. R. Dogonadze, *Dokl. Acad. Nauk. SSSR* **1959**, *124*, 123.

[18] N. S. Hush, *Electrochim. Acta* **1968**, *13*, 1005.

[19] J. Jortner, *J. Chem. Phys.* **1976**, *64*, 4860.

[20] V. May, O. Kühn, *Charge and Energy Transfer Dynamics in Molecular Systems*, Wiley-VCH, Berlin, **2000**.

[21] P. F. Barbara, T. J. Meyer, M. A. Ratner, *J. Phys. Chem.* **1996**, *100*, 13148.

[22] H. Ihee, V. A. Lobastov, U. M. Gomez, B. M. Goodson, R. Srinivasan, C.-Y. Ruan, A. H. Zewail, *Science* **2001**, *291*, 458.

[23] M. Bixon, J. Jortner, *J. Phys. Chem.* **1986**, *90*, 3795.

[24] V. De Vault, C. Chance, *Biophys. J.* **1966**, *6*, 825.

[25] A. Weller, *Z. Physik. Chem. NF* **1982**, *133*, 93.

[26] W. Schmickler, *J. Chem. Soc. - Far. Trans. II* **1976**, *72*, 307.

[27] M. H. Vos, M. R. Jones, C. N. Hunter, J. Breton, J. C. Lambry, J. L. Martin, *Biochemistry* **1994**, *33*, 6750.

[28] B. H. McMahon, J. D. Muller, C. A. Wraight, G. U. Nienhaus, *Biophys. J.* **1998**, *74*, 2567.

[29] C. C. Page, C. C. Moser, X. Chen, P. L. Dutton, *Nature* **1999**, *402*, 47.

[30] R. Langen, J. L. Colon, D. R. Casimiro, T. B. Karpishin, J. R. Winkler, H. B. Gray, *J. Biol. Inorg. Chem.* **1996**, *1*, 221.

[31] M. E. Michel-Beyerle, M. Bixon, J. Jortner, *Chem. Phys. Lett.* **1988**, *151*, 188.

[32] J. Schlichter, J. Friedrich, L. Herenyi, J. Fidy, *J. Chem. Phys.* **2000**, *112*, 3045.

[33] J. M. Peloquin, J. C. Williams, X. Lin, R. G. Alden, A. K. Taguchi, J. P. Allen, N. W. Woodbury, *Biochemistry* **1994**, *33*, 8089.

[34] A. Ogrodnik, W. Keupp, M. Volk, G. Aumeier, M. E. Michel-Beyerle, *J. Phys. Chem.* **1994**, *98*, 3432.

[35] A. Ogrodnik, G. Hartwich, H. Lossau, M. E. Michel-Beyerle, *Chem. Phys.* **1999**, *244*, 461.

[36] G. Palazzo, A. Mallardi, A. Hochkoeppler, L. Cordone, G. Venturoli, *Biophys. J.* **2002**, *82*, 558.

[37] V. V. Ponkratov, J. Friedrich, J. M. Vanderkooi, *J. Chem. Phys.* **2002**, *117*, 4594.

[38] P. J. Steinbach, A. Ansari, J. Berendzen, D. Braunstein, K. Chu, B. R. Cowen, D. Ehrenstein, H. Frauenfelder, J. B. Johnson, D. C. Lamb, S. Luck, J. R. Mourant, G. U. Nienhaus, P. Ormos, R. Philipp, A. Xie, R. D. Young, *Biochem.* **1991**, *41*, 52.

[39] J. Deisenhofer, O. Epp, K. Miki, R. Huber, H. Michel, *Journal of Molecular Biology* **1984**, *180*, 385.

[40] J. P. Allen, G. Feher, T. O. Yeates, D. C. Rees, J. Deisenhofer, H. Michel, R. Huber, *Proceedings of the National Academy of Sciences of the United States of America* **1986**, *83*, 8589.

[41] C.-H. Chang, D. Tiede, J. Tang, U. Smith, J. Norris, M. Schiffer, *FEBS Letters* **1986**, *205*, 82.

[42] O. El Kabbani, C. H. Chang, D. Tiede, J. Norris, M. Schiffer, *Biochemistry* **1991**, *30*, 5361.

[43] U. Ermler, G. Fritzsch, S. K. Buchanan, H. Michel, *Structure* **1994**, *2*, 925.

[44] T. Arlt, S. Schmidt, W. Kaiser, C. Lauterwasser, M. Meyer, H. Scheer, W. Zinth, *Proc. Nat. Acad. Sci. USA* **1993**, *90*, 11757.

[45] G. Hartwich, G. Bieser, T. Langenbacher, P. Müller, M. Richter, A. Ogrodnik, H. Scheer, M.-E. Michel-Beyerle, *Biophys. J.* **1997**, *72*, MAME7.

[46] T. Häberle, G. Bieser, T. Langenbacher, P. Müller, M. Richter, A. Ogrodnik, H. Scheer, M. E. Michel-Beyerle, in *The Reaction Center of Photosynthetic Bacteria* (Ed.: M. E. Michel-Beyerle), Springer, Berlin, **1996**, pp. 239.

[47] *Chlorophylls*, H. Scheer, Eds., CRC Press, Boca Raton Fl, **1991**.

[48] *The Photosynthetic Reaction Center*, J. R. Norris, J. Deisenhofer, Eds., Academic Press, New York, **1993**.

[49] *Anoxigenic Photosynthetic Bacteria*, R. E. Blankenship, M. T. Madigan, C. E. Bauer, Eds., Kluwer, Amsterdam, **1995**.

[50] *The Photosynthetic Reaction Center*, M. E. Michel-Beyerle, Eds., Springer, Berlin, **1996**.

[51] G. Venturoli, M. Trotta, R. Feick, B. A. Melandri, D. Zannoni, *European Journal of Biochemistry / FEBS* **1991**, *202*, 625.

[52] K. J. Kaufmann, K. M. Petty, P. L. Dutton, P. M. Renzepis, *Biochem. Biophys. Res. Comm.* **1976**, *70*, 839.

[53] D. Holten, C. Hoganson, M. W. Windsor, G. C. Schenck, W. W. Parson, A. Migus, R. L. Fork, C. V. Shank, *Biochimica et Biophysica Acta* **1980**, *592*, 461.

[54] C. Kirmaier, D. Holten, W. W. Parson, *Biochim. Biophys. Acta* **1985**, *810*, 33.

[55] C. Kirmaier, D. Holten, *Proc. Nat. Acad. Sci. USA* **1990**, *87*, 3552.

[56] M. Volk, G. Aumeier, T. Langenbacher, R. Feick, A. Ogrodnik, M.-E. Michel-Beyerle, *J. Phys. Chem. B* **1998**, *102*, 735.

[57] C. C. Schenck, R. E. Blankenship, W. W. Parson, *Biochim. Biophys. Acta* **1982**, *767*, 345.

[58] D. E. Budil, S. V. Kolaczkowski, J. R. Norris, in *Progress in Photosynthesis Research, Vol. 1* (Ed.: J. Biggens), 1 Martinus Nijhoff, Dodrecht, **1987**, pp. 25.

[59] A. Ogrodnik, M. Volk, R. Letterer, R. Feick, M. E. Michel-Beyerle, *Biochim. Biophys. Acta* **1988**, *936*, 361.

[60] C. E. D. Chidsey, C. Kirmaier, D. Holten, S. G. Boxer, *Biochim. Biophys. Acta* **1984**, *766*, 424.

[61] A. J. Hoff, *Quart. Rev. Biophys.* **1981**, *14*, 599.

[62] M. Volk, A. Ogrodnik, M.-E. Michel-Beyerle, in *Anoxygenic Photosynthetic Bacteria* (Eds.: R. E. Blankenship, M. T. Madigan, C. E. Bauer), Kluver Academic, Dortrecht, **1995**, pp. 595.

[63] S. F. Fischer, I. Nussbaum, P. O. J. Scherer, in *Antennas and Reaction Centers of Photosynthetic Bacteria* (Ed.: M. E. Michel-Beyerle), Springer, Berlin, **1985**, pp. 256.

[64] S. G. Johnson, D. Tang, R. Jankowiak, J. M. Hayes, G. J. Small, D. M. Tiede, *J. Phys. Chem.* **1989**, *93*, 5953.

[65] M. Nonella, K. Schulten, *J. Phys. Chem.* **1991**, *95*, 2059.

[66] A. Warshel, W. W. Parson, *Quart. Rev. Biophys.* **2001**, *34*, 563.

[67] H. Treutlein, K. Schulten, A. T. Brunger, M. Karplus, J. Deisenhofer, H. Michel, *Proc. Nat. Acad. Sci. USA* **1992**, *89*, 75.

[68] J. R. Norris, D. E. Budil, S. V. Kolaczkowski, J. H. Tang, M. K. Bowman, in *Antennas and Reaction Centers of Photosynthetic Bacteria* (Ed.: M. E. Michel-Beyerle), Springer, Berlin, **1985**, pp. 190.

[69] P. Hamm, K. A. Gray, D. Oesterhelt, R. Feick, H. Scheer, W. Zinth, *Biochim. Biophys. Acta* **1993**, *1142*, 99.

[70] R. J. Stanley, S. G. Boxer, *J. Phys. Chem.* **1995**, *99*, 859.

[71] G. R. Fleming, J. L. Martin, J. Breton, *Nature* **1988**, *333*, 190.

[72] T. Kakitani, H. Kakitani, *Biochimica et Biophysica Acta* **1981**, *635*, 498.

[73] Y. Jia, T. J. DiMagno, C. K. Chan, Z. Wang, M. S. Popov, M. Du, D. K. Hanson, M. Schiffer, J. R. Norris, G. R. Fleming, *J. Phys. Chem.* **1993**, *97*, 13180.

[74] W. Holzapfel, U. Finkele, W. Kaiser, D. Oesterhelt, H. Scheer, H. U. Stilz, W. Zinth, *Proc. Nat. Acad. Sci. USA* **1990**, *87*, 5168.

[75] M. H. Vos, J.-C. Lambry, S. J. Robles, D. C. Youvan, J. Breton, J.-L. Martin, *PNAS* **1992**, *89*, 613.

[76] C. Chan, T. DiMagno, L. Chen, J. Norris, G. Fleming, *Proc. Nat. Acad. Sci. USA* **1991**, *88*, 11202.

[77] N. W. Woodbury, L. Su, L. Xiaomei, J. M. Peloquin, A. K. W. Taguchi, J. C. Williams, J. P. Allen, *Chemical Physics* **1995**, *197*, 405.

[78] V. Nagarajan, W. W. Parson, D. Davis, C. C. Schenck, *Biochemistry* **1993**, *32*, 12324.

[79] H. Huber, M. Meyer, H. Scheer, W. Zinth, J. Wachtveitl, *Photosynth. Res.* **1998**, *55*, 153.

[80] S. Sporlein, W. Zinth, M. Meyer, H. Scheer, J. Wachtveitl, *Chemical Physics Letters* **2000**, *322*, 454.

[81] P. Huppman, T. Arlt, H. Penzkofer, S. Schmidt, M. Bibikova, B. Dohse, D. Oesterhelt, J. Wachtveit, W. Zinth, *Biophys. J.* **2002**, *82*, 3186.

[82] S. Schenkl, S. Sporlein, F. Muh, H. Witt, W. Lubitz, W. Zinth, J. Wachtveitl, *Biochim. Biophys. Acta* **2002**, *1554*, 36.

[83] M. Volk, G. Aumeier, T. Häberle, A. Ogrodnik, R. Feick, M. E. Michel-Beyerle, *Biophys. Biochim. Acta* **1992**, *1102*, 253.

[84] P. Tzankov, A. Ogrodnik, *unpublished results.*

[85] Z. Wang, R. M. Pearlstein, Y. Jia, G. R. Fleming, J. R. Norris, *Chem. Phys.* **1993**, *176*, 421.

[86] M. Richter, Ph.D. thesis, TU Munich, **1996**.

[87] P. Schellenberg, R. J. W. Louwe, S. Shochat, P. Gast, T. J. Aartsma, *J. Phys. Chem. B* **1997**, *101*, 6786.

[88] P. Steinbach, K. Chu, H. Frauenfelder, J. Johnson, D. Lamb, G. Nienhaus, T. Sauke, R. Young, *Biophys. J.* **1992**, *61*, 235.

[89] R. K. Clayton, B. J. Clayton, *Biochimica et Biophysica Acta* **1978**, *501*, 478.

[90] H. Frauenfelder, N. A. Alberding, A. Ansari, D. Braunstein, B. R. Cowen, M. K. Hong, I. E. T. Iben, J. B. Johnson, S. Luck, M. C. Marden, J. R. Mourant, P. Ormos, L. Reinisch, R. Scholl, A. Schulte, E. Shyamsunder, L. B. Soremen, P. J. Steinbach, A. Xie, R. D. Young, K. T. Yue, *J. Phys. Chem.* **1990**, *94*, 1024.

[91] G. J. Small, J. M. Hayes, R. J. Silbey, *J. Phys. Chem.* **1992**, *96*, 7499.

[92] F. Parak, H. Frauenfelder, *Phys. A* **1993**, *201*, 332.

[93] H. Frauenfelder, P. W. Fenimore, B. H. McMahon, *Biophys. Chem.* **2002**, *98*, 35.

[94] H. Frauenfelder, S. G. Sligar, P. G. Wolynes, *Science* **1991**, *254*, 1598.

[95] Y. A. Berlin, A. L. Burin, L. D. A. Siebbeles, M. A. Ratner, *J. Phys. Chem. A* **2001**, *105*, 5666.

[96] M. Hong, D. Braunstein, B. Cowen, H. Frauenfelder, I. Iben, J. Mourant, P. Ormos, R. Scholl, A. Schulte, P. Steinbach, *Biophys. J.* **1990**, *58*, 429.

[97] R. D. Young, H. Frauenfelder, J. B. Johnson, D. C. Lamb, G. U. Nienhaus, R. Philipp, R. Scholl, *Chemical Physics* **1991**, *158*, 315.

[98] H. Frauenfelder, P. G. Wolynes, *Phys. Today* **1994**, *47*, 58.

[99] R. Kohlrausch, *Annal. Phys. (Leipzig)* **1847**, *12*, 393.

[100] G. Williams, D. C. Watts, *Transact. Far. Soc.* **1970**, *66*, 565.

[101] Y. A. Berlin, N. I. Chekunaev, V. I. Goldanskii, *J. Chem. Phys.* **1990**, *92*, 7540.

[102] Y. A. Berlin, *Chem. Phys.* **1996**, *212*, 29.

[103] C. P. Lindsey, G. D. Patterson, *J. Chem. Phys.* **1980**, *73*, 3348.

[104] H. Scher, M. F. Shlessinger, J. T. Bendler, *Phys. Today* **1991**, *44*, 26.

[105] P. Debye, *Polar Molecules*, Dover, New York, **1945**.

[106] A. Fick, *Poggend. Annal. Phys.* **1855**.

[107] J. C. Phillips, *Rep. Prog. Phys.* **1996**, *59*, 1133.

[108] V. Balakrishnan, *Physica A* **1985**, *132*, 569.

[109] W. R. Schneider, W. Wyss, *J. Math. Phys.* **1989**, *30*, 134.

[110] I. M. Sokolov, J. Klafter, A. Blumen, *Phys. Today* **2002**, *55*, 48.

[111] J. Jäckle, *Rep. Prog. Phys.* **1986**, *49*, 171.

[112] R. Richert, *J. Chem. Phys.* **2000**, *113*, 8404.

[113] H. Bässler, *Phys. Stat. Sol. B* **1993**, *175*, 15.

[114] J. D. Ferry, L. D. Grandine Jr., E. R. Fitzgerald, *J. Appl. Phys.* **1953**, *24*, 911.

[115] H. Frauenfelder, G. U. Nienhaus, J. B. Johnson, *Ber. Bunsenges. Phys. Chem.* **1991**, *95*, 272.

[116] Y. A. Berlin, S. F. Fischer, N. I. Chekunaev, V. I. Goldanskii, *Chem. Phys.* **1995**, *200*, 369.

[117] H. Bässler, *Phys. Rev. Lett.* **1987**, *58*, 767.

[118] H. H. Leyser, W. Doster, *Eur. Biophys. J* **2000**, *29*, 321.

[119] S. Sporlein, H. Carstens, H. Satzger, C. Renner, R. Behrendt, L. Moroder, P. Tavan, W. Zinth, J. Wachtveitl, *PNAS* **2002**, *99*, 7998.

[120] P. Hamm, private communication, **2003**.

[121] J.-L. Martin, J. Breton, A. J. Hoff, A. Migus, A. Antonetti, *Proc. Nat. Acad. Sci. USA* **1986**, *83*, 957.

[122] J. Breton, J.-L. Martin, G. R. Fleming, J.-C. Lambry, *Biochem.* **1988**, *27*, 8276.

[123] J. Breton, J.-L. Martin, J. Petrich, A. Migus, A. Antonetti, *FEBS Letters* **1986**, *209*, 37.

[124] N. W. Woodbury, M. Becker, D. Middendorf, W. W. Parson, *Biochemistry* **1985**, *24*, 7516.

[125] C. Kirmaier, D. Holten, W. W. Parson, *FEBS Letters* **1985**, *185*, 76.

[126] D. Budil, P. Gast, C. Chang, M. Schiffer, J. Norris, *Annu. Rev. Phys. Chem.* **1987**, *38*, 561.

[127] J. Jortner, M. E. Michel-Beyerle, in *Antennas and Reaction Centers of Photosynthetic Bacteria* (Ed.: M. E. Michel-Beyerle), Springer, Berlin, **1985**, pp. 345.

[128] M. Bixon, J. Jortner, M. E. Michel-Beyerle, *Chem. Phys.* **1995**, *197*, 389.

[129] N. W. Woodbury, J. M. Peloquin, R. G. Alden, X. Lin, S. Lin, A. K. Taguchi, J. C. Williams, J. P. Allen, *Biochemistry* **1994**, *33*, 8101.

[130] S. Lin, A. K. W. Taguchi, N. W. Woodbury, *J. Phys. Chem.* **1996**, *100*, 17067.

[131] A. R. Holzwarth, M. G. Müller, *Biochem.* **1996**, *35*, 11820.

[132] M. H. Vos, F. Rappaport, J.-C. Lambry, D. C. Youvan, J. Breton, J.-L. Martin, *Nature* **1993**, *363*, 320.

[133] M. H. Vos, M. R. Jones, C. N. Hunter, J.-C. Lambry, J. Breton, J.-L. Martin, in *Reaction Centers of Photosynthetic Bacteria*, Springer, Berlin, **1996**, pp. 271.

[134] C. Geskes, Ph.D. thesis, Freiburg University (Freiburg i. Br.), **1995**.

[135] C. Geskes, G. Hartwich, H. Scheer, W. Mäntele, J. Heinze, *J. Amer. Chem. Soc.* **1995**, *117*, 7776.

[136] A. Struck, H. Scheer, *FEBS Letters* **1990**, *261*, 385.

[137] U. Finkele, C. Lauterwasser, A. Struck, H. Scheer, W. Zinth, *Proc. Nat. Acad. Sci. USA* **1992**, *89*, 9514.

[138] H. Scheer, A. Struck, in *The Photosynthetic Reaction Center* (Eds.: J. Deisenhofer, J. R. Norris), Academic Press, New York, **1993**, pp. 157.

[139] H. Scheer, G. Hartwich, in *Anoxigenic Photosynthetic Bacteria* (Eds.: R. E. Blankenship, M. T. Madigan, C. E. Bauer), Kluwer, Dordrecht, **1995**, pp. 649.

[140] G. Feher, M. Y. Okamura, in *The Photosynthetic Bacteria* (Eds.: R. K. Clayton, W. R. Sistrom), Plenum Press, New York, **1978**, pp. 349.

[141] A. Struck, E. Cmiel, I. Katheder, H. Scheer, *FEBS Letters* **1990**, *268*, 180.

[142] G. Hartwich, H. Scheer, V. Aust, A. Angerhofer, *Biochimica et Biophysica Acta (BBA) - Bioenergetics* **1995**, *1230*, 97.

[143] M. Meyer, H. Scheer, J. Breton, *FEBS Letters* **1996**, *393*, 131.

[144] C. Lauterwasser, U. Finkele, H. Scheer, W. Zinth, *Chemical Physics Letters* **1991**, *183*, 471.

[145] A. Struck, E. Cmiel, I. Katheder, W. Schäfer, H. Scheer, *Biochim. Biophys. Acta* **1992**, *1101*, 321.

[146] H. Frank, V. Chynwat, G. Hartwich, M. Meyer, I. Katheder, H. Scheer, *Photosynthesis Res.* **1993**, *37*, 193.

[147] G. Hartwich, M. Friese, H. Scheer, A. Ogrodnik, M. E. Michel-Beyerle, *Chem. Phys.* **1995**, *197*, 423.

[148] P. Müller, G. Bieser, G. Hartwich, T. Langenbacher, H. Lossau, A. Ogrodnik, M.-E. Michel-Beyerle, *Ber. Bunsenges. Phys. Chem.* **1996**, *100*, 1967.

[149] J. N. Demas, *Excited State Lifetime Measurements*, Academic Press, New York, **1983**.

[150] G. Hartwich, H. Lossau, A. Ogrodnik, M. E. Michel-Beyerle, in *The Reaction Centers of Photosynthetic Bacteria* (Ed.: M. E. Michel-Beyerle), Springer, Berlin, **1996**, pp. 199.

[151] G. Hartwich, H. Lossau, M.-E. Michel-Beyerle, A. Ogrodnik, *J. Phys. Chem. B* **1998**, *102*, 3815.

[152] M. H. Vos, J. C. Lambry, S. J. Robles, D. C. Youvan, J. Breton, J. L. Martin, *Proc. Nat. Acad. Sci. USA* **1991**, *88*, 8885.

[153] M. Du, S. Rosenthal, X. Xie, T. DiMagno, M. Schmidt, D. Hanson, M. Schiffer, J. Norris, G. Fleming, *Proc. Nat. Acad. Sci. USA* **1992**, *89*, 8517.

[154] G. Schweitzer, M. Hucke, K. Griebenow, M. G. Muller, A. R. Holzwarth, *Chem. Phys. Lett.* **1992**, *190*, 149.

[155] D. Braun, W. Rettig, *Chemical Physics* **1994**, *180*, 231.

[156] U. Eberl, Ph.D. thesis, TU Munich, **1992**.

[157] C. Kirmaier, D. Holten, R. Feick, R. E. Blankenship, *FEBS Letters* **1983**, *158*, 73.

[158] M. Bixon, J. Jortner, M. E. Michel-Beyerle, *Biochim. Biophys. Acta* **1991**, *1056*, 301.

[159] J. S. Connolly, A. B. Samuel, A. F. Janzen, *Photochem. Photobiol.* **1982**, *36*, 565.

[160] K. J. Laidler, *Chemical Kinetics*, Harper&Row Publ., New York, **1987**.

[161] M. Bixon, J. Jortner, M. E. Michel-Beyerle, A. Ogrodnik, *Biochim. Biophys. Acta* **1989**, *977*, 273.

[162] D. J. Lockhart, R. F. Goldstein, S. G. Boxer, *J. Chem. Phys.* **1988**, *89*, 1408.

[163] J. Deisenhofer, H. Michel, *EMBO J.* **1989**, *8*, 2149.

[164] A. Ogrodnik, M. E. Michel-Beyerle, *Z. Naturforsch.* **1989**, *44a*, 763.

[165] U. Eberl, A. Ogrodnik, M. E. Michel-Beyerle, *Z. Naturforsch.* **1990**, *45a*, 763.

[166] A. Ogrodnik, U. Eberl, R. Heckmann, M. Kappl, R. Feick, M. E. Michel-Beyerle, *J. Phys. Chem.* **1991**, *95*, 2036.

[167] D. J. Lockhart, S. G. Boxer, *Biochem.* **1987**, *26*, 664.

[168] M. Lösche, G. Feher, M. Y. Okamura, *Proc. Nat. Acad. Sci. USA* **1987**, *84*, 7537.

[169] D. J. Lockhart, S. G. Boxer, *Proc. Nat. Acad. Sci. USA* **1988**, *85*, 107.

[170] Z. D. Popovic, G. J. Kovacs, P. S. NVincett, *Chem. Phys. Lett.* **1985**, *116*, 405.

[171] S. Franzen, R. F. Goldstein, S. G. Boxer, *J. Phys. Chem.* **1990**, *94*, 5135.

[172] M. Bixon, J. Jortner, *J. Phys. Chem.* **1988**, *92*, 7148.

[173] A. Ogrodnik, *Mol. Cryst. Liq. Cryst.* **1993**, *230*, 35.

[174] A. Ogrodnik, *Biochim. Biophys. Acta* **1990**, *1020*, 65.

[175] D. J. Lockhart, C. Kirmaier, D. Holten, S. G. Boxer, *J. Phys. Chem.* **1990**, *94*, 6987.

[176] S. G. Boxer, D. J. Lockhart, S. Franzen, S. H. Hammes, in *Reaction Centers of Photosynthetic Bacteria* (Ed.: M. E. Michel-Beyerle), Springer, Berlin, **1990**, pp. 147.

[177] M. Plato, W. Lubitz, F. Lendzian, K. Möbius, *Isr. J. Chem.* **1988**, *28*, 109.

[178] P. O. J. Scherer, S. F. Fischer, in *Perspectives in Photosynthesis* (Eds.: J. Jortner, B. Pullman), Kluwer, Dordrecht, **1990**, pp. 361.

[179] C. Kittel, *Introduction to Solid State Physics*, 7th ed., John Wiley & Sons, New York, **1996**.

[180] B. Honig, M. R. Gunner, *Biophys. J.* **1996**, *70*, 2469.

Acknowledgements

I would like to warmly thank to all who have contributed to the successful completion of this work and to the accompanying projects during its time.

I give my special thanks to

My dear supervisor Dr. Alexander Ogrodnik for the opportunity to do such a decent science in his wonderful group, for his endless creativity in solving any problem, for his patient understanding through all these years and for his outstanding openness to interesting new ideas.

Prof. Dr. Maria-Elisabeth Michel-Beyerle for her impressible support, for her experienced advises, for her permanent interest in my work and for giving me the opportunity to investigate hole transfer in DNA.

Dr. Izabela Naydenova for her helpful and stimulating discussions and for her everlasting availability for any kind of help and support.

Dr. Reiner Feick for his preparation of the samples of reaction centers of *Rb. sphaeroides* and of *Chloroflexus Aurantiacus* and for his helpful collaboration in Q_A-reconstitution and PVA film preparation.

Dr. Michaela Meyer and Prof. Dr. Hugo Scheer for the supply of the high-quality Vinyl exchanged R26 reaction centers of *Rb. sphaeroides*.

Dr. A. Chugreev, Tanja Schüttrigkeit, Dr. Mirco Götz, Christian Kompa, Dr. Andreas Kummer, Dr. Harald Lossau, Dr. Gerhard Hartwich, Dr. Peter Gilch, Dr. Peter Schellenberg, Prof. Dr. Bill Davis, Dr. Christian Musewald, Till von Feilitzsch, Dr. Stefan Hess, Nikolay Ilkov, Anton Trifonov, Dr. Hristo Iglev, Dr. Borislav Naydenov and Dr. Reinhard Haselsberger for their friendly cooperation and help in the lab.

Dr. Ivan Buchvarov for his self sacrificing support and thrust, for his creativity and excitement in doing optical science, for his understanding and ever refreshing philosophical conversations and for our very successful collaboration.

Dr. Torsten Fiebig for his braveness and thrust in giving me the opportunity to realize some of my ideas in optical science in his group, for the stimulating and exciting discussions and for the very productive work together.

Dr. Gagik Gurzadyan for his helpful discussions, friendly support and successful cooperation in other projects accompanying this work.

I am obliged to the East European Center at Technical University of Munich and especially to the head of the Center Dr. Vesselinka Koch for recommending me to Dr. Alexander Ogrodnik as a Ph.D. student and for the help in the beginning of my stay in Munich.

Michaela Reischl, Gabriele Dietrich, Brigitte Allendorf and Brigitte Goldbach for the ever friendly support with the administrative and other problems.

And last but definitely not least to my wife Maria Tzankova for her eminent patience and believe in me.